THERMOMECHANICS OF AMORPHOUS POLYMERS AND ITS APPLICATIONS TO SHAPE MEMORY BEHAVIORS

by

Rui Xiao

A dissertation submitted to The Johns Hopkins University in conformity with the requirements for the degree of Doctor of Philosophy.

Baltimore, Maryland

January, 2015

Abstract

Amorphous polymers exhibit a wide range of complex temperature-dependent and time-dependent behaviors, from elastic and rubbery to viscoplastic and glassy. At high temperatures, the polymer structure has high mobility and is in the equilibrium rubbery state. The mobility decreases with temperature, and cooling drives the initially rubbery material out of equilibrium and induces the glass transition. The glass transition mechanism can be exploited to achieve the shape memory behaviors. The programmed shape of amorphous shape memory polymers can be stored by the tremendous decrease in chain mobility and recovered to an original shape in response to an environmental trigger, such as heat and solvent, which increases the chain mobility. Modeling the shape memory effect of amorphous polymers requires modeling the temperature-dependent and time-dependent behaviors of the glass transition. Simultaneously, the investigation on shape memory behaviors of amorphous polymers can also enrich the understanding the glass transition.

In this work, we started with exploiting the glass transition to model the thermally-activated shape memory behaviors. The model adopted multiple discrete relaxation processes to describe the distribution of relaxation times for stress relaxation, structural re-

laxation, and stress-activated viscous flow. Experimental methods were also developed to obtain the stress and structural relaxation spectra, and viscoplastic parameters. The model was applied to study the deformation temperature and physical aging influence on the partially constrained recovery and fixed-strain recovery responses. The model was able to capture the main features of the shape memory recovery response observed in experiments. We further extended this model to describe the influence of solvent on the thermomechanical properties and shape memory behavior of amorphous polymers. The solvent increases the chain mobility, decreases the relaxation time and the glass transition temperature. The time-dependent diffusion process was also incorporated into the model. The model showed the ability to predict quantitatively the dramatic softening of the stress response of saturated specimen and the time-dependent solvent-driven shape recovery. In the last part of this work, we developed a thermomechanical theory that couples the structural evolution and inelastic deformation to describe the nonequilibrium behavior of amorphous polymers. We showed that this theory was able to reproduce the temperature-dependent and rate-dependent stress response spanning the glass transition and the effects of physical aging and mechanical rejuvenation on the stress response and enthalpy change observed in experiments.

ABSTRACT

Primary Reader:

Thao D. Nguyen, Associate Professor,

Department of Mechanical Engineering, The Johns Hopkins University

Secondary Reader:

Michael Falk, Professor,

Department of Materials Science and Engineering, The Johns Hopkins University

Robert Leheny, Professor,

Department of Physics and Astronomy, The Johns Hopkins University

Acknowledgments

First and foremost, I would like to express my sincere gratitude to my PhD advisor Professor Vicky Nguyen, for her continuous support and guidance during my PhD period. When I joined Vicky's lab in 2009, I knew little about polymers and computational mechanics. Over these years, I learned from Vicky in her courses and at every one of our meeting. Vicky is a guru of computation mechanics. Whenever I became frustrated by the code and simulations, I turned to Vicky. She was always helpful, and I was never disappointed. I also greatly appreciate the freedom Vicky gave me to choose the research subjects that I am interested in. I am also deeply grateful to my committee members, Professor Michael Falk and Professor Robert Leheny, for their valuable suggestions and comments to my work.

I want to thank my collaborators, Professor Christopher Yakacki at University of Colorado, and Professor Carl Frick at University of Wyoming on the project of shape memory polymers, and Professor David Gracias from Department of Chemical and Biomedical Engineering at Johns Hopkins on the project of hydrogels. The discussion with them was always inspiring. In particular, I would like to thank Chris for his expert advice on polymer synthesis and characterization.

ACKNOWLEDGMENTS

I want to thank Professor Michael Yu for allowing me to use his lab to perform polymer synthesis in the first two years of my PhD, Professor Howard Katz for allowing me to use the DSC equipment and Professor Hemker for providing access to the micro-tensile tester.

I would like to thank my labmates: Baptiste Coudrillier, Theresa Koys Tonge, Barbara Murienne, Xiang Chen, Kimberly Ziegler, Kristin Myers, Jin Choi, Stephen Alexander, Rajneesh Bhardwaj, Jingkai Guo, Dan Midgett, Sarah Bentil, Aurlie Azoug and Michelle Chen. It is joyful to work with all of the members of Vicky's group. I appreciate the help from them, both regarding work and in my personal life. I would also acknowledge the undergraduates who worked with me, Jonathan Wang and Brandon Lee. I want to extend my gratitude to the whole Mechanics and Materials community at Hopkins. They were always friendly and willing to help. In particular, I would like to thank Matt Shaeffer, Yong Zhang and Guangli Hu for the help and suggestions on experiments.

I am grateful for my funding support. I thank Mechanical Engineering for the Department Fellowship during the first year. My work was then funded by the PECASE award,, administered by Sandia National Labs. Sandia is a multiprogram laboratory operated by Sandia Corporation, a Lockheed Martin Company, for the United States Department of Energy under contract DE-ACO4- 94AL85000.

Finally I would express my deepest gratitude to my family in China, my parents and my sister. They have given me unconditional love, constant encouragement and support through all these years. Without this, I would never have been able to go so far on my own.

Dedication

This thesis is dedicated to my family.

Contents

CONTENTS

List of Tables

List of Figures

Chapter 1

Introduction

Shape memory polymers (SMPs) are smart materials that can memorize one or multiple temporary shapes and recover to their permanent shape in response to an environmental stimulus, such as heat,[1–5] light,[6–9] electricity,[10–12] pH[13] or solvent.[14–17] Among various types of SMPs, thermally-activated SMPs are the most widely investigated due to their ease of synthesis and characterization,[18,19] tunable mechanical properties,[4] and broad potential applications.[20–23] Several different thermally-activated mechanisms[3,20,24,25] can be employed to achieve the shape memory effect (SME), but the most common mechanism is glass transition of amorphous polymers. Amorphous SMPs are typically programmed at the temperature above the glass transition temperature (T_g), and cooled down below transition temperature to fix a temporary shape. The programmed SMPs are then heated above the T_g to achieve shape recovery. The tremendous change in thermomechanical properties during the glass transition is the underlying physical mechanism behind the shape memory

effect.

Compared with the emerging field of SMPs, the glass transition behaviors of amorphous polymers have been extensively studied for more than half a century. The characterization techniques for the glass transition can be applied to investigate amorphous SMPs, and the theories can be employed to model the shape memory behaviors. Thus, exploiting our knowledge of the glass transition can improve our understanding of the complex thermo-mechanical properties and shape recovery responses of SMPs under various conditions. Simultaneously, the research on amorphous SMPs can also enrich our understanding of glass transition behaviors.

This chapter begins by introducing the phenomena and theories of the glass transition. The following section reviews recent work on characterization and modeling the thermally-activated shape memory effect. From this, it demonstrates how the glass transition theories can be employed to model the thermally-activated shape memory behaviors. Sec. 1.1.3 introduces shape memory recovery of amorphous polymers in solvent from both experimental and modeling perspectives. This section shows that the solvent-induced SME arises from the depression of the T_g through the plasticization effect. Sec. 1.1.4 describes the physical aging and mechanical rejuvenation behaviors of the amorphous polymers in their glassy state. Finally, the outline of this thesis is listed.

1.1 Glass Transition of Amorphous Polymers

1.1.1 Description of the Phenomena

The glass transition describe the reversible change of amorphous materials from a hard glassy state to a soft rubbery or molten state. A variety of properties show tremendous change during the glass transition. Among them, the most commonly measured properties to describe the glass transition are the modulus, enthalpy and volume.

The dependence of modulus on temperature of amorphous polymers can be measured by commercially available rheometers and dynamic mechanical analyzers.[26] Fig. 1.1 shows the storage modulus of an acrylate-based amorphous network as a function of temperature measured under a dynamic load with a constant frequency of 1Hz. As shown, at low temperatures, the polymer structure is frozen and exhibits a high glassy modulus. When the material is heated across the transition region, the polymer structure obtains more and more mobility resulting in a dramatical decrease in modulus. The polymer then reaches the rubbery plateau. The Tan(δ), or loss tangent, shown in Fig. 1.1 describes the viscoelastic dissipation characteristic of the polymers. To distinguish it from T_{g}, defined as the onset of the glass transition region, the peak of the Tan(δ) is defined as $T_{\mathrm{g}}^{\mathrm{mid}}$ in this thesis. The measured glass transition region is dependent on the applied frequency, which corresponds to the time-temperature superposition,[27] and will be discussed in Sec. 1.1.3.

Differential scanning calorimetry (DSC) techniques are widely employed to measure the enthalpy change of amorphous polymers with temperature.[28] Fig. 1.2 plots the DSC

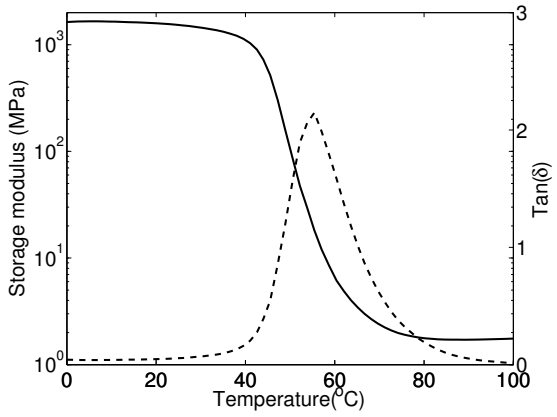

Figure 1.1: Storage modulus of acrylate-based polymer

scans of annealed and quenched polystyrene specimens upon heating. The specimens were first heated to 15°C above T_g for one hour to erase the thermal history. The quenched specimen was quickly transferred to ice water, while the annealed specimen was slowly cooled to room temperature over a period of 6-8 hours. For the quenched specimen, heat flow increased upon heating due to gradually increasing of the specific heat capacity from the glassy heat capacity c_g to the rubbery heat capacity c_r. In comparison, the annealed specimen shows an endothermic overshoot. This is caused by enthalpy loss from structural relaxation (physical aging) during the annealing period. Structural relaxation plays an important role in the performance of amorphous polymers, which is elaborated in Sec. 1.4. Briefly, the structure of amorphous polymers is unable to rearrange towards an equilibrium state instantaneously to a temperature change near T_g. Thus a longer annealing time results in a more sluggish structure (closer to the equilibrium state), which is represented by an increase in density and viscosity, and a decrease in enthalpy and mobility.

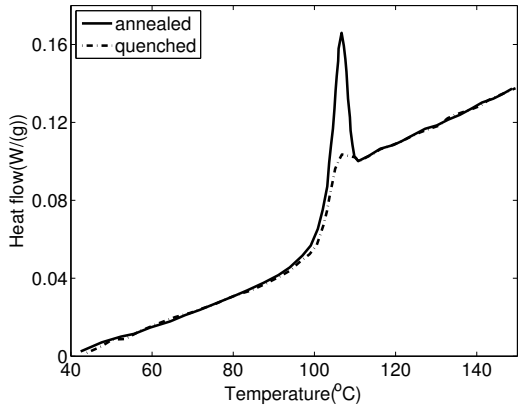

Figure 1.2: DSC scans of an annealed and quenched polystyrene using a heat rate of 10^{o}C/min. (Data extracted from Hasan and Boyce[29])

Measuring the thermal expansion using a dilatometer and thermomechanical analyzer is another general method to characterize the glass transition.[30] The volume as a function of temperature is often recorded during a constant cooling test. The coefficient of thermal expansion (CTE) shows a rapid change from a high rubbery CTE α_r to a low glassy CTE α_g around T_{g}. There are also other experiments which measure the volume change after a sudden temperature drop. Fig. 1.3 shows the volume change of poly(vinyl acetate) specimens, which were fast quenched from an initial high temperature to the measuring temperature and measured after 0.02h and 100h annealing at the measured temperature. As shown, a longer annealing period results in denser material due to the structural relaxation. All of the above experimental observations show that the glass transition process is a kinetic process and that the experimental temperature rate has an important influence on the determination of the glass transition region and thermomechanical properties.

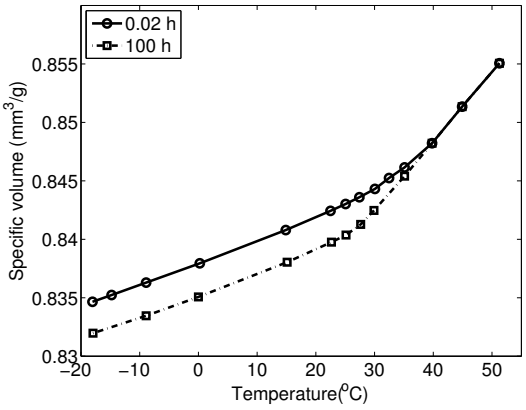

Figure 1.3: Specific volume versus temperature for poly(vinyl acetate) measured at 0.2 and 100 h after cooling rapidly from well above T_{g} (Data extracted from Kovacs[31])

1.1.2 Glass Transition Theories

Many theories[32–38] have been developed to describe the glass transition of amorphous materials. Among them, free volume theory[32,33] and configurational entropy theory[34,39] are the most widely accepted.

The free volume V_f is defined as the space not occupied by the polymer molecules, which allows the polymer segments to undergo rotation and translation. As the polymer is cooled down from their rubbery state, the free volume continuously decreases and eventually reaches a critical value where segmental motion is forbidden due to insufficient free space, resulting in a transition from the rubbery state to the glassy state. As an example, the following illustrates the dependence of the viscosity on temperature through the free volume concept. Assuming the free volume remains constant below T_{g} as V_g due to the polymer structure being frozen, the free volume at temperature T above T_{g} can be repre-

sented as,

$$V_f = V_g + \alpha_f \left(T - T_{\mathrm{g}}\right), \tag{1.1}$$

where α_f is the linear coefficient of free volume with temperature.

The following empirical equation was proposed by Doolittle[40] to express the relation between viscosity and free volume,

$$\eta(T) = A \exp\left(\frac{B}{V_f(T)}\right). \tag{1.2}$$

Substituting eq. (1.1) into (1.2) gives,

$$\eta(T) = A \exp\left(\frac{B}{V_g + \alpha_f \left(T - T_{\mathrm{g}}\right)}\right). \tag{1.3}$$

Combining eq. (1.3) with $\eta_{\mathrm{g}} = A \exp\left(B/V_g\right)$ leads to,

$$\eta(T) = \eta_{\mathrm{g}} \exp\left(-\frac{B/V_f(T - T_{\mathrm{g}})}{V_f/\alpha_f + (T - T_{\mathrm{g}})}\right). \tag{1.4}$$

By defining $C_1^{\mathrm{g}} = B/(V_f \ln(10))$ and $C_2^{\mathrm{g}} = V_f/\alpha_f$, Eq. (1.4) can be reorganized as,

$$\log\left(\frac{\eta(T)}{\eta_{\mathrm{g}}}\right) = -\frac{C_1^{\mathrm{g}}(T - T_{\mathrm{g}})}{C_2^{\mathrm{g}} + (T - T_{\mathrm{g}})}. \tag{1.5}$$

This relation is known as the Williams-Landel-Ferry (WLF) equation,[41] and is widely adopted in polymer science.

Another widely accepted approach to model the glass transition uses the configurational entropy concept. The pioneering work of configurational entropy by Gibbs and DiMarzio[34] proposed that the glass transition is in fact an experimental manifestation of the equilibrium second order phase transition. Many experiments including the examples shown in sec.

1.1.1 imply that measured T_g decreases if the cooling rate is decreased. A new transition temperature T_2 at which the configurational entropy vanishes, can be considered as the limiting value of T_g, where the experiments take an infinitely long time. In reality, due to the tremendous decrease in chain mobility when approaching T_2, the equilibrium state can never be approached, resulting in a measured T_g which is larger than T_2. The theory is derived based on a quasi-lattice theory and the main calculation involves calculating the number of configurations that chains can occupy the lattice. The detailed information of this theory will not be discussed in this thesis.

The WLF relationship can also be obtained through the configuration entropy concept. Adam and Gibbs[39] extended the Gibbs-DiMarzio theory and derived an explicit function of the relaxation time with configurational entropy S_c,

$$\tau(T) = A' \exp\left(\frac{B'}{TS_c(T)}\right). \tag{1.6}$$

The configurational entropy can be further calculated as,

$$S_c(T) = \int_{T_2}^{T} \frac{\Delta c}{T} dT. \tag{1.7}$$

The temperature dependent configurational heat capacity can be approximated as the hyperbolic form $\Delta c = a/T$ (Hodge[42]). Substituting this specific form and Eq. (1.7) into Eq. (1.6) gives,

$$\tau(T) = A' \exp\left(\frac{B'T_2/a}{T - T_2}\right). \tag{1.8}$$

The above equation can be rewritten with $\tau_{\text{ref}} = A' \exp\left(\frac{B'T_2/a}{T_{\text{ref}} - T_2}\right)$ as,

$$\tau(T) = \tau_{\text{ref}} \exp\left(-\frac{B'T_2/(a(T - T_{\text{ref}}))(T - T_{\text{ref}})}{T - T_2}\right). \tag{1.9}$$

By defining $C_1 = B'T_2/(a \ln 10(T - T_{\text{ref}}))$ and $C_2^{\text{ref}} = T_{\text{ref}} - T_2$, the same WLF relation is obtained from the configurational entropy theory,

$$\log a(T) = \log\left(\frac{\tau(T)}{\tau_{\text{ref}}}\right) = -\frac{C_1^{\text{ref}}(T - T_{\text{ref}})}{C_2^{\text{ref}} + (T - T_{\text{ref}})}. \tag{1.10}$$

Although both theories explain the glass transition phenomena with considerable success, there are still limitations. For example, the free volume theory fails to predict the influence of chain length or side chain on the glass transition. The configurational entropy concept fails to explain the glass transition of inorganic networks. The emerging of the new experimental and simulation techniques may be able to improve the understanding and help develop a universal description of the glass transition.

1.1.3 Time Temperature Superposition

The time temperature superposition (TTS) principle states that the shape of the time (frequency) response function does not change with temperature, so that a measurement at a certain temperature is equivalent to a measurement at a higher temperature and shorter time. This implies the mechanical response at various temperatures can be predicted from the master curve at the reference temperature, and vice versa. The TTS principle can be explained as following: for a thermorheologically simple materials, such as a generalized Maxwell viscoelastic solid,[43] the stress relaxation modulus can be represented as,

$$E(t, T) = E^{\text{eq}} + \sum E_i^{neq} \exp\left(-\frac{t}{\tau(T)}\right), \tag{1.11}$$

Previously, it is shown that the relaxation time at different temperatures are related with each other through a shift factor a_T.[27] Thus the relationship between the stress relaxation modulus measured at two temperatures, T_0 and T is,

$$E(t, T) = E\left(a_T t, T_0\right). \tag{1.12}$$

In the following chapters, the TTS principle is applied extensively to obtain parameters for viscoelastic constitutive models .

1.2 Thermally-activated Shape Memory Effect of Amorphous Polymers

1.2.1 Experimental Characterization

Amorphous SMPs are classified into two major types: chemically cross-linked thermoset and physically cross-linked thermoplastic.[3] Thermoset SMPs show nearly 100% shape recovery but the programmed strain is typically smaller than the thermoplastics which allow as much as 400% programmed engineering strain.[44] This thesis focuses mainly on thermoset SMPs, but the work can be extended for thermoplastic SMPs. To characterize the amorphous SMPs, the experimental techniques described in sec. 1.1.1 are employed. The shape memory performance is investigated under a shape memory cycle (Fig. 1.4). The samples are deformed at high temperature to a specified stress (strain) and

then cooled under constant stress (strain). The samples are then unloaded at low temperatures. Negligible strain recovery occurs during the unloading process since the samples are in their stiff glassy state. The samples are heated upon the transition temperature to recover the permanent shape without constraint, which is referred to as free recovery (unconstrained recovery).[45] In contrast, fixed recovery (constrained recovery) measures the resultant force while the strain is fixed during the recovery process.[45] Other recovery conditions, such as partially constrainedunder a constant load, have also been investigated.[46,47]

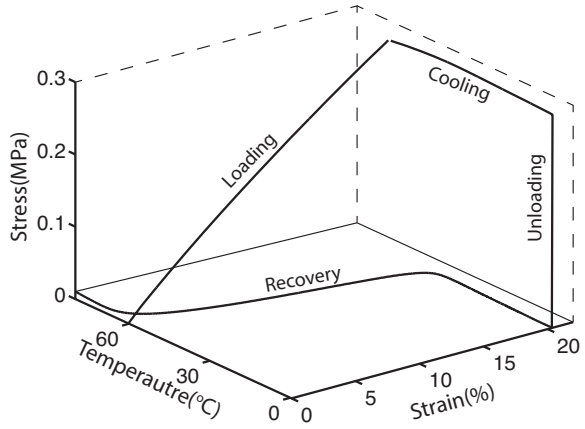

Figure 1.4: Cyclic tests for characterization the shape memory behaviors

The programming temperature has a significant influence on the shape recovery behavior. The SMP samples programmed below T_g have been shown to recover at lower temperatures compared to the samples programmed above T_g.[48–52] During the constrained recovery tests, the cold deformed sample exhibits a larger recovery stress with a lower tem-

perature peak stress in comparison with a hot programmed sample.[49,53–56] In the partially constrained experiments, the samples programmed below T_g exhibited an overshoot in the recovered strain[46,47] while the samples programmed above T_g showed monotonic strain recovery. The response of shape recovery on the deformation temperatures is caused by the broad distribution of the relaxation time, which will be discussed in Chapter 2.

Three-dimensional characterizations of SMPs have also been performed to demonstrate applications of these materials. For example, Yakacki et al.[21] demonstrated the application of shape memory effect to deliver a cardiovascular stent in a minimally invasive manner (Fig. 1.5).

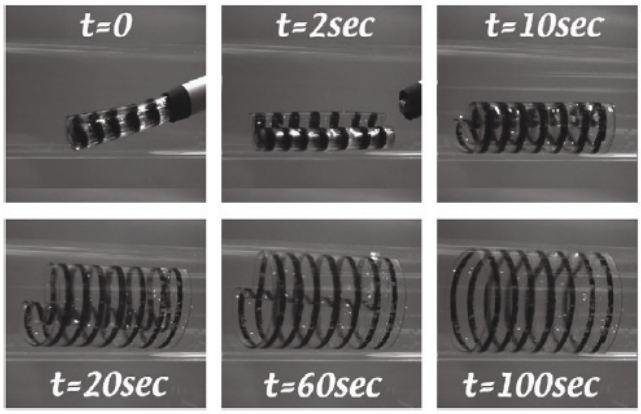

Figure 1.5: Recovery of a SMP stent with T_g^{mid} 52 °C delivered via an 18 Fr. catheter into a 22mm ID glass tube containing body temperature water at 37°C, reprinted with permission from Elsevier[21]

.

1.2.2 Thermoviscoelastic Models

The shape memory fixity and recovery of amorphous polymers are achieved by the tremendous change in chain mobility through the glass transition. Above T_g, the polymer chains have high mobility and can reach their equilibrium state upon loading or deformation. As the temperature decreases, the chains lose their mobility, representing an increase in stiffness and viscosity. Thus, the deformed shape can be stored. To model the shape memory response, recent thermoviscoelastic models[57–61] employ a temperature dependent viscosity or modulus to describe the chain mobility change through the glass transition.

The pioneering work of Tobushi et al.[57,62]was based on a one-dimensional, small strain viscoelastic model and assumed a temperature-dependent modulus. Morshedian et al.[58] used an Arrhenius equation to describe the increase of viscosity with decreasing temperature while Buckley[59] adopted a quadratic function to represent the temperature dependent shift factor. Recently Yu et al.[60] employed a hybrid function to represent the experimentally measured shift factor. The authors adopted WLF equation in the glass transition region while an Arrhenius-type function is used below T_g.

The applications of SMP devices require the development of three-dimensional, finite deformation models that can be implemented into finite element programs to simulate the complex programming and recovery conditions. In the past thirty years, various models have been developed to simulate large deformation viscoelastic-plastic behaviors of amorphous polymers across the glass transition, including Boyce and coworkers,[63–65] Buckley and coworkers,[66,67] Govaert and coworkers,[68,69] as well as Anand and coworkers.[70,71] In

fact, an extension of these models can be applied to simulate shape memory behaviors.[72] To model SMPs, the tremendous change in chain mobility spanning the glass transition region needs to be incorporated into the thermomechanical model. Diani et al.[73] developed the first three-dimensional finite deformation model to represent the thermomechanical behavior of SMPs by an extension of the three element standard solid reological model. The model is composed of an entropy based elastic part and a time dependent viscoelastic part. Diani et al.[74] also applied the relaxation spectrum for shape memory effect by an extension on the generalized Maxwell model to the finite deformation. With the parameters obtained from the master curve of the storage modulus from the TTS principle, the model successfully predicted the torsion shape recovery behaviors of a rectangular beam.

As shown in Sec. 1.1.1, the glass transition is a time dependent kinetic process. As the temperature approaches T_{g}, the polymer structure deviates from of the equilibrium state and continuously evolves towards equilibrium. The structural relaxation has a pronounced effect on mechanical properties and the shape memory response. Thus, Nguyen et al.[45] incorporated both the structural relaxation and stress relaxation into the thermomechanical model. The structural state is represented by the internal variable fictive temperature.[75] The following equation proposed by Tool[75] was applied to represent the structure evolution,

$$\frac{dT_f}{dt} = -\frac{T_f - T}{\tau_R\left(T, T_f\right)}, \tag{1.13}$$

where τ_R is the structural relaxation time.

By evaluating the configurational entropy at fictive temperature T_f instead of at temperature T in eq. 1.7 as proposed by Scherer[76] and Hodge,[42] the relaxation time can be

rewritten as,

$$\tau_R\left(T, T_{\mathrm{f}}\right)=\tau_R^{\mathrm{g}} \exp\left[-\frac{C_1}{\log e}\left(\frac{C_2\left(T-T_{\mathrm{f}}\right)+T\left(T_{\mathrm{f}}-T_{\mathrm{g}}^{\mathrm{ref}}\right)}{T\left(C_2+T_{\mathrm{f}}-T_{\mathrm{g}}^{\mathrm{ref}}\right)}\right)\right]. \tag{1.14}$$

The viscosity was assumed to have the same temperature and structure dependency, and also depends on the flow stress through the Eyring model.[77] This model was able to reproduce the main features of free and constrained recovery behaviors. However, the model overestimated the free recovery rate. Nguyen et al.[78] extended the model to multiple relaxation processes by incorporating stress and structural relaxation spectra. The stress relaxation spectrum was obtained through the master curve of the storage modulus, while the structural relaxation spectrum was assumed to have the same breadth as the stress relaxation spectrum. The multiple relaxation model with the obtained parameters greatly improve the prediction of the unconstrained recovery performance compared to the single relaxation process model. However, the procedures for obtaining the structural relaxation spectrum is oversimplified, resulting in an inaccurate prediction of the recovery performance of programmed specimens after long-term storage.[79] In Chapter 2, an improved experimental procedure to obtain the structural relaxation spectrum will be described. Additionally, the model will be applied to study the effect of deformation temperature and physical aging on the shape-memory behaviors of partially constrained and fixed-strain tests.

1.3 Solvent-induced Shape Memory Effect of Amorphous Polymers

1.3.1 Experimental Observations

The athermal shape recovery of programmed SMP samples in solvent has attracted great interest in the past several years due to its potential applications in biomedical areas[80] (Fig. 1.6). Solvent-induced shape-memory recovery was first reported by Yang et al.[14] The authors observed that polyurethane SMPs lost their shape fixing capability after being exposed to the air for several days due to the moisture diffused into the polymer matrix. The small water molecule acts as plasticizers and increases the chain mobility. The influence of the moisture on the glass transition temperature was measured through DMA and DSC. As shown in Fig. 1.7, the T_g^{mid}, measured from the maximum of $\tan\delta$, decreases with increasing exposing time. After 30 days, T_g^{mid} is close to room temperature, resulting in shape recovery. The uniaxial tension response of polyurethane SMP samples with different water immersion time was also investigated by the same group (Fig. 1.8). With increasing immersion time, the stress response transitions from a stiff viscoplastic with yielding and strain softening to a soft viscoelastic response.

In water or humid environments, shape recovery takes hours or even days, due to the slow diffusion process. Chen et al.[15] introduced the pyridine moieties into polyurethane and demonstrated that the resulting materials had excellent moisture absorption abilities.

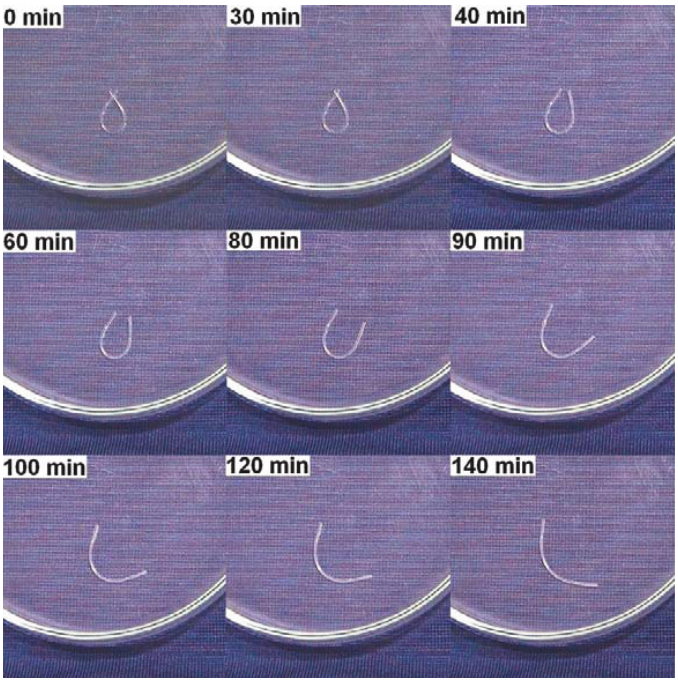

Figure 1.6: Water-driven actuation of a shape-memory recovery of polyurethane SMPs with a circular temporary shape and a linear permanent shape, reprinted with permission from AIP[81]

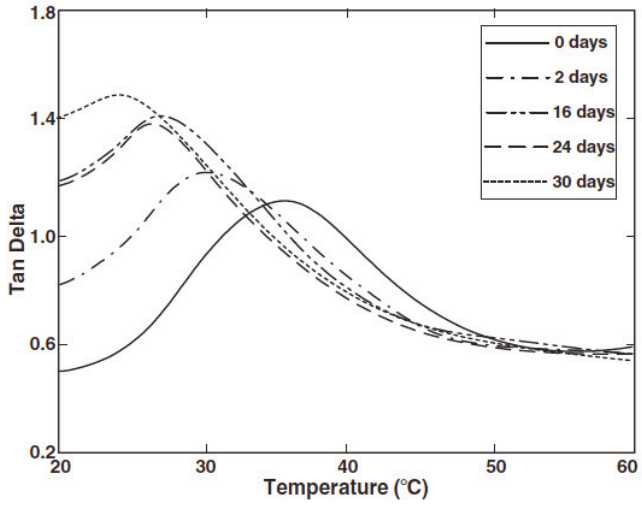

Figure 1.7: Tan δ from DMA tests of polyurethane specimens after exposure to air for different time, reprinted with permission from IOP[82]

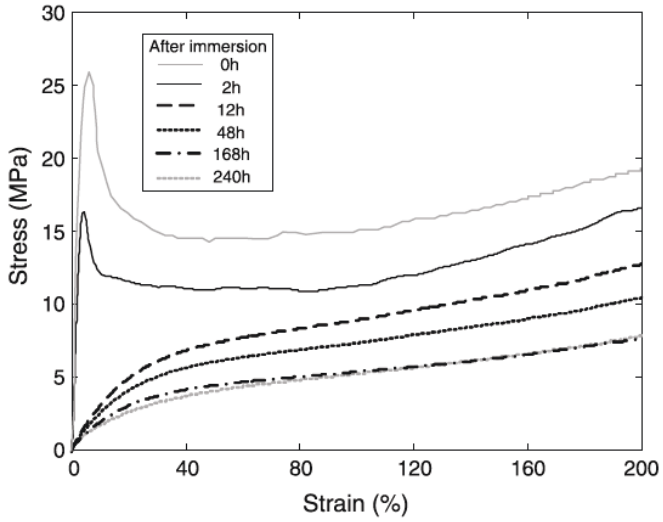

Figure 1.8: Uniaxial tension stress response of polyurethane specimens with different immersion time in water reprinted with permission from Elsevier[83])

The shape recovery time varies from minutes to hours with the difference in the relative humidity, recovery temperature and the chemical compositions. Other polyurethane SMPs with PCL and PEG were reported by Gu et al.[17] , and the materials showed a recovery time from 1.3s to 5 min with variation in the composition and material form (fibrous mats or bulk film). In addition to water, organic solvents have also been employed to achieve shape memory recovery.[16,84] The solvent type has a strong influence on the shape recovery with full recovery in good solvent and partial shape recovery in a poor solvent.

1.3.2 Theoretical Aspects of Solvent Influence on Amorphous Polymers

Compared with various models developed for thermally-activated shape memory effect, few models have been developed for solvent-driven shape memory recovery. One of the main objectives in this thesis is to develop a constitutive model for the influence of solvent on the mechanical properties and shape recovery behaviors. Nevertheless, the introduction of small additives (plasticizers) into the polymer matrix to lower the T_{g} has been extensively investigated.

Several theories have been developed to explain the plasticization effect, for example, the lubricity theory,[85] the gel theory,[85] the free volume theory,[86,87] and the configurational entropy theory.[88] Here the latter two theories described in Sec. 1.1.2 will be extended to incorporate the plasticization effect. In the free volume theory, the major assumption is that adding the plasticizer into the polymer matrix creates new free volume. Thus the eq. (1.1) can be modified as,

$$V_f = V_g + \alpha_f \left(T - T_{\mathrm{gp}}\right) V_p + \gamma_f (T - T_{\mathrm{gs}})(1 - V_p), \tag{1.15}$$

where V_p is the volume fraction of the polymer, T_{gp} and T_{gs} are the glass transition temperatures of polymer and solvent, and γ_f is the materials constant. By assuming that at T_{g} at the free volume is constant. The T_{g} of the polymer and solvent system is,

$$T_{\mathrm{g}} = \frac{\alpha_p T_{\mathrm{gp}} V_p + \gamma_f (1 - V_p) T_{\mathrm{gs}}}{\alpha_p V_p + \gamma_f (1 - V_p)}. \tag{1.16}$$

Kelley and Bueche[86] showed that this approach provided good agreement with the experimentally measured concentration dependence of T_g for a variety of polymer-solvent systems. The viscosity of the polymer-solvent systems can be calculated by substituting eq. (1.15) into the Doolittle equation (eq. (1.2)).

The configurational entropy treatment of the plasticization effect is based on the Dimarzio and Gibbs[88] statistical mechanics theory. The central development of their theory lies in the calculation of the configurational entropy for the polymer-solvent systems. In general, they found an increase in volume fraction of plasticizers, and a decrease in the plasticizer molecular size and molecular stiffness would result in a larger depression of the T_g, which is consistent with experimental observations. Chow[89] extended the work of Dimarzio and Gibbs by developing an explicit expression for the T_g of polymer-solvent systems. His treatment was based on both classical and statistical thermodynamics theory. The model successfully predicted the T_g depression of polystyrene by various diluents. In Chapter 3, this theory is extended to model the solvent-driven shape memory behaviors.

1.4 Physical Aging and Mechanical Rejuvenation of Amorphous Polymers

1.4.1 Experimental Observations

Structural relaxation occurs when polymers are cooled near or below the glass transition temperature. The time for structural rearrangement towards the equilibrium state exceeds the experimental time due to the decrease in chain mobility. Aging at low temperatures, the nonequilibrium structure continuously evolves towards the equilibrium state, representing by the time-dependent properties change, such as density, enthalpy and stiffness.[75,90–93] The more sluggish equilibrium structure also shows more resistance to the mechanical deformation, which represents an increase in the yield strength (Fig 1.9).

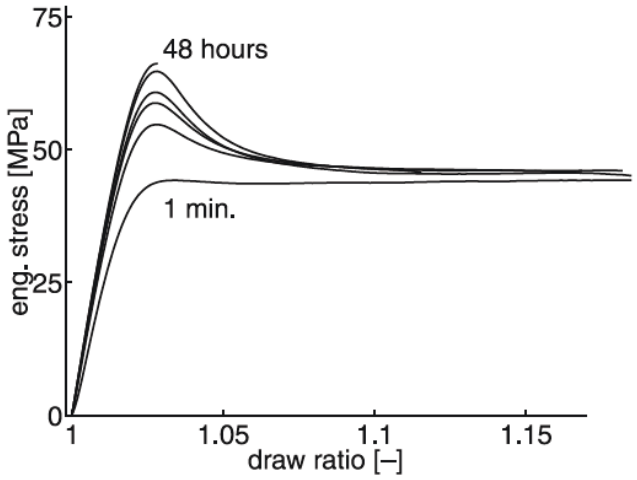

Figure 1.9: Uniaxial tension stress-strain curves of PS specimens at different aging time after rolling, reprinted with permission from Elsevier[94]

.

The aged polymer structure can regain the chain mobility through heating to a high temperature. This process is referred to as thermally rejuvenation. In contrast, mechanical rejuvenation increases the mobility through plastic deformation below T_g, and leads to strain-softening and erases the previous thermal history.[29,95] As shown in Fig. 1.9 , the flow stress of the specimens with different aging times collapses to the same curve. The influence of mechanical rejuvenation on the thermal history can also be observed in the enthalpy measurement.[29] Figure 1.10 shows the DSC curves of quenched and annealed polystyrene specimens after 25% uniaxial compression. The results for both quenched and annealed specimens were nearly identical. The large plastic deformation removed the endothermic overshoot at T_g and produced an exothermic undershoot below T_g.

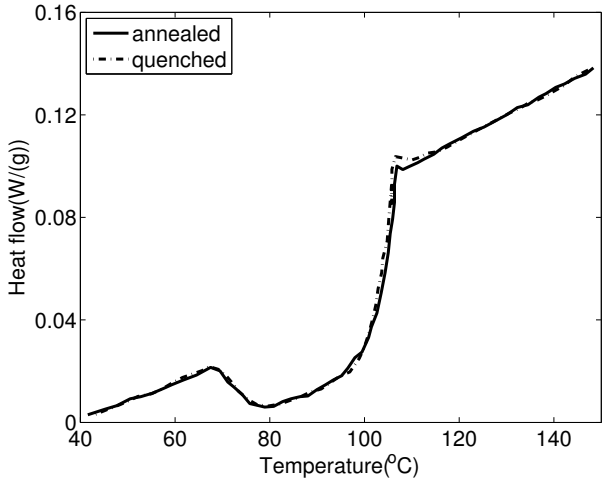

Figure 1.10: DSC scans of the quenched and annealed PS specimens after 25% compression (Data extracted from Hason and Boyce[29])

1.4.2 Modeling Approaches

The fictive (effective) temperature concept introduced by Tool has been widely employed to model the structural relaxation, and the evolution equation (1.13) for T_f proposed by Tool shown has been widely adopted to describe the change in physical properties with structural relaxation. Both phenomenological[96,97] and physical-based approaches[42,98] have been developed for explicit functions of the relaxation time. These models can describe various experimental observations on enthalpy and volume relaxation behaviors. Buckley et al.[99] introduced the fictive temperature as an internal variable to model the mechanical rejuvenation behaviors (strain softening) by assuming T_f evolves with the plastic strain rate $\dot{\bar{\epsilon}}_p$,

$$\frac{dT_f}{dt} = -\frac{1}{\tau_R\left(T, T_f\right)}\left(T_f - T\right) + k\dot{\bar{\epsilon}}_p. \tag{1.17}$$

This model shows good agreement with the experimental results across a wide range of strain rates. However the formulation of the equation is purely empirical. The nonequilibrium thermodynamic theories[100–105] developed in the recent years provide powerful tools to develop constitutive relations and the evolution equation for the effective temperature. The central assumption of the nonequilibrium thermodynamic theories is that the polymer structure is composed of a fast kinetic relaxation process and slow configurational relaxation processes. The kinetic relaxation process can instantaneously attains its equilibrium state, described by thermodynamic state variables temperature and kinetic entropy. The slow relaxation processes fall out of equilibrium near or below T_g and are described by the effective temperature and configurational entropy. Physical aging is a consequence of the

configurational subsystems evolving towards the equilibrium state while mechanical rejuvenation arises from the transfer of the inelastic work into the configurational subsystems. In Chapter 4, a constitutive model is developed based on the nonequilibrium thermodynamics framework to describe the stress-strain response and enthalpy change of specimens with different aging time and pre-plastic deformation.

1.5 Objectives of this Work

The aim of this work is to investigate the thermomechanics of amorphous polymers spanning the glass transition region and to demonstrate that the glass transition behaviors can be exploited to describe the shape memory effect. The work focuses primarily on theory. However, experimental techniques have also been developed to obtain model parameters and to validate the models. There are three specific aims of this work: (1) to develop a constitutive model for thermally-activated shape memory behaviors, (2) to develop a coupled mechanical-diffusion model for solvent-driven shape memory effects, (3) to formulate an effective temperature theory for physical aging and mechanical rejuvenation.

Chapter 2 describes the formation of the constitutive model for the thermally-activated shape memory effect. The model adopted multiple discrete relaxation processes for stress relaxation, structural relaxation and stress-activated viscous flow. Experimental methods were developed to obtain the stress and structural relaxation spectrum, as well as viscoplastic parameters. The model was applied to investigate the partially contained recovery per-

formance of specimens programmed both above and below T_g. The model was also adopted to simulate the deformation temperature influence on the fixed-strain recovery tests.

In Chapter 3, a constitutive model was developed for the effect of solvent absorption on the thermomechanical properties and the shape-memory behavior of amorphous networks. The Adam-Gibbs model was extended to incorporate the influence of solvent concentration on relaxation time. The model was implemented into finite element code. An iterative staggered scheme was applied to couple the mechanical process and the time-dependent diffusion process. The material parameters were obtained through diffusion tests and dynamic mechanical tests of dry and saturate specimens. The model was applied to study the uniaxial tension response of the dry and saturated specimens and the isothermal shape recovery response of rectangular and tube specimens in water of an acrylate-based copolymer.

In Chapter 4, a thermomechanical theory was developed to model the nonequilibrium behaviors of amorphous polymers. The theory introduced the effective temperature as a thermodynamic state variable to represent the nonequilibrium structure. Based on the nonequilibrium thermodynamic framework, the effective temperature was coupled with the inelastic work. The theory was applied to study the effect of temperature, strain rate, aging time and plastic pre-deformation on the uniaxial stress response and enthalpy change of an acrylate-based polymer.

To conclude, Chapter 5 first summarizes the key results and main contributions of this work. Based on the results of the thesis, it will demonstrate how to exploit the glass transi-

tion behaviors to achieve specific shape memory behaviors. The limitations of the work is also discussed. The chapter ends with a discussion of future research directions.

The appendix contains the information on experimental analysis and finite element implementation. Appendix A describes a detailed procedure of obtaining the broad viscoelastic spectrum through time-temperature superposition of the stress relaxation tests. The method shows the ability to accurately obtain the discrete relaxation spectrum of Nafion spanning 24 decades of log time. The spectrum is then employed by a simple finite deformation model to simulate the temperature memory effect and multiple shape memory effect of Nafion. Appendix B includes the ongoing work of implementing the thermomechanical coupled model developed in Chapter 4 into a finite element program. This part provides the general procedures to implement a user-defined element subroutine into a finite element program. It starts with the strong form of the balance of momentum and balance of energy. It then describes the detailed steps to obtain the weak form and matrix form. The coupled fields are solved using a Newton Raphson method. The explicit function of the element-level residuals and the tangent modulus are also provided.

Chapter 2

Modeling the Thermally Activated Shape-Memory Behavior

This chapter has been reprinted from R. Xiao, J. Choi, N. Lakhera, C. Yakacki, C. Frick, and T. Nguyen, "Modeling the glass transition of amorphous networks for shape-memory behavior ", Journal of the Mechanics and Physics of Solids, Vol. 161, Pages 1612-1635, 2013, with permission from Elsevier.[106]

In this chapter, a thermomechanical constitutive model was developed for the time-dependent behaviors of the glass transition of amorphous networks. The model used multiple discrete relaxation processes to describe the distribution of relaxation times for stress relaxation, structural relaxation, and stress-activated viscous flow. A non-equilibrium thermodynamic framework based on the fictive temperature was introduced to demonstrate the thermodynamic consistency of the constitutive theory. Experimental and theoretical

methods were developed to determine the parameters describing the distribution of stress and structural relaxation times and the dependence of the relaxation times on temperature, structure, and driving stress. The model was applied to study the effects of deformation temperatures and physical aging on the shape-memory behavior of amorphous networks. The model was able to reproduce important features of the partially-constrained recovery response observed in experiments. Specifically, the model demonstrated a strain-recovery overshoot for cases programmed below T_g and subjected to a constant mechanical load. This phenomenon was not observed for materials programmed above T_g. Physical aging, in which the material was annealed for an extended period of time below T_g, shifted the activation of strain recovery to higher temperatures and increased significantly the initial recovery rate. For fixed-strain recovery, the model showed a larger overshoot in the stress response for cases programmed below T_g, which was consistent with previous experimental observations. Altogether, this chapter demonstrates how an understanding of the time-dependent behaviors of the glass transition can be used to tailor the temperature and deformation history of the shape-memory programming process to achieve more complex shape recovery pathways, faster recovery responses, and larger activation stresses.

2.1 Introduction

Shape-memory behavior in polymers describes the ability to store a programmed shape indefinitely and fully recover to an original shape in response to an environmental trigger.

CHAPTER 2. MODELING THE THERMALLY ACTIVATED SHAPE-MEMORY BEHAVIOR

Shape-memory polymers (SMPs) are classified by their structure and triggering mechanisms, and numerous review articles have described the structure, functional capabilities, and potential applications of a wide variety of SMP materials and composites.[2,5,107–109] The materials are attractive for medical applications because they can be designed for biocompatibility, biodegradability, and controlled drug delivery. Moreover, they can store and recover large deformation, which is desirable for deployable and morphing structures.[110]

For amorphous networks, shape-memory behavior is realized by programming around the glass transition temperature, T_g.[1,107,111] In a typical shape-memory cycle, the material is heated above T_g, deformed to the desired shape, then cooled rapidly below the T_g to fix the programmed shape for indefinite storage. This shape-memory programming process is a hot deformation process, similar to hot-drawing and hot-embossing, that takes advantage of the large change in the material stiffness through the glass transition to apply large deformations at low stresses. Alternatively, the material can be deformed in the glassy state below T_g to achieve the programmed shape. The cold deformation process obviates the temperature cycle for materials with a T_g above room temperature, and can provide significant time and cost savings.

Studies of the unconstrained recovery response of materials programmed below T_g have shown little qualitative difference with those programmed above T_g, though the recovery temperature was generally lower for cold deformed specimens.[48–52] For fixed-strain recovery response, the cold compression cases exhibited a larger stress overshoot compared to cases programmed at higher temperatures.[49,53,54,56] The recent study of Lakhera et al.[46]

reported significant differences in the strain recovery response under a constraining stress. Those programmed above T_g recovered monotonically from the programmed strain to the equilibrium strain determined by the constraining stress and rubbery modulus. Materials programmed below T_g exhibited an overshoot in the recovered strain that paradoxically increased with the constraining stress. The overshoot in strain recovery may be an important factor in designing the fit and tolerance of deployable structures and actuators.

The objective of this study is to develop a constitutive model for amorphous SMPs to investigate the mechanisms underlying the recovery response under various mechanical constraints as well as the dependence of the recovery response on the temperature and deformation history of the programming process. Modeling the shape-memory effect of amorphous networks requires modeling the temperature-dependent and time-dependent behaviors of the glass transition. Several approaches have been proposed for modeling the glass transition behaviors of amorphous SMPs[45,72,78,112–115] and more generally of amorphous polymers.[65–67,116] Our focus has been to develop a thermoviscoelastic approach that described the change in the relaxation behaviors with temperature, structure, and driving stress. Our earliest effort[45] used a single relaxation process to represent the stress and structural relaxation mechanisms of the glass transition. We assumed that the stress and structural relaxation times share the same temperature and structure dependence described by the nonlinear Adam-Gibbs relation.[39] Yielding and viscoplastic flow of the glassy material below T_g was described by a single stress-activated Eyring process.[77] Including structural relaxation allowed the model to accurately predict the stress-temperature response in

fixed-strain recovery experiments; however, it severely underestimated the recovery time measured in unconstrained recovery experiments. Chen and Nguyen[117] showed that the recovery rate in unconstrained recovery is primarily determined by the viscoelastic properties which cannot be adequately described by a single relaxation process. To address the deficiencies of the single-process model, Nguyen et al.[78] introduced an extension that incorporated multiple stress and structural relaxation processes. The multi-process model provided improved predictions for the recovery time, which demonstrated the importance of viscoelasticity to the unconstrained shape recovery response; however, it did not describe yielding in the stress response and could not be applied to study the effect of deformation processing below T_g. Li and Xu[52] developed a model to investigate the unconstrained recovery response of amorphous SMPs programmed by cold compression that employed a continuous structural relaxation spectrum but only a single process to describe viscous flow.

In this paper, we extend the multi-process model of Nguyen et al.[78] to include stress-activated viscous flow and yielding below T_g and introduce a thermodynamic framework for a fully coupled thermomechanical theory. In general, there are two approaches for applying multiple stress-activated flow processes to model yielding in glassy polymers. Tervoort et al.[118] and coworkers used a coupled formulation, in which all of the flow processes depended on a single activation stress, while Dooling and Buckley[119] and coworkers proposed a decoupled formulation that assumed a discrete spectrum of activation stresses corresponding to the spectrum of relaxation times. We adopt the coupled formulation with a single activation stress for its economy and show that this is sufficient to accurately pre-

dict the rate-dependent and temperature-dependent yield and post-yield behavior through the glass transition. A challenge in modeling multiple relaxation processes is determining the parameters of the stress and structural relaxation spectrum. For the structural relaxation spectrum, we present an isothermal recovery test that measures the time-dependent thermal contraction response to successive rapid temperature decreases in the glass transition region, and apply the method of reduced variables to shift the time-dependent response of each temperature step to construct a master curve for the structural relaxation function. We then show that the shift factor measured for the stress relaxation function can be used to determine the shift factor for the structural relaxation function, which validates the modeling assumption that the structural and stress relaxation behavior of the polymer networks share the same temperature dependence. Lastly, we apply the model to study the fixed-strain and partially constrained recovery response of specimens programmed below and above T_g. In particular, we examine the importance of the stress relaxation spectrum in determining the strain overshoot during partially constrained recovery and the stress overshoot during fixed-strain recovery for materials deformed below T_g.

2.2 Experimental Methods

2.2.1 Materials and Specimen Preparations

Tert-butyl acrylate (*t*BA) poly(ethylene glycol) dimethacrylate (PEGDMA), with typical molecular weight M_n = 550, di(ethylene glycol) dimethacrylate (DEGDMA) , and photoinitiator 2,2-dimethoxy-2-phenylacetophenone (DMPA) were ordered from Sigma Aldrich and used in their as-received condition. A crosslinker solution (XLS) was synthesized by mixing 30 wt % DEGDMA with 70 wt% PEGDMA. Comonomer solutions were prepared by mixing 10, 20, and 40 wt% XLS with the tBA monomer solution to create three networks of equal T_g and varying crosslinking density once polymerized. The photoinitiator, 2,2-dimethoxy-2-phenylacetophenone, was added to the comonomer solution at a concentration of 0.1 wt% of the total comonomer weight and mixed manually until fully dissolved. The polymer solution was injected between two glass slides separated by a 1 mm spacer to create film specimens for tensile tests or into cylindrical polyethylene molds for compression tests. Polymerization was achieved by exposing the mixture to UV light (Blak Ray B100 A/R) for 15 minutes. For the cylindrically molded specimens, the solution was submerged in ice water to slow the rate of polymerization and avoid cracking in the molds. Following UV curing, all polymer specimens were thermally cured in an oven at 90 ^{o}C for one hour to ensure complete polymerization. The films specimens were cut to dimensions 1.0 mm x 5.0 mm x 25.0 mm using a laser cutter. The cylindrical specimens were machined to 10 mm in diameter. These were cut to 15 mm in length and sanded to

provide smooth surfaces for uniaxial compression tests.

2.2.2 Thermomechanical Experiments

The thermomechanical properties of unprogrammed tBA-co-XLS materials were characterized using four sets of experiments. Constant cooling rate tests were performed to determine the volumetric coefficients of thermal expansion (CTE) and the T_g at a reference cooling rate. The frequency-dependence of the storage modulus was measured using dynamic frequency sweep at multiple temperatures, and the results were shifted in the frequency domain using the time-temperature superposition principle to construct the master curve of the stress relaxation function and determine the temperature dependence of characteristic relaxation time. To characterize the structural relaxation response, we developed an isothermal recovery test that measured the time-dependent volumetric thermal contraction response to a series of rapid temperature decreases and applied the method of reduced variables to construct a master curve for structural relaxation function. The temperature-dependent and rate-dependent yield strength was measured using isothermal uniaxial compression experiments.

2.2.2.1 Coefficients of Thermal Expansion

To determine the volumetric CTEs at a reference glass transition temperature T_g^{ref}, constant cooling rate tests were performed on the film specimens under uniaxial tension using a TA Q800 Dynamic Mechanical Analyzer (DMA) set to zero force mode. The specimens

were equilibrated at 110 °C and cooled to 0 °C at 1 °C /min. The experiments measured the thermal contraction in length, defined as the change in length over the original length, as a function of temperature. The rubbery volumetric CTE, α_r, was determined as 3 times the slope of thermal strain-temperature curve between 80 °C and 100 °C, and the glassy CTE, α_g, was determined as 3 times the slope of the curve between 0 °C and 20 °C. The glass transition temperature, T_g^{ref}, for the cooling rate 1 °C /min was determined from the intersection of the glassy and rubbery CTE lines. The glass transition measured in a CTE test corresponds to the onset glass transition temperature measured in a dynamic temperature sweep test at fixed frequency.[78]

2.2.2.2 Dynamic Frequency Sweep Tests at Different Temperatures

The viscoelastic properties of polymers in the glass transition region strongly depend on the temperature at which they are measured. The time temperature superposition (TTS) principle describes the simple relationship between time/frequency and temperature for the viscoelastic behavior of thermorheologically simple materials. The TTS principle states that the shape of the frequency response function does not change with temperature. The frequency-dependent storage modulus, $G(w)$, measured at two temperatures, T and T_0, are related by a horizontal logarithmic shift along the frequency axis as follows,

$$G(\log\omega, T) = G(\log\omega + \log a_T(T),\ T_0) \tag{2.1}$$

where $a_T(T)$ is the temperature-dependent shift factor measured from the reference temperature T_0. The temperature dependence of the shift factor was described using Williams

Landel Ferry (WLF) equation [27, Chapter 11],

$$\log a_T = \frac{-C_1^0(T - T_0)}{C_2^0 + T - T_0} \tag{2.2}$$

where C_1^0 and C_2^0 are the WLF constants at the reference temperature T_0.

Dynamic frequency sweep tests were performed on the film specimens using the DMA in multifrequency mode. The polymer film specimens were heated from 0 °C to 120 °C in 5°C increments. The specimens were annealed at each test temperature for 5 minutes to allow for complete heat conduction through the sample, then subjected to a 0.2% dynamic strain at 0.32 Hz, 1.0 Hz, 3.2 Hz, 10.0 Hz, and 31.6 Hz. The storage modulus as a function of frequency was measured at each temperature then shifted to a reference temperature, $T_0 = 75$°C, using the method described in Ferry.[27] This procedure provided a master curve for $G(\omega, T_0)$, which was used to determine the parameters of the viscoelastic relaxation spectrum and the temperature-dependence of $a_T(T)$. To determine the WLF constants, $(T - T_0)/\log a_T$ was plotted as a function of $T - T_0$ and a line was fitted to data between 40°C and 80°C. These temperatures corresponded to the onset of the glassy and rubbery plateaus for the frequency range of the experiments. From eq. (2.2), the WLF constants can be calculated from the slope m and intercept a of the linear fit as,

$$C_1^0 = -\frac{1}{m}, \quad C_2^0 = \frac{a}{m}. \tag{2.3}$$

Finally, the WLF constants for T_0 was shifted to T_g^{ref} to give,

$$C_2^{\mathrm{g}} = C_2^0 + T_{\mathrm{g}}^{\mathrm{ref}} - T_0, \quad C_1^{\mathrm{g}} = \frac{C_1^0 C_2^0}{C_2^{\mathrm{g}}} \tag{2.4}$$

2.2.2.3 Isothermal Recovery

Structural relaxation describes the time-dependent process in which an amorphous material in a nonequilibrium configuration evolves towards equilibrium. The mechanical effects of structural relaxation can be observed in isothermal volume recovery tests, where a material in equilibrium is subjected to an instantaneous temperature change ΔT. The temperature jump induces a time-dependent volumetric deformation from an instantaneous value, $\Delta_0 = \alpha_{\mathrm{g}} \Delta T$, to an equilibrium value, $\Delta_\infty = \alpha_{\mathrm{r}} \Delta T$. Structural relaxation in polymers occurs too slowly at low temperatures, $T \ll T_{\mathrm{g}}$, to be measured completely in a single experiment and too quickly for $T \gg T_{\mathrm{g}}$ to be measured reliably using the DMA. Thus, we developed the test described below to measure the non-equilibrium volumetric deformation, $\delta(t, T)$, for consecutive rapid temperature decreases in the glass transition region then shifted the results in logarithmic time to form a master curve for the structural relaxation function at $T_{\mathrm{g}}^{\mathrm{ref}}$.

The DMA was set to zero-force mode to measure the length change of the film specimens in response to a rapid change in temperature. Samples were equilibrated at $T = 70°\mathrm{C}$ for 30 minutes then cooled either to $T_{\mathrm{g}}^{\mathrm{ref}} + 8^{\mathrm{o}}\mathrm{C}$ or $T_{\mathrm{g}}^{\mathrm{ref}} + 6^{\mathrm{o}}\mathrm{C}$ at 1°C/min and equilibrated for 60 minutes. The specimens were subjected to subsequent temperature decrements of $4^{\mathrm{o}}\mathrm{C}$ at 6°C/min and held for 60 minutes at each temperature step until either $T_{\mathrm{g}}^{\mathrm{ref}} - 8^{\mathrm{o}}\mathrm{C}$ or

$T_g^{ref} - 10^oC$ was reached. The total volumetric deformation, $\Delta(t,T)$, was approximated as three times the linear thermal contraction of the film measured from the beginning of the test, at either to $T_g^{ref} + 8^oC$ or $T_g^{ref} + 6^oC$, and the nonequilibrium volumetric deformation for the nth step was calculated as,

$$\delta(t,T_n) = \Delta(t,T_n) - \sum_{j=1}^{n} \alpha_r \Delta T_j, \quad t_{n-1}^{+} < t \leq t_n^{-}. \tag{2.5}$$

In the following developments, we assumed the cooling rate of each temperature step was sufficiently fast such that it can be be neglected and $\delta(t,T_n)$ in eq. (2.5) represents the nonequilibrium volumetric deformation resulting from n instantaneous temperature jumps.

For thermorheologically simple materials, the structural relaxation function, ρ, measured at different temperatures superpose when plotted as a function of reduced time,[120]

$$\rho(\log t,T) = \rho(\log u(T,\delta(t,T))), \quad u = \int_0^t \frac{dt}{a(T,\delta(t,T))}, \tag{2.6}$$

where $a(T,\delta)$ is the time-dependent and structure-dependent shift factor. The nonlinear Adam-Gibbs equation[39,42,45,121] was used to describe the shift factor for T_g^{ref} as the reference temperature,

$$a(T,\delta) = \exp\left[-\frac{C_1^g}{\log e}\left(\frac{C_2^g\left(T - T_f(\delta)\right) + T\left(T_f(\delta) - T_g^{ref}\right)}{T\left(C_2^g + T_f(\delta) - T_g^{ref}\right)}\right)\right], \quad T_f(\delta) = T + \frac{\delta}{\Delta\alpha}, \tag{2.7}$$

where C_1^g and C_2^g are the WLF constant determined from the dynamic frequency sweep tests for the storage modulus, T_f is the fictive temperature,[122] and $\Delta\alpha = \alpha_r - \alpha_g$. At equilibrium, when $\delta = 0$, the shift factor $a(T,\delta)$ reduces to the WLF shift factor $a_T(T)$. In the test, the thermal deformations may not reach equilibrium at the end of each temperature step,

particularly for the lower temperatures, and the residual nonequilibrium deformations from prior temperature steps may contribute to the response function at the current temperature step. Neglecting the effect of the finite cooling rate, the total nonequilibrium deformation after n consecutive temperature steps ΔT can be evaluated from the response function as,

$$\delta\left(t, T_n\right) = \sum_{j=1}^{n} \Delta\alpha \Delta T_j \rho\left(u\left(t, T_n\right) - u_{j-1}\right), \quad t_{n-1}^{+} < t \leq t_n^{-}. \tag{2.8}$$

where $u_j\left(t_j, T_j\right)$ is the reduced time in eq. (2.6) evaluated at temperature T_j and time t_j at the end of the jth hold period, and $u_0 = 0$ for $j = 1$. The nonequibrium volumetric deformation at the end of $n-1$ hold period is,

$$\delta(t_{n-1}^{-}, T_{n-1}) = \sum_{j=1}^{n-1} \Delta\alpha \Delta T_j \rho\left(u_{n-1} - u_{j-1}\right). \tag{2.9}$$

Subtracting eq. (2.9) from eq. (2.8), gives:

$$\begin{aligned}\delta\left(t, T_n\right) - \delta(t_{n-1}^{-}, T_{n-1}) &= \Delta\alpha \Delta T_n \rho\left(u\left(t, T_n\right) - u_{n-1}\right) \\ &+ \sum_{j=1}^{n-1} \Delta\alpha \Delta T_j \left[\rho\left(u\left(t, T_n\right) - u_{j-1}\right) - \rho\left(u_{n-1} - u_{j-1}\right)\right], \quad t_{n-1}^{+} < t \leq t_n^{-}, \end{aligned} \tag{2.10}$$

where the summation describes the evolution of the non-equilibrated deformations from prior temperature steps. Assuming that the non-equilibrated strain at the end of hold period does not evolve signiï£¡cantly further towards equilibrium for the duration of the test the structural relaxation relaxation function for each hold period can be calculated from the measured nonequilibrium volumetric deformation as,

$$\rho\left(u - u_{n-1}\right) = \frac{1}{\Delta\alpha \Delta T_n}\left(\delta\left(u\right) - \delta(u_{n-1})\right), \quad u_{n-1} < u \leq u_n. \tag{2.11}$$

This assumption is reasonable because the relaxation time increases with decreasing temperature and structure δ. Neglecting the evolution of the residual nonequilibrium deformation of prior steps led to a maximum error of 3% for the temperature range and hold period of the test for all three materials.

2.2.2.4 Isothermal Uniaxial Compression Experiment

The isothermal uniaxial compression experiments were performed on the cylindrical specimens using the MTS 810 equipped with an Eurotherm 2404 temperature controller. The specimens were subjected to a heat treatment immediately prior to testing to remove the effects of physical aging. Specifically, the specimens were heated in the environmental chamber from room temperature to 80 ^{o}C, equilibrated for 20 minutes, cooled to the test temperatures at 3 ^{o}C/min, and held for 20 min to ensure complete heat conduction through the specimen. The specimens were compressed to 30% engineering strain at 3 strain rates, $0.003/\mathrm{s}, 0.01/\mathrm{s}$, and $0.03/\mathrm{s}$, to measure the yield and post-yield softening response. The experiments were performed at 10 ^{o}C, 25 ^{o}C, 40 ^{o}C, 55 ^{o}C and 70 ^{o}C, which corresponded to a temperature range of $T_{\mathrm{g}}^{\mathrm{ref}} \pm 30°\mathrm{C}$.

2.2.3 Partially Constrained Recovery Experiment

The partially constrained recovery experiments were performed on the cylindrical specimens using an MTS Mini Bionix II equipped with an MTS 651 environmental chamber and MTS LX 500 laser extensometer.[46] Samples were either heated to 70 ^{o}C (above T_{g})

or cooled to 20 °C (below T_g) and held for 20 minutes to ensure complete heat conduction through the specimens. The specimens were compressed to 30% engineering strain at a slow strain rate of $10^{-3}s^{-1}$ and allowed to relax for 20 minutes. Following stress relaxation, the specimens were cooled to 0°C without removing the compression platens at a rate of 5°C /min and held isothermally for about 10 minutes. The stress decreased to zero during annealing, which indicated that the specimens detached from the platens. A constraining stress, which corresponded to a fraction of the engineering stress required to deform the specimens to 30% at 70°C, was applied, and the specimens were heated to 100°C at 2 °C /min. The same constraining stress was applied to specimens programmed above and below T_g. The strain recovered under the constraining stress was measured as a function of temperature.

2.3 Constitutive Model

The following presents a constitutive model for amorphous polymers near the glass transition, that integrates the time-dependent mechanisms of viscoelasticity, structural relaxation, and stress-activated yield and post-yield flow. The theoretical foundation and development of the thermoviscoelastic model was described in detail in Nguyen et al.[45] and Nguyen et al.[78] Here, we summarize the constitutive relations and develop an extension that uses discrete distributions of relaxation processes to describe the three time-dependent mechanisms. Finally, we introduce a thermodynamic framework for a fully coupled ther-

momechanical theory.

Consider a body with an undeformed configuration initially in thermodynamic equilibrium at time t_i and temperature T_i. The deformation gradient $\mathbf{F}$ maps lines in the undeformed configuration to the deformed configuration at time t and temperature T. We assume that the deformation gradient can be decomposed multiplicatively into an isotropic thermal component $\mathbf{F}_{\mathrm{T}} = J_{\mathrm{T}}^{1/3}\mathbf{1}$ and a mechanical component $\mathbf{F}_{\mathrm{M}}$,[123,124]

$$\mathbf{F} = J_{\mathrm{T}}^{1/3}\mathbf{F}_{\mathrm{M}}, \tag{2.12}$$

A polymer network responds to a temperature change by first undergoing an instantaneous volume change followed by a slower relaxation towards an equilibrium volume through configurational rearrangements. The configurational entropy decreases with temperature and vanishes entirely at the equilibrium temperature T_2 of the ideal glass;[34] however the equilibrium structure at T_2 cannot be realized because the molecular mobility also decreases with temperature and the configurational entropy.[39] This causes the polymer structure to become kinetically trapped in a quasi-equilibrium state at a fictive temperature $T_f > T$ during cooling. To model this structural relaxation process, we decompose the thermal deformation into an instantaneous part given by $(T - T_i)$ and a departure from the instantaneous response, $\bar{\delta}$, given by $\left(T_f - T_i\right)$,

$$J_{\mathrm{T}} = \exp\left[\alpha_g \left(T - T_i\right)\right] \exp \underbrace{\left[\Delta\alpha \left(T_f - T_i\right)\right]}_{\bar{\delta}}, \tag{2.13}$$

where α_g is the glassy volumetric CTE, α_r is the rubbery volumetric CTE, and $\Delta\alpha =$

$\alpha_r - \alpha_g$. For polymers, structural relaxation is characterized by a broad spectrum of relaxation times, and previous works showed that this feature is needed to capture the activation temperature and recovery rate of unconstrained shape recovery.[78,117] We assume that the distribution of relaxation times can be attributed to different molecular substructures. Furthermore, the relaxation mechanisms of the substructures are weakly coupled, such that the substructures can be considered to be in quasi-equilibrium at different fictive temperatures T_{f_k}. The fictive temperature of each substructure is associated with a partial thermal deformation $\bar{\delta}_k$, defined as

$$\bar{\delta}_k = \Delta\alpha_k \left(T_{f_k} - T_i\right), \tag{2.14}$$

where $\Delta\alpha_k$ are the partial volumetric CTEs. The partial deformations sum to the total departure from the instantaneous response, $\sum_{k=1}^{P} \bar{\delta}_k = \bar{\delta}$; thus $\sum_{k=1}^{P} \Delta\alpha_k = \Delta\alpha$. A generalization of Tool's equation[122] can be used to describe evolution of the fictive temperatures,[125]

$$\frac{\partial T_{f_k}}{\partial t} = -\frac{1}{\tau_{R_k}\left(T, T_f\right)}\left(T_{f_k} - T\right), \quad T_{f_k}(0) = T_i, \tag{2.15}$$

where τ_{R_k} is the structural relaxation time of the kth relaxation process. We assume the relaxation times depend on the temperature and the overall network structure through T_f rather than T_{f_k} of the substructures, which causes eq. (2.15) to be a coupled system of differential equations. The evolution equation can be written in terms of the partial deformations using eq. (2.14) as,

$$\frac{\partial \bar{\delta}_k}{\partial t} = -\frac{1}{\tau_{R_k}\left(T, T_f\right)}\left(\bar{\delta}_k - \Delta\alpha_k\left(T - T_i\right)\right), \quad \bar{\delta}_k(0) = 0, \tag{2.16}$$

which is equivalent to the KAHR model[120] for isobaric volume recovery of glasses. The

nonlinear Adam-Gibbs model[39,42,45,98,121] is adopted here to describe the structural relaxation time in terms of WLF constants and glass transition temperature,

$$\tau_{R_k}\left(T, T_{\mathrm{f}}\right) = \tau_{R_k}^{\mathrm{g}} \exp\left[-\frac{C_1}{\log e}\left(\frac{C_2\left(T - T_{\mathrm{f}}\right) + T\left(T_{\mathrm{f}} - T_{\mathrm{g}}^{\mathrm{ref}}\right)}{T\left(C_2 + T_{\mathrm{f}} - T_{\mathrm{g}}^{\mathrm{ref}}\right)}\right)\right]. \tag{2.17}$$

The parameters $\tau_{R_k}^{\mathrm{g}}$ and $\Delta\alpha_k$ together characterize the discrete structural relaxation spectrum.

To model viscoelastic behavior, the mechanical deformation gradient $\mathbf{F}_{\mathrm{M}}$ is decomposed further multiplicatively into N parallel elastic and viscous parts,

$$\mathbf{F}_{\mathrm{M}} = \mathbf{F}_k^{\mathrm{e}}\mathbf{F}_k^{\mathrm{v}}, \quad for \quad k = 1...N, \tag{2.18}$$

where each $\mathbf{F}_k^{\mathrm{v}}$ maps to a stress-free intermediate configuration. We assume that the stress response of an amorphous network arises from two primary mechanisms: the decrease in the configurational entropy with deformation and the increase in internal energy from local intermolecular interactions. The entropic mechanism dominates at high temperatures, where the chains can quickly rearrange to an equilibrium configuration in response to deformation. At low temperatures, the vanishing molecular mobility prevents configurational rearrangements, and the local intermolecular interactions become important. To describe the interaction of these mechanisms, the Cauchy stress response is decomposed additively into an equilibrium deviatoric component, N nonequilibrium deviatoric components, and a corresponding volumetric component:

$$\mathbf{s} = \mathbf{s}^{\mathrm{eq}} + \underbrace{\sum_{k}^{N} \mathbf{s}_k^{\mathrm{neq}}}_{\mathbf{s}^{\mathrm{neq}}} + \mathbf{p} \tag{2.19}$$

The Arruda-Boyce eight chain model[126] is used to describe the high temperature entropic response,

$$\mathbf{s}^{\mathrm{eq}} = \frac{1}{J}\mu^{\mathrm{eq}} \left(\overline{\mathbf{b}}_{\mathrm{M}} - \frac{1}{3}\overline{I}_{\mathrm{M1}}\mathbf{I}\right), \quad \mu^{\mathrm{eq}} = \frac{\mu_{\mathrm{N}}}{3}\frac{T_f}{T_0}\frac{\lambda_{\mathrm{L}}}{\overline{\lambda}_{\mathrm{eff}}}\mathcal{L}^{-1}\left(\frac{\overline{\lambda}_{\mathrm{eff}}}{\lambda_{\mathrm{L}}}\right), \tag{2.20}$$

where $\overline{\mathbf{b}}_{\mathrm{M}} = J_{\mathrm{M}}^{-2/3}\mathbf{b}_{\mathrm{M}}$, $J_{\mathrm{M}} = \det[\mathbf{F}_{\mathrm{M}}]$, and $\overline{I}_{\mathrm{M1}} = \overline{\mathbf{b}}_{\mathrm{M}} : \mathbf{1}$. The $\mathcal{L}(u) = \coth u - u^{-1}$ is the Langevin function, $\overline{\lambda}_{\mathrm{eff}} = \sqrt{\frac{1}{3}\overline{I}_{\mathrm{M_1}}}$ is the effective chain stretch of the network, and λ_{L} is the locking stretch. The parameter μ_{N} describes the characteristic stiffness of the polymer network measured at T_0. At thermodynamic equilibrium, $T_f = T$ and the rubbery shear modulus of the undeformed material is given by $\mu_r = \frac{\mu_N}{3}T/T_0\mathcal{L}^{-1}(1/\lambda_L)$.

The neo-Hookean model is applied to describe the nonequilibrium stress response,

$$\mathbf{s}_k^{\mathrm{neq}} = \frac{1}{J}\mu_k^{\mathrm{neq}} \left(\overline{\mathbf{b}}_k^{\mathrm{e}} - \frac{1}{3}\overline{I}_{1_k}^{\mathrm{e}}\mathbf{I}\right), \tag{2.21}$$

where $\overline{\mathbf{b}}_k^{\mathrm{e}} = J_k^{\mathrm{e}^{-2/3}}\mathbf{b}_k^{\mathrm{e}}$, $J_k^{\mathrm{e}} = \det\left[\mathbf{F}_k^{\mathrm{e}}\right]$, and $\overline{I}_{1_k}^{\mathrm{e}} = \overline{\mathbf{b}}_k^{\mathrm{e}} : \mathbf{1}$. The shear modulus of the undeformed material for the glassy response is given by $\mu_g = \mu_r + \sum_k^N \mu_{\mathrm{k}}^{\mathrm{neq}}$. Finally, the pressure is described by

$$p = \frac{1}{2J}\kappa(J_{\mathrm{M}}^2 - 1), \tag{2.22}$$

where κ is the bulk modulus in the undeformed configuration. The evolution of the internal variable $\mathbf{b}_{\mathrm{M}_k}^e$ to equilibrium is described by the following nonlinear flow rule,[127]

$$-\frac{1}{2}\mathcal{L}_v\mathbf{b}_k^e\mathbf{b}_k^{\mathrm{e\text{-}1}} = \frac{1}{2\upsilon_{\mathrm{S}k}\left(T, T_f, s\right)}\mathbf{s}_k^{\mathrm{neq}}, \tag{2.23}$$

where υ_{S_k} is the shear viscosity. The Lie derivative[128] of the left elastic deformation tensor, defined as $\mathcal{L}_v \mathbf{b}_k^{\mathrm{e}} = -2\mathbf{F}_k^{\mathrm{e}}\mathbf{D}_k^{\mathrm{v}}\mathbf{F}_k^{\mathrm{e}^{\mathrm{T}}}$, is the push forward of the viscous rate of deformation tensor, $\mathbf{D}_k^{\mathrm{v}} = \mathrm{sym}\left[\dot{\mathbf{F}}_k^{\mathrm{v}}\mathbf{F}_k^{\mathrm{v}^{-1}}\right]$, to the deformation configuration. As shown in Sec. 2.3.1, the Lie derivative is the thermodynamic conjugate of the nonequilibrium stress response $\mathbf{s}_k^{\mathrm{neq}}$.

We assume that the viscosities describing the resistance to viscous flow and the structural relaxation times share the same dependence on temperature and structure. The viscosities also depend on the total flow stress $s = \sqrt{\frac{1}{2}\mathbf{s}^{\mathrm{neq}} : \mathbf{s}^{\mathrm{neq}}}$ of the network as follows to model stress-activated viscous flow,[77]

$$\upsilon_{\mathrm{S}k}(T, T_{\mathrm{f}}) = \upsilon_{\mathrm{S}_k}^{g} \exp\left[-\frac{C_1^g}{\log e}\left(\frac{C_2^g(T - T_{\mathrm{f}}) + T(T_{\mathrm{f}} - T_{\mathrm{g}}^{\mathrm{ref}})}{T(C_2^g + T_{\mathrm{f}} - T_{\mathrm{g}}^{\mathrm{ref}})}\right)\right] \frac{Q_{\mathrm{s}}s}{Ts_y}\left[\sinh\left(\frac{Q_{\mathrm{s}}s}{Ts_y}\right)\right]^{-1}, \quad (2.24)$$

where $\upsilon_{\mathrm{S}_k}^{g}$ is the viscosity at the glass transition temperature, s_{y} is the activation stress, and Q_S is activation parameter. A characteristic stress relaxation time can be defined for the flow rule in eq. (2.23) as $\tau_{\mathrm{S}_k}^{\mathrm{g}} = \upsilon_{\mathrm{S}_k}/\mu_k^{\mathrm{neq}}$ such that the parameters $\tau_{\mathrm{S}_k}^{\mathrm{g}}$ and μ_k^{neq} can be applied to characterize the stress relaxation spectrum.

To model the post-yield softening phenomena, we further assume that the activation stress decreases with the effective viscous strain rate of the network $\overline{\gamma}^{\mathrm{v}}$,

$$\dot{s}_y = h\left(1 - \frac{s_y}{s_{\mathrm{yss}}}\right)\dot{\overline{\gamma}}^{\mathrm{v}}, \quad s_y(0) = s_{\mathrm{y0}} \quad (2.25)$$

where s_{yss} is steady state yield strength and h is a softening modulus. The flow rule in eq. (2.23) for each process can be rewritten in terms of the viscous strain rate by defining a flow stress $s_k = \sqrt{1/2\mathbf{s}_{\mathrm{k}}^{\mathrm{neq}} : \mathbf{s}_{\mathrm{k}}^{\mathrm{neq}}}$ and flow direction, $\mathbf{n}_k = \sqrt{2}\mathbf{s}_k^{\mathrm{neq}}/s_k$,

$$-\frac{1}{2}\mathcal{L}_v \mathbf{b}_k^e \mathbf{b}_k^{\mathrm{e\text{-}1}} = \dot{\gamma}_k^{\mathrm{v}}\mathbf{n}_k, \quad \dot{\gamma}_k^{\mathrm{v}} = \frac{s_k}{\sqrt{2}\upsilon_{S_k}\left(T, T_f, s\right)}, \quad (2.26)$$

Then, an effective viscous strain rate can be defined as,

$$\dot{\bar{\gamma}}^{\mathrm{v}} = \frac{T s_y}{\sqrt{2}\bar{\upsilon}^{\mathrm{g}}_{\mathrm{S}} Q_{\mathrm{s}}} \exp\left[-\frac{C_1^g}{\log e}\left(\frac{C_2^g(T-T_{\mathrm{f}}) + T(T_{\mathrm{f}} - T_{\mathrm{g}}^{\mathrm{ref}})}{T(C_2^g + T_{\mathrm{f}} - T_{\mathrm{g}}^{\mathrm{ref}})}\right)\right]\left[\sinh\left(\frac{Q_{\mathrm{s}} s}{T s_y}\right)\right] \tag{2.27}$$

where $\bar{\upsilon}^{\mathrm{g}}_{\mathrm{S}} > 0$ signifies a characteristic effect shear viscosity at T_{g}. Substituting eq. (2.27) into eq. (2.25) gives the following evolution equation for s_y,

$$\dot{s}_y = (1-\frac{s_y}{s_{\mathrm{yss}}})\frac{T s_y}{\sqrt{2}\tau_{\mathrm{y}} Q_{\mathrm{s}}} \exp\left[-\frac{C_1^g}{\log e}\left(\frac{C_2^g(T-T_{\mathrm{f}}) + T(T_{\mathrm{f}} - T_{\mathrm{g}}^{\mathrm{ref}})}{T(C_2^g + T_{\mathrm{f}} - T_{\mathrm{g}}^{\mathrm{ref}})}\right)\right]\left[\sinh\left(\frac{Q_{\mathrm{s}} s}{T s_y}\right)\right], s_y(0) = s_{\mathrm{y0}} \tag{2.28}$$

where $\tau_{\mathrm{y}} = \bar{\upsilon}^{\mathrm{g}}_{\mathrm{S}}/h$ is a characteristic time constant describing the rate of softening. The constitutive relations of the thermoviscoelastic model are summarized in Table 2.1.

2.3.1 Nonequilibrium Thermodynamic Framework

The constitutive relations for the stress and thermal deformation response have been developed based on considerations of energy and entropy, but the formulation thus far lacks a continuum thermodynamic framework. A thermodynamic theory is needed to determine the thermodynamic requirements of the constitutive relations and to develop a coupled thermomechanical theory for thermally activated shape recovery with heat conduction. The development of nonequilibrium thermodynamic theories for material systems driven far from equilibrium remains an open area of research with many unresolved issues. Recent developments for glassy material systems include Nieuwenhuizen,[100] Ottinger,[103] Bouchbinder and Langer,[129] Moller et al.[130] and Lion et al.[116] Nieuwenhuizen[100] developed a nonequilibrium theory based on the fictive temperature concept of Tool.[122] The theory considered

Table 2.1: Thermoviscoelastic model.

Kinematics:

$$\mathbf{F} = J_T^{\frac{1}{3}}\mathbf{F}_{\mathrm{M}}$$

$$\mathbf{F}_{\mathrm{M}} = \mathbf{F}_k^{\mathrm{e}}\mathbf{F}_k^{\mathrm{v}} \text{ for } k = 1...N.$$

Thermal deformation response:

$$J_{\mathrm{T}}\left(T, \delta^{\mathrm{neq}}\right) = \exp\left(\alpha_{\mathrm{g}}\left(T - T_{\mathrm{i}}\right)\right)\exp(\textstyle\sum_k^P \delta_k^{\mathrm{neq}}),$$

$$T_{\mathrm{f}} = \tfrac{1}{\Delta\alpha}\textstyle\sum_k^P \delta_k^{\mathrm{neq}} + T_{\mathrm{i}}$$

$$\dot{\delta}_k^{\mathrm{neq}} = -\tfrac{1}{\tau_{Rk}}\left(\delta_k^{\mathrm{neq}} - \Delta\alpha_k\left(T - T_{\mathrm{i}}\right)\right)$$

$$\tau_{R_k} = \tau_{R_k}^{\mathrm{g}}\exp\left[-\frac{C_1^{\mathrm{g}}}{\log e}\left(\frac{C_2^{\mathrm{g}}(T-T_{\mathrm{f}})+T\left(T_{\mathrm{f}}-T_{\mathrm{g}}^{\mathrm{ref}}\right)}{T\left(C_2^{\mathrm{g}}+T_{\mathrm{f}}-T_{\mathrm{g}}^{\mathrm{ref}}\right)}\right)\right]$$

Stress response:

$$\boldsymbol{\sigma} = \underbrace{\frac{1}{J}\frac{\mu_{\mathrm{N}}}{3}\frac{T_{\mathrm{f}}}{T_0}\frac{\lambda_{\mathrm{L}}}{\overline{\lambda}_{\mathrm{eff}}}\mathcal{L}^{-1}\left(\frac{\overline{\lambda}_{\mathrm{eff}}}{\lambda_{\mathrm{L}}}\right)\left(\overline{\mathbf{b}}_{\mathrm{M}} - \frac{1}{3}\overline{I}_{\mathrm{M}_1}\mathbf{1}\right)}_{\mathbf{s}^{\mathrm{eq}}}$$

$$+\underbrace{\sum_k^N \frac{1}{J}\mu_k^{\mathrm{neq}}\left(\overline{\mathbf{b}}_k^{\mathrm{e}} - \frac{1}{3}\overline{I}_{1k}^{\mathrm{e}}\mathbf{1}\right)}_{\mathbf{s}^{\mathrm{neq}}} + \underbrace{\frac{1}{2J}\kappa\left(J_{\mathrm{M}}^2 - 1\right)}_{p}\mathbf{1}$$

$$-\tfrac{1}{2}\check{\mathrm{c}}_{\mathrm{v}}\mathbf{b}_k^{\mathrm{e}}\mathbf{b}_k^{\mathrm{e}^{-1}} = \tfrac{1}{\eta_{Sk}}\mathbf{s}^{\mathrm{neq}}$$

$$\eta_{Sk} = \eta_{\mathrm{S}_k}^{\mathrm{g}}\tfrac{Q_S}{T}\tfrac{s}{s_y}\exp\left[-\frac{C_1^{\mathrm{g}}}{\log e}\left(\frac{C_2^{\mathrm{g}}(T-T_{\mathrm{f}})+T\left(T_{\mathrm{f}}-T_{\mathrm{g}}^{\mathrm{ref}}\right)}{T\left(C_2^{\mathrm{g}}+T_{\mathrm{f}}-T_{\mathrm{g}}^{\mathrm{ref}}\right)}\right)\right]\left[\sinh\left(\tfrac{Q_S}{T}\tfrac{s}{s_y}\right)\right]^{-1}$$

$$s = \sqrt{\tfrac{1}{2}\mathbf{s}^{\mathrm{neq}} : \mathbf{s}^{\mathrm{neq}}}$$

$$\dot{s}_{\mathrm{y}} = \tfrac{1}{\tau_y}\tfrac{T}{Q_S}\exp\left[\frac{C_1^{\mathrm{g}}}{\log e}\left(\frac{C_2^{\mathrm{g}}(T-T_{\mathrm{f}})+T\left(T_{\mathrm{f}}-T_{\mathrm{g}}^{\mathrm{ref}}\right)}{T\left(C_2^{\mathrm{g}}+T_{\mathrm{f}}-T_{\mathrm{g}}^{\mathrm{ref}}\right)}\right)\right]\sinh\left(\tfrac{Q_S}{T}\tfrac{s}{s_y}\right)\left(1 - \tfrac{s_{\mathrm{y}}}{s_{\mathrm{y}_{ss}}}\right)s_y, \quad s_{\mathrm{y}}\left(t=0\right) = s_{\mathrm{y}_0}$$

the fictive temperature and configurational entropy as thermodynamic conjugate variables that describes the process during rapid cooling in which the polymer structure becomes kinetically trapped in a quasi-equilibrium state characterized by the equilibrium properties at a higher effective temperature. In the following, we extend the thermodynamic theory of Nieuwenhuizen[100] to include the effects of viscoelasticity and multiple stress and structural relaxation processes. The structural relaxation processes are assumed to be weakly coupled to each other and are entirely separate from the viscoelastic relaxation processes. Each is characterized by different relaxation times and are assumed to be in quasi-equilibrium at a different fictive temperatures T_{f_k}. A key assumption of the thermodynamic theory is that response of a glass-forming material to a temperature change can be separated into fast and slow relaxation processes. The time-scales of the fast and slow processes diverge with decreasing temperature, such that below the glass transition temperature, the fast processes continue to equilibrate at T while the slow configurational processes become kinetically trapped in quasi-equilibrium at the fictive temperatures T_{f_k}. Following these assumptions, the entropy η of the glass-forming system can be partitioned into components η^e for the fast processes and η^c_k for the slow configurational processes,

$$\eta = \eta^e + \sum_k^P \eta^c_k. \tag{2.29}$$

We assume that T_{f_k} and η^c_k are thermodynamic conjugates in addition to T and η^{e}. As such, the Helmholtz free energy density is given by,

$$\Psi = e - T\eta^e - \sum_i^P T_{f_k}\eta^c_k, \tag{2.30}$$

where e is the total internal energy. At equilibrium, $T_{f_k} = T$ and eq. (2.30) reverts to the familiar relation $\Psi = e - T\eta$ of equilibrium thermodynamics. The constitutive relations can be developed by considering the Clausius-Planck entropy inequality for a thermomechanical system,

$$T\dot{\eta} - \dot{e} + \mathbf{S} : \frac{1}{2}\dot{\mathbf{C}} \geq 0. \tag{2.31}$$

Substituting eq. (2.30) into eq. (2.31) for the internal energy density yields the following form for the entropy inequality,

$$\mathbf{S} : \frac{1}{2}\dot{\mathbf{C}} - \dot{\Psi} - \dot{T}\eta^e - \sum_{k=1}^{P} \dot{T}_{f_k}\eta_k^c - \sum_{k=1}^{P} \left(T_{f_k} - T\right)\dot{\eta}_k^c \geq 0, \tag{2.32}$$

The last term in eq. (2.32) represent the internal dissipation caused by structural relaxation to an equilibrium configuration. To model the viscoelastic response of amorphous networks to deformation, we assume that the free energy density can be expressed in terms of a mechanical component and purely thermal components,

$$\Psi\left(\mathbf{C}_{\mathrm{M}}, \mathbf{C}_k^{\mathrm{e}}, T, T_f\right) = \frac{T_f}{T_0} W^{\mathrm{eq}}\left(\overline{\mathbf{C}}_{\mathrm{M}}\right) + \sum_{k=1}^{N} W_k^{\mathrm{neq}}\left(\overline{\mathbf{C}}_k^{\mathrm{e}}\right) + U\left(J_{\mathrm{M}}\right) + f\left(T\right) + \sum_{k=1}^{P} g_k\left(T_{f_k}\right). \tag{2.33}$$

Substituting eq. (2.32) into the entropy inequality, evaluating the time-derivatives, and collecting terms yields,

$$\begin{aligned}\left(\mathbf{S} - \left(\frac{T_f}{T_0}\mathrm{Dev}\mathbf{S}^{\mathrm{eq}} + \sum_{k=1}^{N} J^{\mathrm{T}-2/3}\mathbf{F}_k^{\mathrm{v}^{-1}}\mathrm{Dev}\widetilde{\mathbf{S}}_k^{\mathrm{neq}}\mathbf{F}_k^{\mathrm{v}^{-T}} + \frac{\partial U}{\partial J_{\mathrm{M}}}J_{\mathrm{M}}\mathbf{C}^{-1}\right)\right) : \frac{1}{2}\dot{\mathbf{C}} \\ - \left(\eta^e + f'\left(T\right) - \alpha_g\frac{\partial U}{\partial J_{\mathrm{M}}}J_{\mathrm{M}}\right)\dot{T} - \sum_{k=1}^{P}\left(\eta_k^c + \frac{1}{T_0}\phi_k W^{\mathrm{eq}} + g_k'\left(T_f\right) - \Delta\alpha_k\frac{\partial U}{\partial J_{\mathrm{M}}}J_{\mathrm{M}}\right)\dot{T}_{f_k} \\ + \sum_{k=1}^{N}\mathbf{C}_k^{\mathrm{e}}\mathrm{Dev}\widetilde{\mathbf{S}}_k^{\mathrm{neq}} : \mathbf{L}_k^{\mathrm{v}} - \sum_{k=1}^{P}\left(T_{f_k} - T\right)\dot{\eta}_{\mathrm{k}}^{\mathrm{c}} \geq 0,\end{aligned} \tag{2.34}$$

where,

$$\begin{aligned}\mathrm{Dev}\mathbf{S}^{\mathrm{eq}} &= J^{-2/3}2\frac{\partial W^{\mathrm{eq}}}{\partial \overline{\mathbf{C}}_{\mathrm{M}}} : \left(\mathbb{I} - \frac{1}{3}\mathbf{C}\otimes\mathbf{C}^{-1}\right)\\ \mathrm{Dev}\widetilde{\mathbf{S}}_k^{\mathrm{neq}} &= J^{\mathrm{e}-2/3}2\frac{\partial W_k^{\mathrm{neq}}}{\partial \overline{\mathbf{C}}_k^{\mathrm{e}}} : \left(\mathbb{I} - \frac{1}{3}\mathbf{C}_k^{\mathrm{e}}\otimes\mathbf{C}_k^{\mathrm{e}-1}\right).\end{aligned} \tag{2.35}$$

At equilibrium, $\mathbf{L}_k^{\mathrm{v}} = \mathbf{0}$ and $T_{f_k} = T$, which cause the last line in eq. (2.34) to vanish. Requiring that internal rate of dissipation equal zero at equilibrium for an arbitrary deformation and temperature history gives the following expressions for the nominal stress and entropy components,

$$\begin{aligned}\mathbf{S} &= \frac{T_f}{T_0}\mathrm{Dev}\mathbf{S}^{\mathrm{eq}} + \sum_{k=1}^{N} J^{\mathrm{T}-2/3}\mathbf{F}_k^{\mathrm{v}^{-1}}\mathrm{Dev}\widetilde{\mathbf{S}}_k^{\mathrm{neq}}\mathbf{F}_k^{\mathrm{v}^{-T}} + \frac{\partial U}{\partial J_{\mathrm{M}}}J_{\mathrm{M}}\mathbf{C}^{-1},\\ \eta^e &= -f'(T) + \alpha_g\frac{\partial U}{\partial J_{\mathrm{M}}}J_{\mathrm{M}},\\ \eta_k^c &= -\frac{\phi_k}{T_0}W^{\mathrm{eq}}\left(\overline{\mathbf{C}}_{\mathrm{M}}\right) - g_k'\left(T_{f_k}\right) + \Delta\alpha_k\frac{\partial U}{\partial J_{\mathrm{M}}}J_{\mathrm{M}}.\end{aligned} \tag{2.36}$$

Applying the Arruda-Boyce model for $W^{\mathrm{eq}}\left(\overline{\mathbf{C}}_{\mathrm{M}}\right)$, the Neo-Hookean model for $W_k^{\mathrm{neq}}\left(\overline{\mathbf{C}}_k^{\mathrm{e}}\right)$, and the volumetric model, $U(J_M) = \frac{\kappa}{4}\left(J_{\mathrm{M}}^2 - 2\log J_{\mathrm{M}} - 1\right)$, to eq. (2.36) returns the stress relations in Eqs. (2.20)-(2.22). Substituting eq. (2.36) into eq. (2.34) gives the total dissipation from viscoelastic and structural relaxation processes,

$$\sum_{k=1}^{N}\mathbf{C}_k^{\mathrm{e}}\mathrm{Dev}\widetilde{\mathbf{S}}_k^{\mathrm{neq}} : \mathbf{L}_k^{\mathrm{v}} - \sum_{k=1}^{P}\left(T_{f_k} - T\right)\dot{\eta}_k^c \geq 0. \tag{2.37}$$

We require that each contribution satisfy the positive dissipation criteria,

$$\begin{aligned}\mathbf{C}_k^{\mathrm{e}}\mathrm{Dev}\widetilde{\mathbf{S}}_k^{\mathrm{neq}} : \mathbf{L}_k^{\mathrm{v}} &\geq 0,\\ -\left(T_{f_k} - T\right)\dot{\eta}_k^c &\geq 0.\end{aligned} \tag{2.38}$$

For an isotropic material, the viscous dissipation rate in eq. (2.38) can be expressed in the spatial configuration as,[127]

$$J\mathbf{s}_k^{\text{neq}} : -\frac{1}{2}\mathcal{L}_v\mathbf{b}_k^{\text{e}}\mathbf{b}_k^{\text{e}^{-1}} \geq 0. \tag{2.39}$$

This criteria is satisfied by the viscous flow relation in eq. (2.23) given that the viscosity functions are always positive $\upsilon_{S_k} > 0$. To determine the thermodynamic restrictions on the evolution of the fictive temperature, the time-derivative of the configurational entropy is evaluated to give,

$$\begin{aligned}\dot{\eta}_k^c = &\left(-g_k'' - \Delta\alpha_k^2 K\left(J_{\text{M}}\right)\right)\dot{T}_{f_k} - \Delta\alpha_k\alpha_g K\left(J_{\text{M}}\right)\dot{T} - \sum_{l\neq k}^{P}\Delta\alpha_k\Delta\alpha_l K\left(J_{\text{M}}\right)\dot{T}_{f_l} \\ &+ \quad \left(-\frac{\phi_k}{T_0}\text{Dev}\mathbf{S}^{\text{eq}} + \Delta\alpha_k K\left(J_{\text{M}}\right)\mathbf{C}^{-1}\right) : \frac{1}{2}\dot{\mathbf{C}},\end{aligned} \tag{2.40}$$

where $K\left(J_{\text{M}}\right) = \frac{\partial(pJ)}{\partial J_{\text{M}}} = J_{\text{M}}\frac{\partial U}{\partial J_{\text{M}}} + J_{\text{M}}^2\frac{\partial^2 U}{\partial J_{\text{M}}^2}$. Substituting eq. (2.40) into eq. (2.38) and neglecting all terms associated with the effects of stress (i.e., $K\left(J_{\text{M}}\right)$ and $\text{Dev}\mathbf{S}^{\text{eq}}$) gives,

$$g_k''\left(T_{f_k} - T\right)\dot{T}_{f_k} \geq 0. \tag{2.41}$$

This reduced criteria is satisfied by the kinetic equation (2.15) for T_{f_k} for positive $-g_k''$ and structural relaxation times τ_{R_k}.

The governing equation for the temperature field $T\left(\mathbf{X}, t\right)$ can be derived from the balance of energy for a thermomechanical system,

$$\dot{e} = \frac{1}{2}\mathbf{S} : \dot{\mathbf{C}} - \boldsymbol{\nabla}_{\mathbf{X}} \cdot \mathbf{Q} \tag{2.42}$$

The rate of internal energy can be determined by applying eq. (2.30) for the Helmholtz free

energy density and eq. (2.36) for the constitutive relations to eq. (2.33),

$$\dot{e} = \frac{1}{2}\mathbf{S} : \dot{\mathbf{C}} - \sum_{k=1}^{N} \mathbf{C}_k^{\mathrm{e}} \mathrm{Dev}\widetilde{\mathbf{S}}_k^{\mathrm{neq}} : \mathbf{L}_k^{\mathrm{v}} + T\dot{\eta}^{\mathrm{e}} + \sum_{k=1}^{P} T_{f_k}\dot{\eta}_k^{c}. \tag{2.43}$$

Substituting the above into eq. (2.42) for the first law gives,

$$T\dot{\eta}^{\mathrm{e}} + \sum_{k=1}^{P} T_{f_k}\dot{\eta}_k^{c} = \sum_{k=1}^{N} \mathbf{C}_k^{\mathrm{e}} \mathrm{Dev}\widetilde{\mathbf{S}}_k^{\mathrm{neq}} : \mathbf{L}_k^{\mathrm{v}} - \boldsymbol{\nabla}_{\mathbf{X}} \cdot \mathbf{Q}, \tag{2.44}$$

where $\dot{\eta}_k^{c}$ is given in eq. (2.40). The rate of entropy change associated with the fast relaxation processes, $\dot{\eta}^{e}$, can be evaluated to give,

$$\dot{\eta}^{e} = \left(-f''(T) - \alpha_g^2 K(J_{\mathrm{M}})\right)\dot{T} - \sum_{k=1}^{P} \Delta\alpha_k \alpha_g K(J_{\mathrm{M}})\dot{T}_{f_k} + \alpha_g K(J_{\mathrm{M}})\mathbf{C}^{-1} : \frac{1}{2}\dot{\mathbf{C}}. \tag{2.45}$$

Substituting eqs. (2.40) and (2.45) into eq. (2.44) and neglecting the effects of pressure yields,

$$(-f''T)\dot{T} + \sum_{k=1}^{P} \left(-g_k'' T_{f_k}\right)\dot{T}_{f_k} = -\boldsymbol{\nabla}_{\mathbf{X}} \cdot \mathbf{Q} + \sum_{k=1}^{N} \mathbf{C}_k^{\mathrm{e}} \mathrm{Dev}\widetilde{\mathbf{S}}_k^{\mathrm{neq}} : \mathbf{L}_k^{\mathrm{v}}. \tag{2.46}$$

The governing equation for the temperature describes the effects of internal heating from viscous dissipation, external heat conduction with the environment, and internal heat conduction between the material subsystems associated with the fast and slow relaxation processes.

2.3.2 Parameter Determination

Table 2.2 lists the model parameters and their significance. This section describe the methods for determining the parameters of the discrete stress relaxation spectrum and struc-

tural relaxation spectrum, and parameters describing yielding and post-yield softening in the stress response.

2.3.2.1 Stress Relaxation Spectrum

The parameters μ_k^{neq} and $\tau_{S_k}^{\text{g}}$ of the discrete stress relaxation spectrum can be determined from dynamic frequency sweep tests using the method proposed by Haupt et al.[131] The method constructs a substitute fractional damping viscoelastic model to fit the master curve of frequency dependency on the storage modulus. The fractional damping model features a continuous relaxation spectrum characterized by 2 parameters compared to the $2N$ parameters of the discrete model; thus it is significantly more efficient and efficacious to fit the substitute model to experimental data than the discrete model. The parameters of the discrete model are determined by constructing a discrete approximation of the cumulative relaxation spectrum of the continuous fractional damping model.

To establish a correspondence with the substitute model, the thermoviscoelastic model was first linearized for the case of small strains and structural equilibrium, where $T_f = T$.[78] The frequency-dependent storage and loss shear moduli of the linearized discrete model is given by,

$$G'_{\text{disc}}(\omega) = \mu^{\text{eq}} + \sum_k^N \frac{\mu_k^{\text{neq}} \omega^2 \tau_{\text{S}k}^2}{1 + \omega^2 \tau_{\text{S}k}^2}, \quad G''_{\text{disc}}(\omega) = \sum_k^N \frac{\mu_k^{\text{neq}} \omega \tau_{\text{S}k}}{1 + \omega^2 \tau_{\text{S}k}^2} \tag{2.47}$$

where μ^{eq} is the rubbery shear modulus and $\mu^{\text{neq}} = \sum_k^N \mu_k^{\text{neq}}$ is the difference of the glassy and rubbery moduli. The parameters μ^{eq} and μ^{neq} can be calculated from the tensile storage modulus at the rubbery and glassy plateau as $\mu^{\text{eq}} = E_{\text{r}}/(2(1 + \upsilon_{\text{r}}))$, $\mu^{\text{neq}} = E_{\text{g}}/(2(1 +$

υ_g)) assuming the rubbery Poisson's ratio of $\upsilon_r = 0.5$ and glassy Poisson's ratio of $\upsilon_g = 0.35$. The substitute fractional damping model is described in detail in Haupt et al.[131] The frequency-dependent storage and loss moduli for the substitute model can be written as,

$$\begin{aligned} G'_{\text{frac}}(\omega) &= \mu^{eq} + \frac{\mu^{\text{neq}}((\omega\xi)^{2\alpha} + (\omega\xi)^{\alpha}\cos(\alpha\pi/2)}{1 + (\omega\xi)^{2\alpha} + (\omega\xi)^{\alpha}\cos(\alpha\pi/2)}, \\ G''_{\text{frac}}(\omega) &= \frac{\mu^{\text{neq}}((\omega\xi)^{\alpha}\sin(\alpha\pi/2)}{1 + (\omega\xi)^{2\alpha} + (\omega\xi)^{\alpha}\cos(\alpha\pi/2)} \end{aligned} \tag{2.48}$$

where ξ is the characteristic relaxation time and $0 \leq \alpha \leq 1$ is the fractional order denoting the frequency span of the relaxation spectrum. The relaxation frequency spectrum h_{frac} for the substitute model can be evaluated analytically from the complex modulus $G_{\text{frac}}(i\omega) = G'_{\text{frac}}(\omega) + iG''_{\text{frac}}(\omega)$ by taking the inverse Stieltjes transform of $G_{\text{frac}}(i\omega)/i\omega$. The cumulative relaxation spectrum, defined as $H(\nu) = \int_0^{\nu} h(u)du$, of the linearized model and substitute model are given by,

$$\begin{aligned} H_{\text{disc}}(\nu) &= \sum_{k}^{N} \mu_k^{\text{neq}} \langle \nu - \nu_k \rangle^1 \\ H_{\text{frac}}(\nu) &= \frac{\mu_{\text{neq}}}{\alpha\pi}\left[\arctan\left(\frac{(\lambda\xi)^{\alpha} + \cos(\alpha\pi)}{\sin(\alpha\pi)}\right) - \pi\left(\frac{1}{2} - \alpha\right)\right], \end{aligned} \tag{2.49}$$

where $\langle\rangle^1$ denotes a step function. To determine the parameters of $H_{\text{disc}}(\nu)$ we defined a power-law distribution of the relaxation frequencies of the relaxation frequencies at T_0,

$$\nu_k^0 = \nu_{\min}^0 \left(\frac{\nu_{\max}^0}{\nu_{\min}^0}\right)^{\frac{k-1}{N-1}}. \tag{2.50}$$

These can be shifted to the reference glass transition temperature using the WLF equations to obtain the characteristic stress relaxation times,

$$\tau_{Sk}^g = \frac{1}{\nu_k^0}\exp\left(\frac{-C_1^g}{\log e}\frac{(T_0 - T_g^{\text{ref}})}{C_2^g + T_0 - T_g^{\text{ref}}}\right). \tag{2.51}$$

The parameters μ_k^{neq} can be determined for the frequency distribution in Eq. (2.50) by constructing a staircase approximation of H_{frac} as follows,

$$\begin{aligned}
\mu_1^{\text{neq}} &= \frac{1}{2}(H(\nu_1^0) + H(\nu_2^0), \\
\mu_k^{\text{neq}} &= \frac{1}{2}(H(\nu_{k+1}^0) - H(\nu_{k-1}^0), 1 < k < N-1, \\
\mu_N^{\text{neq}} &= \mu^{\text{neq}} - \sum_k^{N-1} \mu_k^{\text{neq}}.
\end{aligned} \tag{2.52}$$

The frequency range, $\nu_{\text{min}}^0 \geq \nu_k^0 \geq \nu_{\text{max}}^0$, and number of relaxation processes N can be chosen within the guidelines provided by Haupt et al.[131] to provide a smooth reconstruction of the master curve of the storage modulus.

2.3.2.2 Structural Relaxation Spectrum

We developed a similar method to determine the parameters of the discrete structural relaxation spectrum in the time domain. The method constructs a substitute Kohlrausch-Williams-Watts (KWW) model[132,133] for the reduced structural relaxation function $\rho(u)$ and fit the parameters of the substitute model to the master curve for the dependence of the relaxation function on the reduced time u,

$$\rho_{\text{KWW}}(u) = \exp\left(-\left(\frac{u}{\chi}\right)^{\beta}\right), \tag{2.53}$$

where χ represents the characteristic structural relaxation time and $0 < \beta \leq 1$ denotes the time span of the relaxation function. The relaxation spectrum can be evaluated by taking the inverse Laplace transform of $\rho_{\text{KWW}}(u)$ and can be expressed as infinite series,[134]

$$h_{\text{KWW}}(\tau) = -\frac{\chi}{\pi\tau^2}\sum_{k=0}^{\infty}\frac{(-1)^k}{k!}\sin(\pi\beta k)\,\Gamma(\beta k+1)\left(\frac{\tau}{\chi}\right)^{\beta k+1}, \tag{2.54}$$

where $\Gamma()$ is the gamma function. By comparison, the discrete spectrum is given by,

$$h_{\text{disc}}(\tau) = \sum_{k}^{P} \Delta\alpha_k \langle \tau - \tau_k \rangle^0, \tag{2.55}$$

where $\langle\rangle^0$ denotes the Dirac Delta function. To determine the parameters of the discrete spectrum, we defined a power law distribution of relaxation time at $T_{\text{g}}^{\text{ref}}$ as,

$$\tau_{\text{R}_k}^{g} = \tau_{\min} \left(\frac{\tau_{\max}}{\tau_{\min}} \right)^{\frac{k-1}{P-1}} \tag{2.56}$$

The parameters $\Delta\alpha_k$ of the discrete spectrum can be determine by approximating cumulative structural relaxation spectrum $H(\tau) = \int_0^\tau h(t)\,\mathrm{d}\,t$ as,

$$\begin{aligned}
\Delta\alpha_1 &= \frac{\Delta\alpha}{2} \left(H_{\text{KWW}}(\tau_1) + H_{\text{KWW}}(\tau_2) \right), \\
\Delta\alpha_k &= \frac{\Delta\alpha}{2} \left(H_{\text{KWW}}(\tau_{k+1}) - H_{\text{KWW}}(\tau_{k-1}) \right), \; 1 < k < P-1, \\
\Delta\alpha_P &= \Delta\alpha - \sum_{k}^{P-1} \Delta\alpha_k.
\end{aligned} \tag{2.57}$$

The range of relaxation times, $\tau_{\min} \leq \tau_{\text{S}_k}^{g} \leq \tau_{\max}$, and number of relaxation processes, P, are selected to provide a smooth reconstruction of the master curve of the relaxation function.

2.3.2.3 Viscous Flow Parameters

The parameter Q_{s}/s_{y0} in the flow equations (2.24)-(2.28) describes the dependance of yield strength on temperature and strain rate, while $s_{y_{ss}}/s_{y_0}$ is the ratio of the steady-state and initial yield stress, and τ_y describes the characteristic time scale of post-yield stress softening. The parameters can be determined from uniaxial compression tests. At the yield

point, the equivalent viscous strain rate and yield strength were estimated as $\dot{\bar{\gamma}}^{\mathrm{v}} = \dot{\bar{\gamma}}$ and $s_y = s_{\mathrm{y0}}$. Assuming significant viscous flow occurs at the yield stress (i.e., $Q_{\mathrm{s}}s/(Ts_{\mathrm{y0}}) > 1$), a relationship between the effective strain rate and yield stress of the network can be approximated from eq. (2.27) as,

$$\dot{\bar{\gamma}} = \frac{Ts_{\mathrm{y0}}}{\sqrt{2}\bar{\eta}_S Q_{\mathrm{s}}} \exp\left[-\frac{C_1^g}{\log e}\left(\frac{T - T_g^{\mathrm{ref}}}{T}\right)\right] \exp\left[\left(\frac{Q_{\mathrm{s}}s}{Ts_{\mathrm{y0}}}\right)\right], \tag{2.58}$$

where $T_f \approx T_{\mathrm{g}}^{\mathrm{ref}}$ for temperatures well below the glass transition temperature. Taking the logarithm of both sides gives the following linear relationship between the log strain rate and flow stress of the network,

$$T \ln\left(\dot{\bar{\gamma}}\right) = C + \frac{Q_{\mathrm{s}}}{s_{\mathrm{y0}}}s, \tag{2.59}$$

where C is a temperature dependent constant. The deviatoric flow stress and flow strain rate can be calculated from the yield stress and strain rate of the uniaxial compression tests as, $s = \sigma/\sqrt{3}$ and $\dot{\bar{\gamma}} = \sqrt{3}\dot{\epsilon}$. Equation (2.59) provides an initial estimate for $Q_{\mathrm{s}}/s_{\mathrm{y0}}$, which can be applied in numerical simulations of isothermal uniaxial compression to iterate for $Q_{\mathrm{s}}/s_{\mathrm{y0}}$, $s_{y_{ss}}/s_{y_0}$, and τ_y.

2.4 Results and Discussion

2.4.1 Thermomechanical Response

Table 2.2 lists the model parameters determined for tBA-co-XLS networks prepared with 10 wt%, 20 wt%, and 40 wt% crosslinking agents. Figure 2.1 shows the dynamic fre-

Table 2.2: Parameters of the generalized thermoviscoelastic constitutive model for amorphous SMPs.

Parameter	**10wt**	**20wt**	**40wt**	**Physical significance**
$T_g^{ref}(^oC)$	36	38	40	glass transition temperature for $q_{cool} = 1^oC/min$.
$\alpha_r(10^{-4}/^o\,C)$	6.9	6.3	6.0	rubbery coefficient of volumetric thermal expansion.
$\alpha_g(10^{-4}/^o\,C)$	2.34	2.4	2.70	glassy coefficient of volumetric thermal expansion.
$\xi(10^{-6}s)$	1.0	2.0	3.0	stress relaxation time at $T = T^{ref}$.
α	0.7	0.7	0.62	stress relaxation spectrum breadth
$\chi(s)$	900	600	200	structural relaxation time at $T = T_g^{ref}$.
β	0.38	0.38	0.35	structural relaxation spectrum breadth
C_1	13.76	13.63	16.21	first WLF constant.
C_2 (^{o}C)	32.46	33.75	49.50	second WLF constant.
μ_N (MPa)	0.533	1.166	3.43	shear modulus of equilibrium polymer network.
λ_L	4	4	4	limiting chain stretch of equilibrium network.
κ (MPa)	1667	1667	1667	bulk modulus.
μ^{neq} (MPa)	555.6	555.6	555.6	non-equilibrium shear modulus of glassy material.
$Q_S/s_{y_0}(^oK/MPa)$	110	127	135	activation parameter for viscous flow.
$s_{y_{ss}}/s_{y_0}$	0.49	0.53	0.57	ratio of initial to steady-state yield strength.
τ_y	3200	3200	2000	characteristic yield time

quency sweep test results at different temperatures. The measurements at each temperature were shifted along the frequency axis to construct the master curve for the storage modulus at $T_0 = 75°\text{C}$. The parameters of the fractional damping model, α and ξ, were fit to the master curve according to the method described in Sec. 2.3.2.1, and applied to determine the parameters, μ_k^{neq}, of the discrete relaxation spectrum using eq. (2.52) for a power-law distribution of relaxation frequencies $1 \leq \nu_k^0 \leq 10^9$ (eq. (2.50)) for $N = 20$ processes. This range in ν_k^0 corresponds to $4.8 \times 10^{-3} \leq \tau_{\text{S}_k}^{\text{g}} \leq 4.8 \times 10^6$.

The parameters of discrete spectrum were used in eq. (2.47) to reproduce the frequency response at the reference temperature. The model accurately reproduced the experimental measurements until high frequencies, $\omega a_T > 10^5$, which corresponded with the onset of the glassy plateau. At higher frequencies, the model provided a larger storage modulus than found experimentally. This may be caused by the inability of the time-temperature superposition principal to describe the approach to the glassy state.

Figure 2.2(a) plots the structural relaxation function measured in isothermal recovery tests at four different temperatures as a function of time from the beginning of the temperature drop. The recovery rate varied noticeably with temperature. At the highest temperature, the specimens nearly reached equilibrium within the 60 min hold time, while little relaxation was observed at the lowest temperature. The master curve of structural relaxation was obtained by plotting the response function against reduced time, as shown in Fig. 2.2(b). The KWW substitute model was used to fit master curve to determine the parameters β and χ. The thermal contraction measured at higher temperatures exhibited

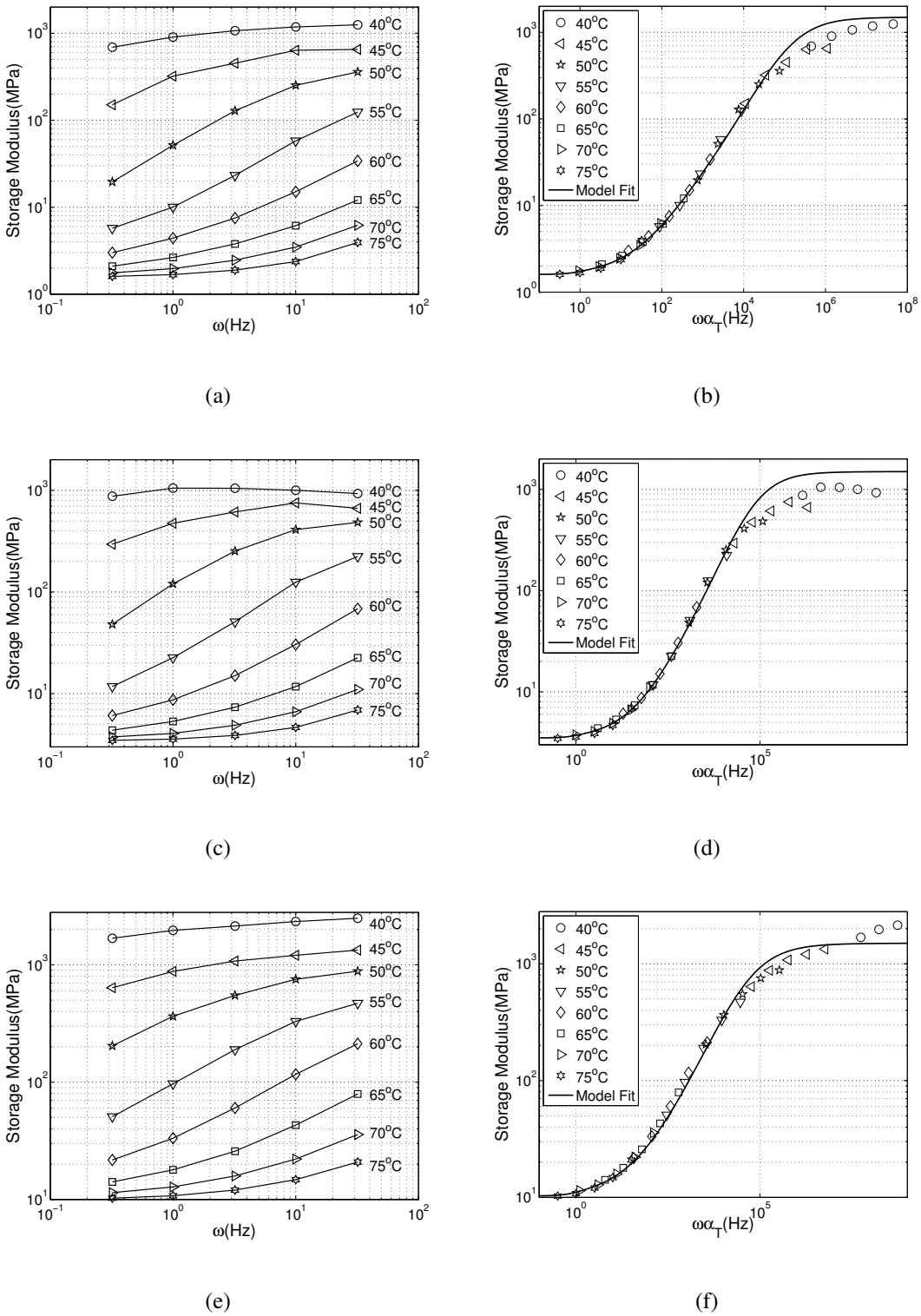

Figure 2.1: TTS tests for different cross-linker densities (a) 10 wt% (b) 10wt% master curve (c) 20wt% (d) 20wt% master curve (e) 40wt% (f) 40wt% master curve.

noticeable overshoot. This was caused by an overshoot of the target temperature at the end of temperature ramp during fast cooling. The parameters $\Delta\alpha_k$ of the discrete structural relaxation spectrum was determined for a power-law distribution of relaxation times in the range $10^{-5}\chi \leq \tau^{g}_{R_k} \leq 200\chi$ using eq. (2.57) for $P = 20$ processes. The parameters of the discrete spectrum were applied to simulate the unconstrained constant cooling rate tests. The results shown in Fig. 2.3 demonstrated significantly improved agreement between experiment and simulations compared to the method presented in Nguyen et al.[78] that fit the parameters of the structural relaxation spectrum directly to constant cooling rate tests. The prior method assumed that the structural relaxation spectrum had the same shape as the viscoelastic spectrum, leading to a large discrepancy in the prediction of the thermal contraction in the glass transition region.

A key assumption of the model is that the stress and structural relaxation times share the same temperature and structure dependance. This allowed the master curve for the structural relaxation function to be constructed using the WLF constants, determined from the shift factor measured for the stress relaxation function, to calculate the temperature-dependent and structure-dependent shift factor for the normalized volume recovery curves. The results in Fig. 2.2 and 2.3 validated this assumption for the three tBA-co-XLS networks. Few studies have examined the relationship between the stress and structural relaxation times. Espinoza and Aklonis[135] compared the two behaviors in aging experiments. The model by Tool[122] and a modified WLF model for the temperature and structure dependence of the relaxation times were used to fit experimental data for volume recovery and

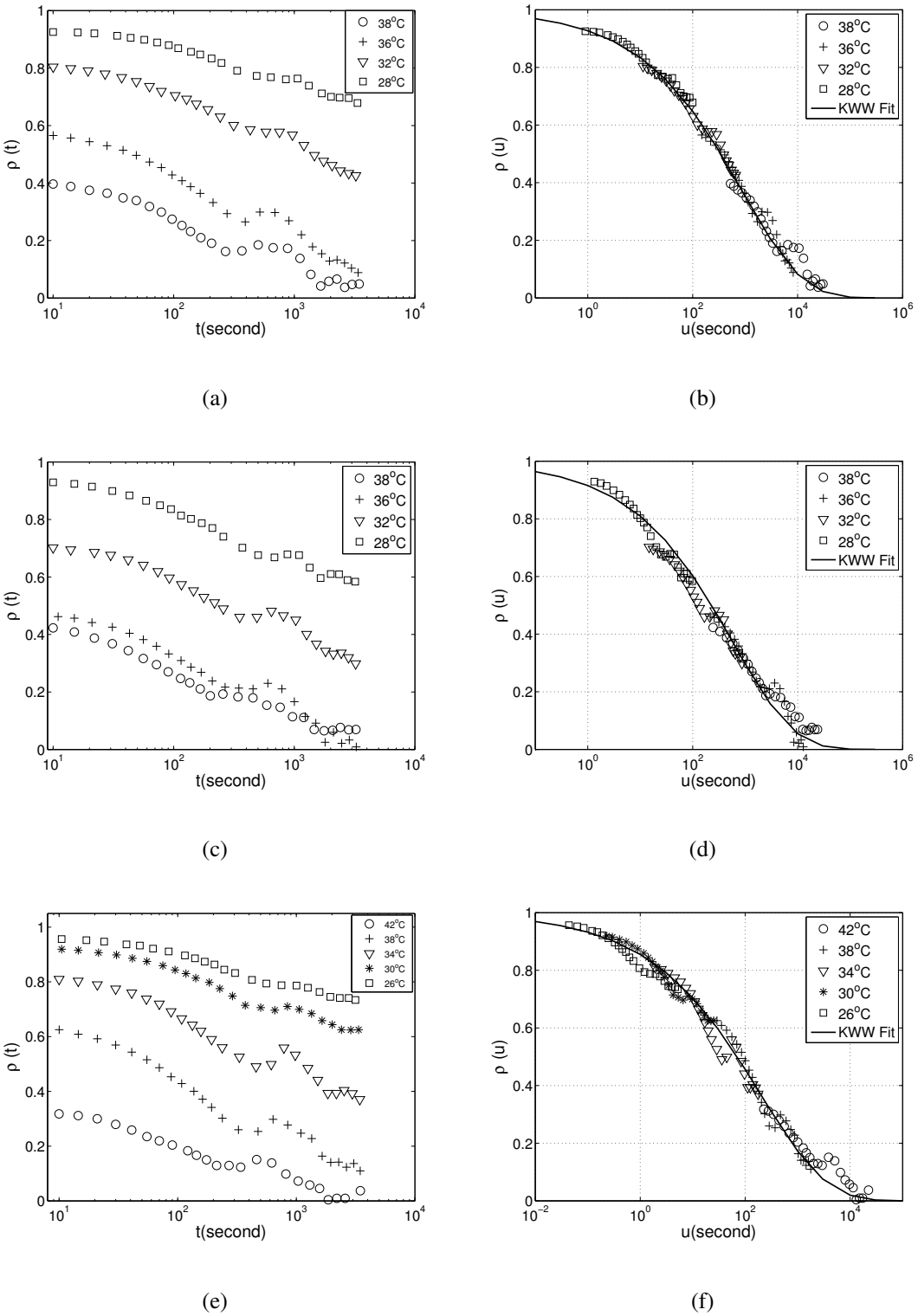

Figure 2.2: Isothermal recovery tests (a) 10 wt% (b) 10wt% master curve (c) 20wt% (d) 20wt% master curve (e) 40wt% (f) 40wt% master curve.

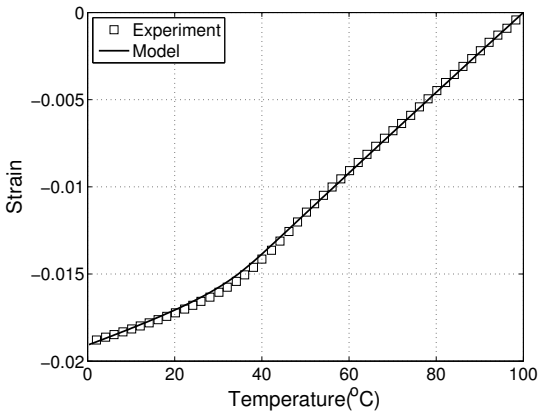

Figure 2.3: Thermal strain: experimental and simulation results for 10wt % SMPs

stress relaxation of polystyrene. It was found that both models were able to reproduced the volume recovery data, but only the modified WLF model was able to reproduce the stress relaxation data for different aging times. The modified WLF equation used by Espinoza and Aklonis[135] shares similar characteristics with the Adam-Gibbs equation, which corroborates our findings.

To determine the viscoplastic parameters, isothermal uniaxial compression experiments were performed at different strain rates at temperatures well below $T_{\mathrm{g}}^{\mathrm{ref}}$. Fig. 2.4(a) plots the stress-strain curves for 10°C, and Fig. 2.4(b) shows the Eyring plots for all three networks (eq. (2.59)). The parameters for the yield and post-yield behavior were determined by fitting to the stress-strain curves measured at 10°C for strain rates 0.003/s, 0.01/s, and 0.03/s (Fig. 2.4(c)). The results were used to predict the stress response for the strain rate 0.03/s at different temperatures (Fig. 2.4(d)). The results of 20 wt% and 40 wt% materials are shown in Fig. 2.5. The results showed that the model was able to reproduce the transi-

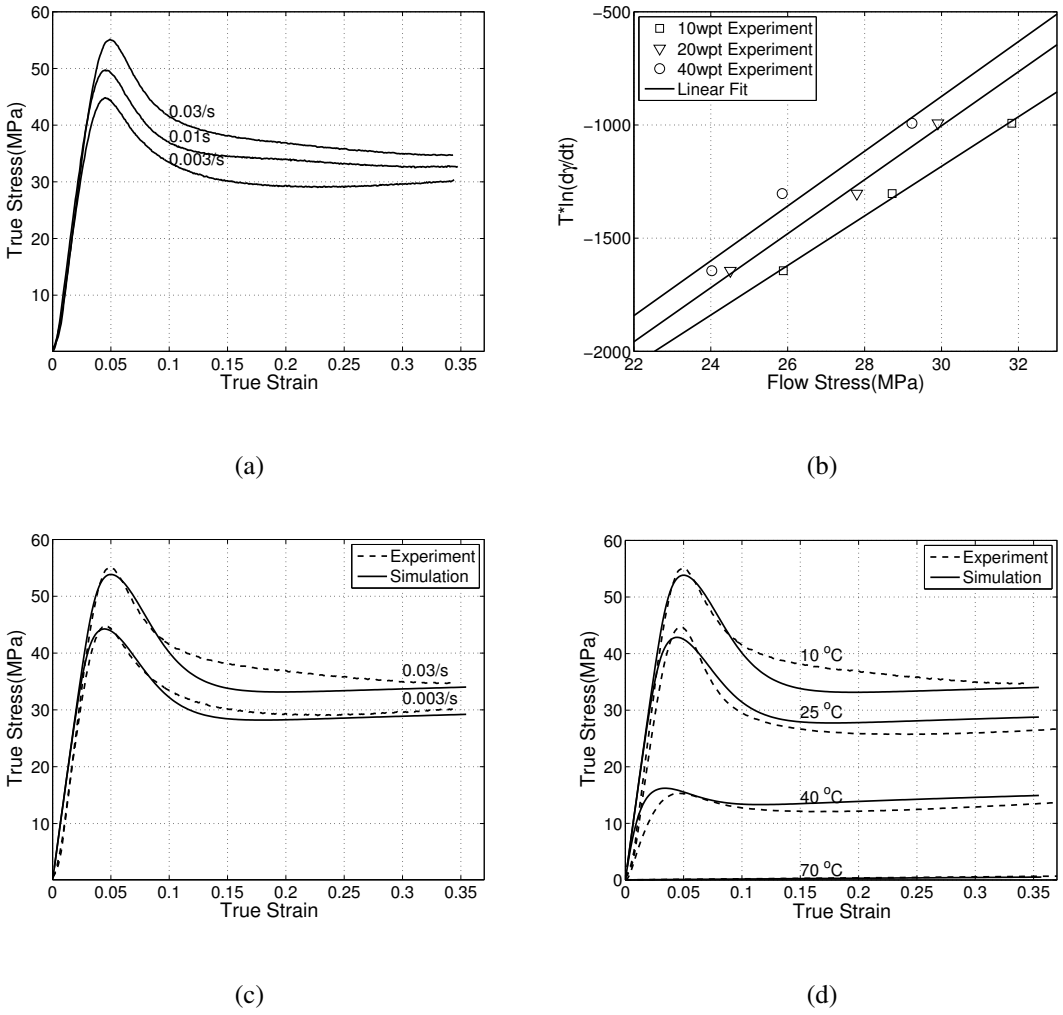

Figure 2.4: Uniaxial compression tests for 10wt% materials (a) 10°C experimental results (b) Eyring plot (c) experimental and simulation results for 10°C (d)experimental and simulation results for strain rate 0.03/s

tion from a viscoplastic response, with a distinct yield point and post-yield softening, to a viscoelastic response with increasing temperatures through the glass transition region. The model also captured the strain rate and temperature dependance of the yield strength across the glass transition region. Compared to the single-process model of Nguyen et al.,[45] which calculated a stiffer elastic response and smaller yield strains in the glass transition region, the multiple relaxation model more accurately described the temperature-dependence of the yield behavior.

2.4.2 Partially Constrained Recovery Response

The thermoviscoelastic model was implemented numerically into Mathematica and applied to simulate the partially constrained and fully constrained shape recovery response. The numerical implementation evaluated the constitutive relations for uniaxial tension at a material point and did not consider the effects of heat conduction. Simulations of the partially constrained recovery response applied the same temperature and loading history used in the experiments (Sec. 2.2.3). To model the shape-memory programming step, the sample was either started at 70°C for hot-deformation or cooled to 20°C at 5°C/min for cold deformation and held for 20 min. For both cases, a 30% compressive engineering strain was applied at 10^{-3}/s and held for 20 min to allow for stress relaxation. The temperature was decreased to 0°C at 5°C/min and held for 10 min in two steps. In the first step, the strain was held constant during cooling to allow for stress relaxation by viscoelasticity and thermal contraction of the vitrifying material. Once the stress decreased to zero, the

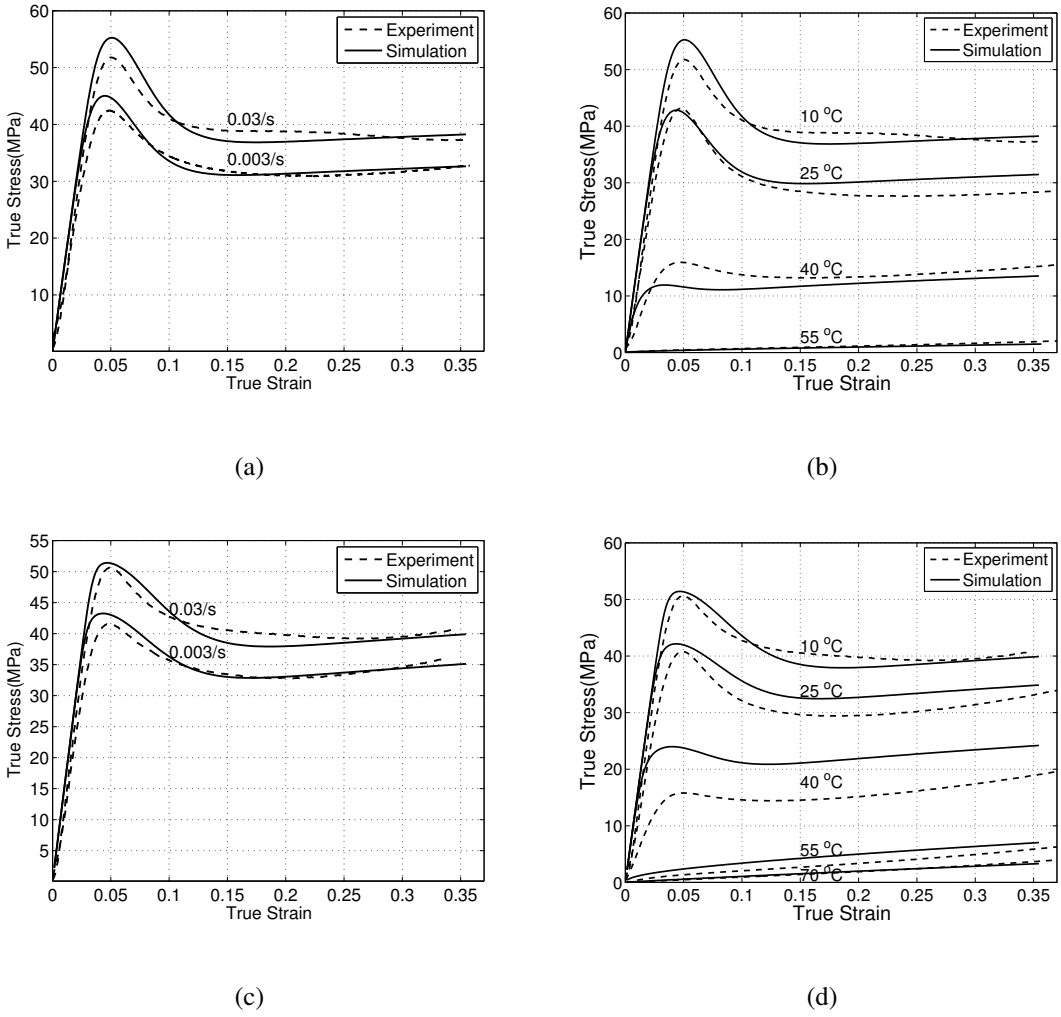

Figure 2.5: Uniaxial compression tests (a) 20wt % experimental and simulation results for 10°C (b) 20% experimental and simulation results for strain rate 0.03/s (c) 40wt % experimental and simulation results for 10°C and (d) 40wt %experimental and simulation results for strain rate 0.03/s .

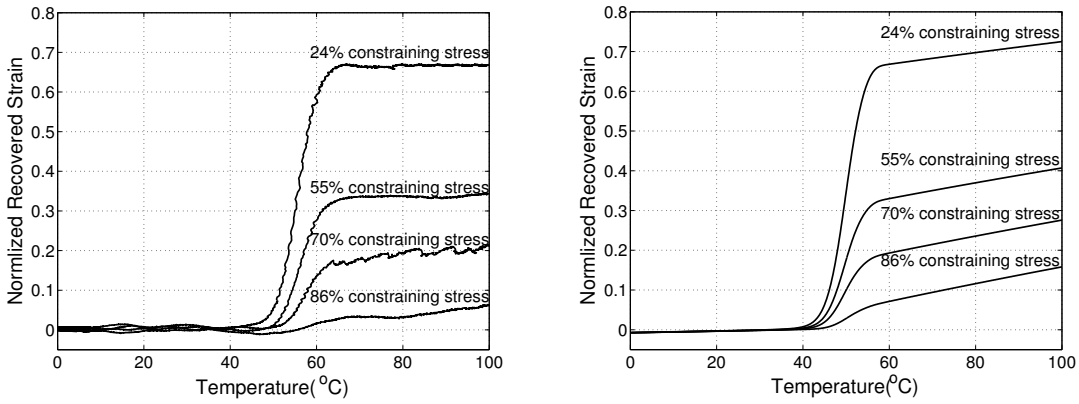

Figure 2.6: The normalized recovered strain at different constraining stress for 10wt% materials programmed at 70 °C comparing (a) experiment and (b) simulations

second step allowed the strain to decrease freely during the remainder of the cooling period and the annealing period to simulate the sample contracting away from the compression platens during experiments. To simulate the shape-recovery step, an engineering stress, which corresponded to a fraction of the stress required to deform the material at 70°C to 30% engineering strain, was applied for both the hot-deformation and cold-deformation case in 60 seconds. The temperature was increased to 100°C at 2°C/min while the constraining stress was held constant.

Figures 2.6, 2.7 and 2.8 show the normalized recovered strain for the 10 wt%, 20 wt% and 40 wt% materials programmed at 70°C for various constraining stress comparing experiments and simulations. Results for the 40wt % materials are presented in Appendix **??**. For all three networks, activation of significant strain recovery occurred at temperatures slightly higher than the T_g measured by constant cooling rate tests. Previous works showed

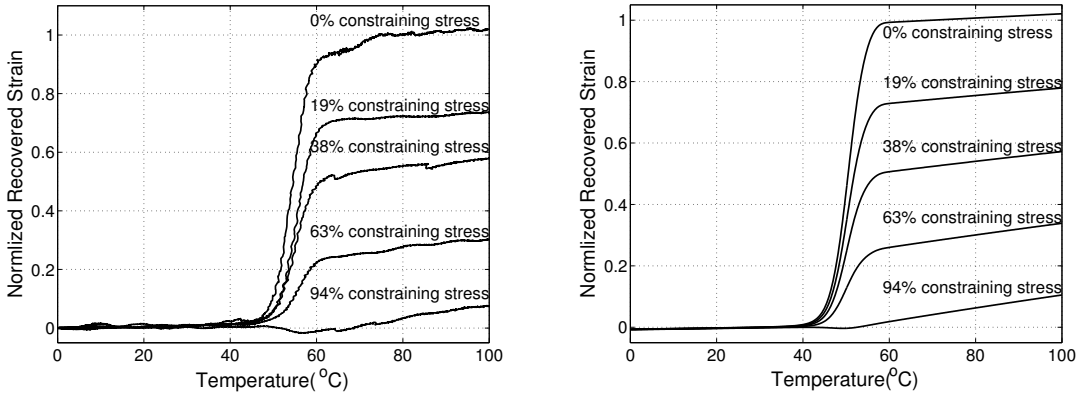

(a) (b)

Figure 2.7: The normalized recovered strain at different constraining stress for 20wt% materials programmed at 70 °C comparing (a) experiment and (b) simulations

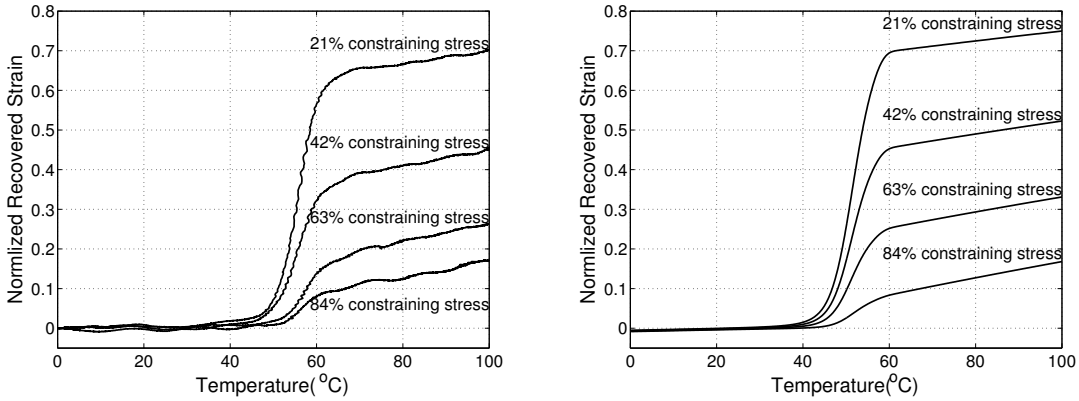

(a) (b)

Figure 2.8: The normalized recovered strain at different constraining stress for 20wt% materials programmed at 70 °C comparing (a) experiment and (b) simulations

that this temperature corresponded to the onset glass transition temperature measured in dynamic thermal scan experiments at fixed frequency.[78] The strain recovered monotonically from the programmed strain to an equilibrium value determined by constraining stress and the equilibrium modulus. The simulations predicted an activation temperature and correspondingly an end temperature that was on average lower by 5.5 °C. The slower activation of strain recovery observed in experiments was most likely caused by finite rate of heat conduction, which was not considered in the simulations. Both simulations and experiments showed that the recovery rate decreased with increasing constraining stress. The strain continued to increase after full recovery because of thermal expansion and the slope of the post-recovery strain-temperature curve for the 0% constraining stress corresponded to the rubbery CTE in the simulation. The CTE appeared to increase with the constraining stress in both experiments and simulations, but this was caused by the entropic stiffening of the material with temperature, which under a constant constraining stress provided additional elastic strain recovery.

The partially constrained recovery response of materials programmed below T_g differed significantly from those programmed above T_g. Figures 2.9, 2.10 and 2.11 show that the activation of strain recovery occurred at lower temperatures (20°C) below T_g and more gradually with a slower recovery rate. Though the simulations also predicted a lower activation temperature, the values was 10°C higher than measured in experiments. The simulations also did not predict a slower initial recovery rate. These discrepancies suggest that the large compressive stresses generated by the initial cold compression had a non-negligible

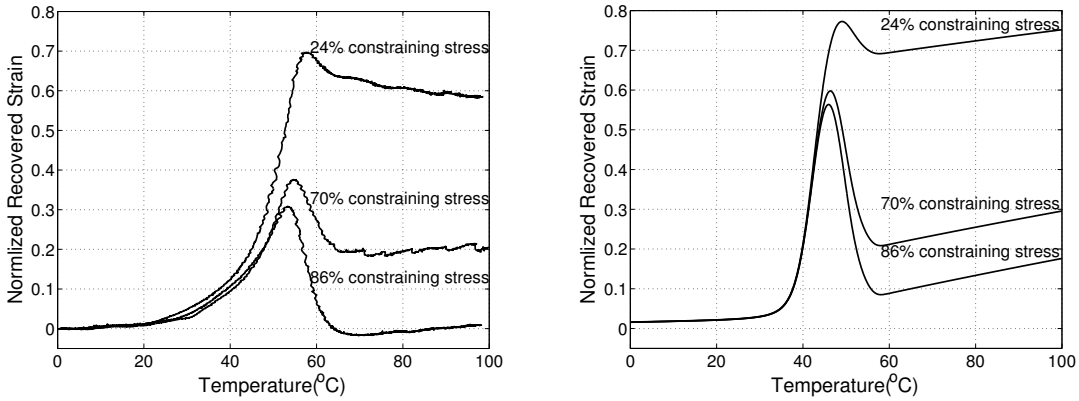

Figure 2.9: The normalized recovered strain at different constraining stress for 10wt% materials programmed at 20 °C comparing (a) experiment and (b) simulations

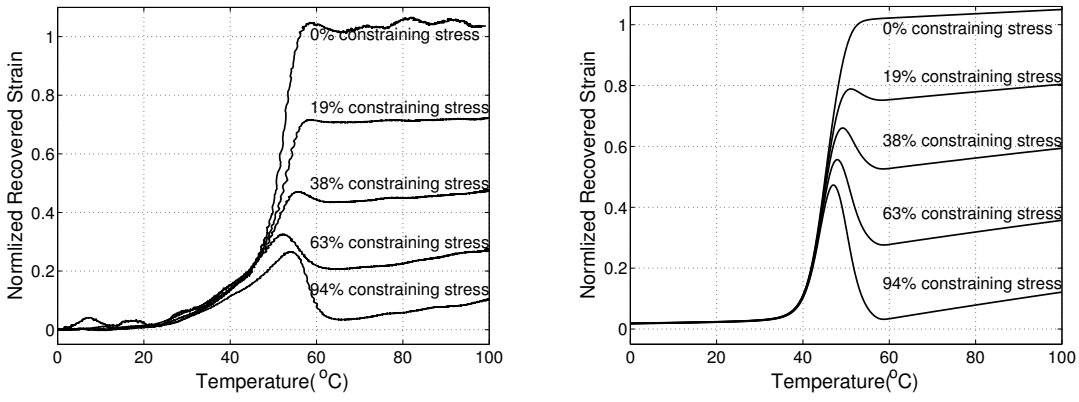

Figure 2.10: The normalized recovered strain at different constraining stress for 20wt% materials programmed at 20 °C comparing (a) experiment and (b) simulations

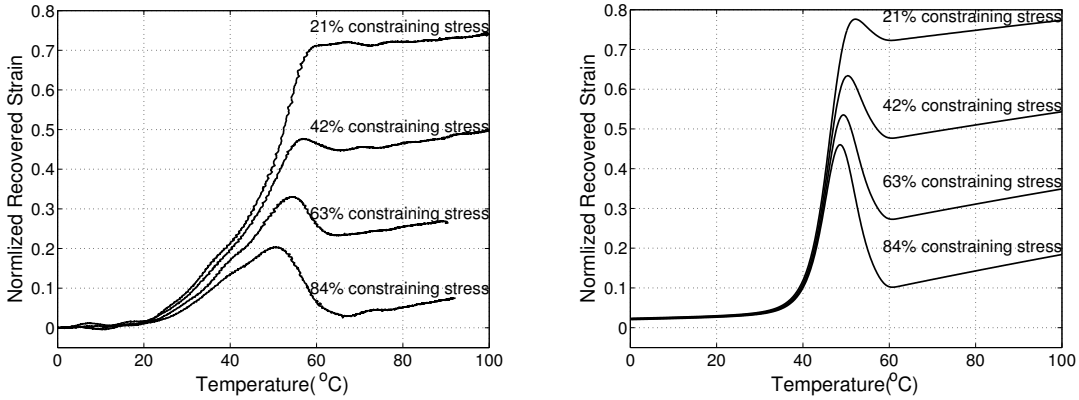

Figure 2.11: The normalized recovered strain at different constraining stress for 40wt% materials programmed at 20 °C comparing (a) experiment and (b) simulations

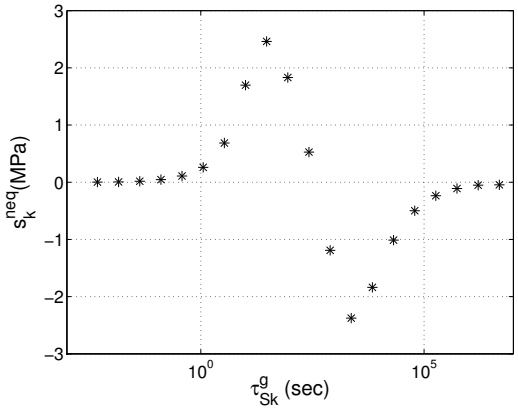

Figure 2.12: The distribution of nonequilibrium stress at the beginning of recovery process for 10 wt% materials programmed at 20 °C

effect on the structural relaxation. Pressure in general increases the structural relaxation time, and a larger structural relaxation time causes a more gradual activation of strain recovery.[117] After activation, the strain recovered non-monotonically with temperature, first increasing to a maximum value then decreasing to the equilibrium value determined by the constraining stress and rubbery modulus. Both the experiments and simulations showed that the strain overshoot increased with increasing constraining stress; though the model generally predicted a lager strain overshoot than measured in experiments.

In preliminary studies, we did not observe the overshoot in recovered strain in identical simulations using the single-process model of Nguyen et al.[45] (results not shown). This indicates that the phenomena is caused by the distribution of the stress relaxation times and is akin to the Kovacs effect which arises from the distribution of structural relaxation times.[120] The stress relaxation spectrum of the tBA-co-XLS networks spans a broad distribution of relaxation times. This caused a broad distribution of nonequilibrium stresses, $\mathbf{s}_k^{\text{neq}}$, to develop during the relaxation period of the programming step. Processes with larger relaxation times remained in compression with negative flow stresses throughout the 20 minute relaxation period, while those with smaller relaxation times were driven into tension (Fig. 2.12). The application of the small constraining stress prior to deployment did not change significantly the distribution of nonequilibrium stresses. The viscous strain rates scale with the nonequilibrium stresses. As a result, the faster processes with positive nonequilibrium stresses first cause the strain to increase during heating until the slower processes with negative nonequilibrium stresses become dominant and cause the strain to

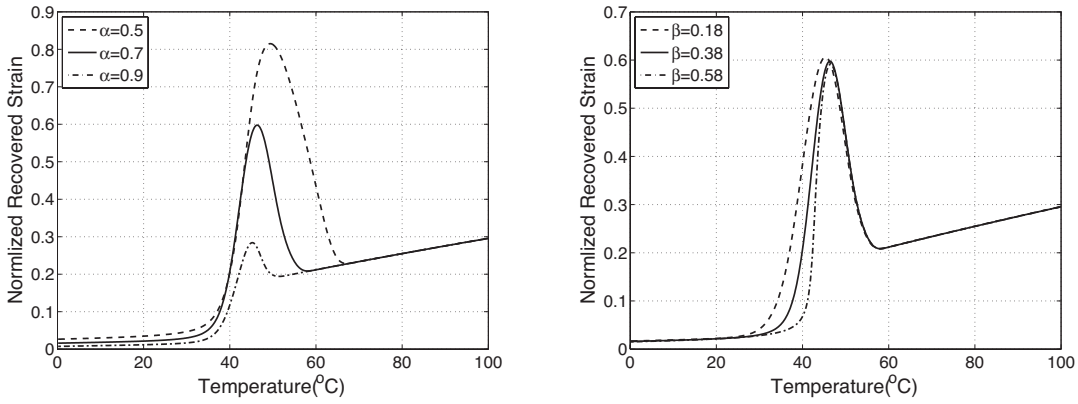

(a) (b)

Figure 2.13: Parameter study for partial recovery behavior (a) viscoelastic spectrum breadth (b) structural relaxation spectrum breadth

decrease to the equilibrium value.

To investigate the importance of the different time-dependent deformation mechanisms on the partially constrained recovery response of materials programmed in the glassy state, the simulations were repeated for the 10 wt % material with 70% constraining stress varying one-by-one the parameters of the model. The overshoot in the recovered strain was most sensitive to α, which describes the breadth of the relaxation spectrum (Fig. 2.13(a)). The strain overshoot decreased dramatically with larger α, vanishing in the limit $\alpha \rightarrow 1$. This limit corresponds to a single exponential process. Structural relaxation primarily influenced the activation of strain recovery. A broader distribution of structural relaxation times, represented by a smaller β in Fig. 2.13(b), produced a lower activation temperature and slower initial recovery rate. The overshoot in the recovered strain was strongly influenced also by the parameters governing the stress-activated yield and softening response.

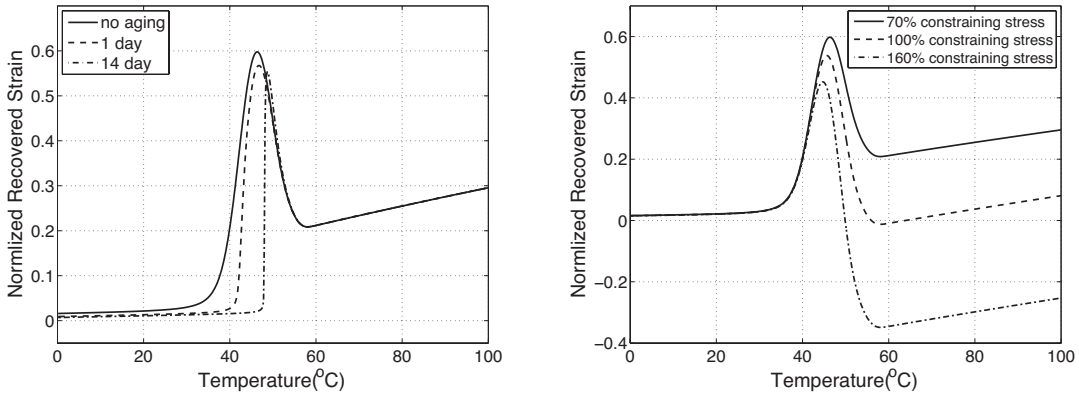

(a) (b)

Figure 2.14: Loading condition study for partial recovery behavior (a) aging (b) constraining stress

A larger activation parameter, Q_S/s_{y_0}, and a smaller relative steady-state yield strength, $s_{y_{ss}}/s_{y_0}$, led to a lower yield point and a smaller stress for the applied deformation to drive the recovery response.

The study also examined the effects of an extended annealing (aging) time and constraining stress. The model predicted that extended annealing at 20°C resulted in a higher activation temperature and also a greatly improved initial recovery rate as shown in Fig 2.14(a). The overshoot in the recovered strain was also observed when the constraining stress was larger than the stress for 30% compressive strain above T_g (Fig 2.14(b)).

2.4.3 Fixed-Strain Recovery

To simulate the fixed-strain recovery response, the sample was either started at 70°C for hot-deformation or cooled to 20°C at 5°C/min for cold deformation and held for 10

minutes. For both cases, a 30% compressive engineering strain was applied at 10^{-2}/s and held for 5 minutes to allow for stress relaxation before cooling to 0°C at 5°C/min and annealed 10 minutes. The strain was allowed to vary as described for the partially constrained simulations (Sec. 2.4.2) to allow the stress to fully unload. The temperature was increased to 100°C at 2°C/min while holding the strain constant. Fig. 2.15 plots the stress response for the 10% wt material as a function of temperature during the heating step, showing a stress overshoot at temperatures near the T_g. A significantly larger maximum stress was obtained for materials programmed by cold compression than by hot compression. This result is consistent with previous experimental observations[49,53,54,56] regarding the effects of deformation temperature on the recovery response. The stress overshoot for materials programmed above T_g is caused by the constrained thermal expansion of the stiff unrelaxed material.[117] Thermal strains are small, on the order of 1%, and this leads to relatively small activation stresses. For those programmed in the unrelaxed state below T_g, the stress overshoot is caused by viscoelastic recovery of the programmed strain, which for these simulations was 30%. Consequently, the cold-programmed material has the capacity for significantly larger activation stresses prior to the glass transition, where the material softens and the stresses decrease back to the equilibrium value. The simulation was repeated for different applied compressive strains ranging from 5% to 30% and different material parameters. Fig. 2.16(a) showed that the maximum stress increased significantly with the applied strain, while Fig. 2.16(b) shows that a higher yield strength can generate a higher activation stress.

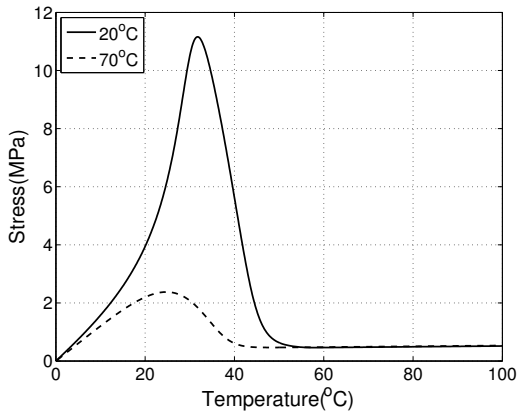

Figure 2.15: Simulation results for fully constrained recovery for 10 wt %SMPs programmed above and below T_g^{ref}

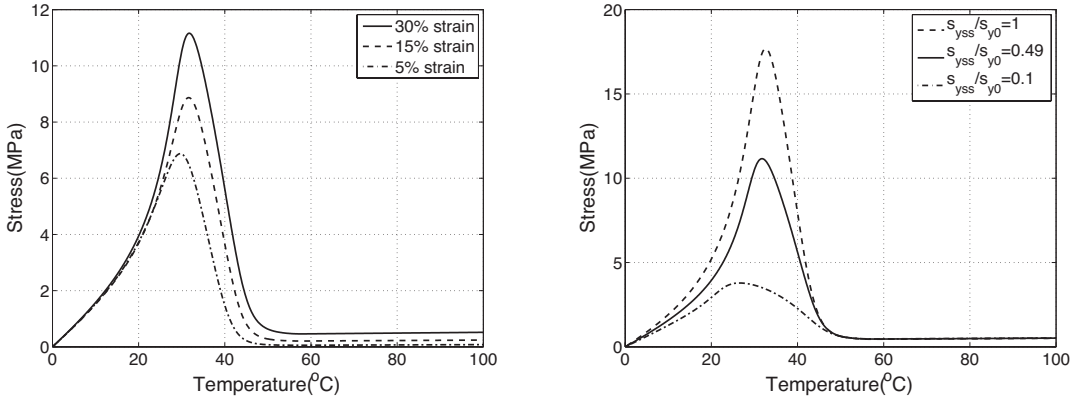

(a) (b)

Figure 2.16: Simulation results for fully constrained recovery for 10 wt %SMPs programmed at 20 ^oC (a) different compression strain influence (b)steady state yield strength influence

2.5 Conclusions

A thermomechanical constitutive theory was developed for the glass transition of amorphous networks, and applied to study the effects of deformation temperature and physical aging on shape memory performance. The model described multiple coupled nonlinear viscoelastic processes and nonlinear structural relaxation processes. The constitutive model was applied to investigate the partially constrained and fixed-strain recovery response of materials programmed above and below the glass transition temperature. Comparing the experimental and modeling results for the hot-deformed and cold-deformed materials yields the following observations:

- We were able to use the temperature shift factor measured for the stress relaxation function to calculate the temperature-dependent and structure-dependent shift factor for the structural relaxation function. This validated the central assumption of the model that the stress relaxation times and structural relaxation times exhibit the same temperature and structure dependance.

- The temperature-dependent and rate-dependent yield strength and post-yield softening was successfully described using a multiple-process Eyring model for stress-activated flow. The model was characterized by a single activation stress and the distribution of relaxation times measured from the small-strain viscoelastic response at high temperatures. Moreover, the same temperature and structure dependence applied for the structural relaxation time was used to describe the resistance to viscous

flow and the rate of dynamic softening. Compared to the single-process model of Nguyen et al.,[45] the multiple-process model more closely reproduced the temperature-dependence and strain-rate dependence of the isothermal stress response through the glass transition.

- The model was able to reproduce the partially constrained recovery response of materials programmed above and below T_g. For materials programmed above T_g, the model accurately captured the recovery rate and recovery strain ratio as a function of the constraining stress. For materials programmed below T_g, the model reproduced the overshoot in recovered strain.

- The magnitude of the strain overshoot was most sensitive to the viscoelastic parameter α, which described the breadth of the relaxation spectrum. The maximum strain decreased with increasing α and vanished entirely as $\alpha \rightarrow 1$, which corresponds to a single exponential relaxation process. These results indicate the overshoot in the recovered strain stems from the distributed nature of relaxation process. The magnitude of the strain overshoot was also significantly influenced by the yield strength.

- The activation temperature and initial recovery rate was most sensitive to the structural relaxation parameter β, which described the width of the structural relaxation spectrum. A narrow structural relaxation spectrum produced a higher activation temperature and faster initial recovery rate. The influence of the structural relaxation mechanisms also caused the increase in the activation temperature and recovery rate

with the annealing time below T_g.

- The fixed-strain recovery response of materials programmed below T_g exhibited a significantly larger stress overshoot than those programmed above T_g. This was consistent with experimental observation.[49,53,56] The stress overshoot is caused by constrained thermal expansion of the unrelaxed glassy material for hot-programmed materials,[117] and by viscoelastic strain recovery for cold-programmed materials.

Despite their numerous advantages, SMPs have not been widely adopted, primarily because of their slow recovery times, which typically range between 100 and 1000 s,[4,21] and small actuation force.[113,117] This study shows the recovery rate, activation temperature, and activation stress can be manipulated to a large extent by designing the time, temperature, and deformation history of the programming step. Cold-deformation programming can be applied to achieve an overshoot in the recovered strain under a constraining stress, which introduces the possibility of designing more complex shape changes. In addition, cold-deformation can also increase significantly the actuation force capacity. Physical aging can dramatically increase the initial recovery rate and increase the activation temperature for unconstrained and partially constrained recovery.

The present constitutive model was developed considering only the time-dependent mechanisms of the glass transition of amorphous networks. The successful application of the model for type I SMPs reinforces the fact that these materials are a subset of a well-studied class of conventional engineering polymers, yet SMPs are distinguished from conventional polymers in their application. Specifically, deformation programming, stor-

age, and deployment for SMP devices can occur in a narrow temperature range surrounding the glass transition. This is particularly true for many proposed SMP biomedical devices, where the activation temperature (T_g onset) is tailored to be near 40° (body temperature) and device storage is intended to be at 20°C (room temperature). Physical aging becomes an important factor in the performance of these SMP devices. The application of SMP devices involves the interaction of many nonlinear and time-dependent mechanisms. By modeling these underlying mechanisms of shape-memory behavior, we have identified programming strategies for improving the recovery rate and actuation stress that could potentially help overcome some persistent challenges in the design of SMP devices.

Chapter 3

Modeling the Solvent-induced Shape-memory Behavior

This chapter has been reprinted from R. Xiao and T. Nguyen, "Modeling the solvent-induced shape-memory behavior of glassy polymers ", Soft Matter, Vol. 9, Pages 9455-9464, 2013, with permission from The Royal Society of Chemistry[136] .

In this chapter, a constitutive model was presented for the effect of solvent absorption on the thermomechanical properties and shape-memory behavior of amorphous polymers. The absorption of low concentrations of solvent depresses the glass transition temperature by increasing the molecular mobility of the polymer chains. In a shape-memory application, this can lead to premature shape recovery and significant alterations to the time-dependence and temperature-dependence of shape recovery. We implemented the constitutive model for finite element analysis and developed a computational model that considered the time-

dependent effect of diffusion to study the solvent-induced shape-memory behavior of a meth(acrylate) copolymer network. The model was validated by comparing to isothermal shape recovery experiments of specimens in air and water at different temperatures.

3.1 Introduction

Thermally activated shape-memory polymers (SMP) have garnered significant attention in recent years for their potential broad range of applications and tailorable properties.[5] Several different mechanisms can be employed to achieve the shape memory effect in polymers,[2,137,138] but the two most common ones are the melt transition of semicrystalline polymers and the glass transition of amorphous polymers. For amorphous polymers, the temporary shape is obtained by deforming the material in its heated rubbery state. Cooling the material below the glass transition temperature T_g reduces the molecular mobility of the polymer chains, fixing the deformed shape in a nonequilibrium thermodynamic state. The temporary shape should be fixed indefinitely until the material is heated above the T_g. However, amorphous SMPs can experience a significant loss in shape fixity below T_g when stored for a prolonged period of time in water or in a humid environment.[14] While the absorption of solvents, such as water, can be detrimental to the shape-memory effect of amorphous networks, the phenomena can also be harnessed to athermally activate shape recovery. This alternative to temperature-driven shape recovery is attractive for biomedical applications, such as implantable medical devices, where the controlled delivery of heat

poses an intractable challenge in a surgical environment.

The first experimental studies of solvent-driven shape recovery examined the effect of water absorption on polyurethane SMP.[14,83] The authors observed that the T_g decreased gradually with the absorption of water, resulting in a reduction in the Young's modulus and yield strength, as well as a loss of the programmed shape. For large programmed tensile deformation, this phenomena can lead to buckling instabilities, as demonstrated by Zhao et al.[139] and Wang et al.[140] for PMMA in ethanol. Huang[141] also demonstrated the potential biomedical applications of solvent-driven shape recovery. Chen et al.[15] reported a novel shape memory polyurethane containing pyridine moieties with excellent moisture absorption properties and measured how the temperature and humidity influenced the shape recovery performance. They found that a faster recovery rate could be achieved with higher temperature and higher levels of humidity. Lu et al.[84] described the solvent-driven shape recovery behavior of a styrene-based SMP immersed in toluene, while Lu et al.[16] investigated the response of a poly(vinyl alcohol) SMP in good versus poor solvents. Simith et al.[142,143] studied the relationship between the glass transition temperature, water absorption, and uniaxial tensile stress response for a family of (meth)acrylate networks. Their experimental results showed an initial rapid decrease in the elastic modulus upon immersion in water. The toughness also initially increased, then abruptly decreased after a prolonged immersion time.

CHAPTER 3. MODELING THE SOLVENT-INDUCED SHAPE-MEMORY BEHAVIOR

The absorption of solvent precipitates shape recovery in amorphous polymers by depressing the glass transition temperature below the storage temperature. This also causes the material to become more compliant (i.e., more rubbery) compared to the dry polymer at the same temperature. The effect of low solvent concentration on the glass transition of amorphous networks has been modeled as an increase in the molecular mobility caused either by an increase in free volume[86,87,144] or configurational entropy of the polymer-solvent system. The pioneering configurational entropy theory of Dimarzio and Gibbs[88] used statistical mechanics to derive an implicit expression for the glass transition temperature of a polymer-solvent system as a function of the concentration, and size and flexibility of the solvent molecules. Chow[89] extended the work of Dimarzio and Gibbs[88] by deriving an explicit expression for T_{g} that showed good agreement with experimental data. Here, we adopt the configurational entropy approach to develop a constitutive model for the effect of low solvent concentration on the thermomechanical properties and shape-memory performance of amorphous polymers. Previously, we developed thermoviscoelastic constitutive models for the glass transition behavior of amorphous polymers, that included the time-dependent mechanisms of stress relaxation, structural relaxation, and stress-activated yielding and viscous flow below T_{g}.[45,78,145] The models were applied successfully to describe the effects of temperature, mechanical loading,[145,146] and physical aging[79] on the shape-memory response. The thermoviscoelastic models used the nonlinear Adam-Gibbs model[39,42,121] to describe the temperature-dependence and structure-dependence of the relaxation time. In the Adam-Gibbs model the relaxation time depends inversely on the

configurational entropy of the polymer network. Cooling the polymer below the T_g progressively reduces the configurational entropy and causes the relaxation time to increase exponentially preventing the material from relaxing to equilibrium.

In this work, we extend the thermoviscoelastic model of Xiao et al.[145] by modifying the nonlinear Adam-Gibbs model to incorporate the effect of low solvent concentrations on the temperature-dependent relaxation behavior of amorphous polymers. We implemented the model for finite element analysis and developed a computational model to study solvent-driven shape recovery of a (meth)acrylate network. The computational model also described the diffusion of solvent into the polymer matrix to more accurately describe the time-dependence of shape recovery. The model parameters were obtained from dynamic mechanical analysis and diffusion experiments. The model was validated by comparing to isothermal free recovery experiments of specimens in air and water at different temperatures.

3.2 Methods

3.2.1 Materials and Specimen Preparation

Methyl acrylate (MA), methyl methacrylate (MMA), poly(ethylene glycol) dimethacrylate (PEGDMA), with typical molecular weight $M_n = 550$, and photoinitiator 2,2-dimethoxy-

2-phenylacetophenone (DMPA) were purchased from Sigma Aldrich and used in their as-received condition. The MA-MMA-PEGDMA solution was mixed in a 5:4:1 mass ratio, and DMPA was added to the comonomer solution at a concentration of 0.5 wt% of the total comonomer weight. The polymer solution was either injected between two glass slides to make tensile test specimens or a thin-walled tube mold to make hollow cylindrical specimens as described in Yakacki et al.[21] The specimens were placed in a UV oven (Model CL-1000L Ultraviolet Crosslinker) for 15 minutes to polymerize. The specimens were then annealed in an incubator at 80^oC for 1 hour to achieve full polymerization.

3.2.2 Experiments

In previous works, we performed three sets of experiments to characterize the thermomechanical properties of amorphous polymers in their dry state. These were time-temperature superposition tests to measure the temperature-dependent viscoelastic properties, isothermal volume recovery tests to measure the structural relaxation properties, and isothermal uniaxial compression tests to measure the temperature-dependent and rate-dependent yield and post-yield behavior. The methods for these tests were described in detail in Nguyen et al.,[45,78] Choi et al.,[79] Xiao et al.[145] Here we describe additional experiments developed to measure the effect of water absorption on the mechanical properties and shape recovery behavior of the polymer network.

3.2.2.1 Diffusion Tests:

Rectangular specimens with dimension $20.0 \times 20.0 \times 0.95$ mm^3 were used to measure the diffusion coefficient of water into the polymer network. Each specimen was weighed before testing. The specimens were then immersed in de-ionized water and placed in an incubator at either 25°C or 30°C. The specimens were removed periodically and weighed using a high resolution digital balance with 10^{-4} gram resolution. The specimens were returned immediately to the water bath and placed into the incubator after measurement. The measurements were performed on 4 specimens for each temperature.

3.2.2.2 Frequency Sweep Tests:

The frequency sweep tests were performed on dry and saturated tension film specimens using a TA Q800 Dynamic Mechanical Analyzer (DMA) in multifrequency mode. Dry polymer film specimens were heated from 20 °C to 80 °C in 5°C increments. The specimens were annealed at each test temperature for 5 minutes to allow for complete heat conduction through the sample, then subjected to a 0.2% dynamic strain at 0.3 Hz, 1.0 Hz, 3.0 Hz, 10.0 Hz, and 30.0 Hz to measure the storage modulus and tan delta. The same frequency sweep was also performed on saturated samples at room temperature to measure the effect of solvent absorption on the storage modulus and tan delta. Saturated specimens were prepared by immersing the dry tension film specimens in de-ionized water and placed in an incubator at 25°C for 48 hours. This immersion time was sufficient to achieve equilibrium in prior diffusion tests described in Sec. 3.2.2.1. The saturated specimens were not

subjected to measurements at higher temperatures to prevent significant evaporation.

3.2.2.3 Isothermal Uniaxial Tension Tests:

Isothermal uniaxial tension tests were performed on dry and saturated specimens using a custom-built micro-tensile setup described in Joshi et al.[147] to measure the effect of water absorption on the tensile properties. The experiments used dog-bone shape specimens with a $6.0 \times 2.0 \times 1.0$ mm^3 gage section cut from the film specimen using a digital control mill (Figure 3.1). Digital image correlation (DIC) was used to measure the local strain in the gage section as described in Joshi et al.[147] The specimens were pulled to 40% engineering strain at a strain rate of $0.002/s$.

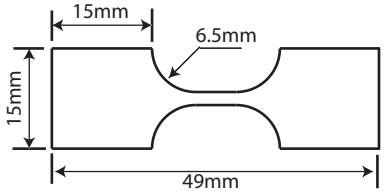

Figure 3.1: Dog-bone shaped tensile test specimen.

3.2.2.4 Isothermal Recovery Tests:

Isothermal shape recovery experiments were performed to compare the response of dry specimens in air and specimens immersed in water. The experiments used two different specimen geometries: thin film specimens $20.0 \times 5.0 \times 0.75$ mm^3 in size, and tube specimens with length 15.0 mm, outer radius 10.0 mm, and thickness 0.8 mm. The film

specimens were equilibrated at 60°C and then stretched to 25 % engineering strain in 100 seconds using the TA Q800 DMA. The deformed specimens were cooled down to 20°C at 5°C/min and annealed for five minutes before unloading to nominally zero force (0.001 N). For recovery in air, the film specimens were heated in the DMA, set to zero force mode, to the test temperature at 10°C/min then held constant for 1 hour. The displacements of the grips were measured under nominally zero force (0.001 N) and used to calculate the shape fixity ratio defined as,

$$R_t = \frac{L_t - L_0}{L_{max} - L_0}, \tag{3.1}$$

where L_0, L_t, and L_{max} are the initial length, current length at time t, and the maximum length at the end of the programmed step. The shape recovery experiments in air were performed at four test temperatures: 41°C, 44°C, 47°C and 50°C. For recovery in water, the specimens were immersed in de-ionized water and placed in an incubator at the test temperature. The two test temperatures were 25°C and 30°C. The momentary shape was recorded using a digital camera and the length L_t was measured using the GNU Image Manipulation Program [1].

Similarly, the tube specimens were equilibrated at 60°C in an incubator. The top and bottom of the tube were pinched together using tweezers to create a temporary shape (Fig. 3.2). The deformed specimen was removed from the oven to room temperature to fix the programmed shape. To recover the permanent tube shape, the programmed specimen was

[1] http://www.gimp.org/

immersed in de-ionized water at either 25°C or 30°C. The specimen was imaged using a digital camera during the recovery process to track the distance between the top and bottom of pinched section (Fig. 3.2). The shape fixity ratio was defined as,

$$R_t = \frac{H_t - H_0}{H_{min} - H_0}, \tag{3.2}$$

where H_0, H_t, and H_{min} are the initial height, current height at time t, and the height at the end of the programmed step between the top and bottom of the pinched section (Fig. 3.2).

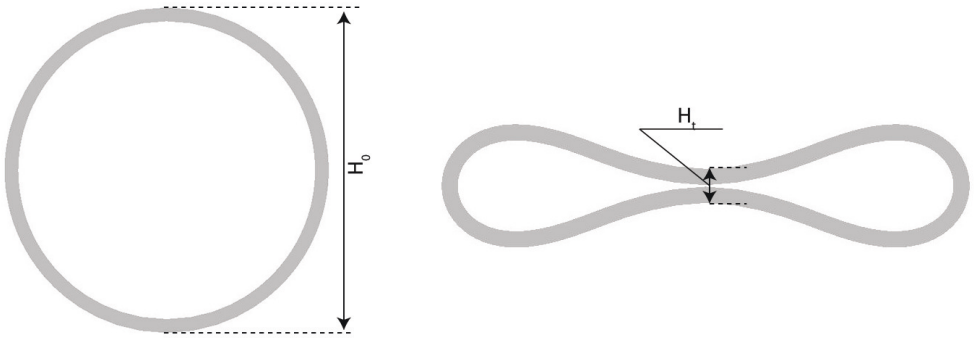

Figure 3.2: The geometry of the tube specimens for both undeformed and deformed shape

3.2.3 Constitutive Model

We present in this section an extension of a constitutive model developed by Xiao et al.[145] to incorporate the effect of solvent absorption on the thermomechanical behavior of amorphous polymers spanning the glass transition. We first review the key features of the nonlinear thermoviscoelastic model described previously in detail in Nguyen et al.[45,78] and

Xiao et al.,[145] then focus on developing a formulation for the dependence of the stress and structural relaxation times on the solvent concentration.

To model the swelling, time-dependent thermal, and mechanical deformation, we assume that the deformation gradient, which maps material lines in the reference configuration to spatial lines in the deformed configuration, can be decomposed multiplicatively into isotropic swelling and thermal components, $\mathbf{F}_{\mathrm{S}} = J_{\mathrm{S}}^{1/3}\mathbf{1}$ and $\mathbf{F}_{\mathrm{T}} = J_{\mathrm{T}}^{1/3}\mathbf{1}$, and a mechanical component, $\mathbf{F}_{\mathrm{M}}$. The mechanical component is decomposed further into N_1 parallel elastic and viscous components:

$$\mathbf{F} = (J_{\mathrm{S}}J_{\mathrm{T}})^{\frac{1}{3}}\mathbf{F}_{\mathrm{M}}, \quad \mathbf{F}_{\mathrm{M}} = \mathbf{F}_k^{\mathrm{e}}\mathbf{F}_k^{\mathrm{v}}, \quad \text{for} \quad k = 1...N_1. \tag{3.3}$$

We assume molecular incompressibility, such that the diffusion of solvent molecules into the polymer network causes the following volume change,

$$J_s = 1 + \frac{\rho_p}{\rho_s}\phi, \tag{3.4}$$

where ρ_p, ρ_s is the density of the polymer and solvent and ϕ is the mass ratio between solvent and polymer; thus $\frac{\rho_p}{\rho_s}\phi$ is the volumetric ratio between the solvent and polymer.

Thermal deformation is assumed to undergo structural relaxation with an instantaneous deformation given by the glassy coefficient of thermal expansion (CTE), α_g, and N_2 time-dependent partial deformations δ_k^{neq},

$$J_{\mathrm{T}}\left(T, \delta^{\mathrm{neq}}\right) = \exp\left(\alpha_{\mathrm{g}}\left(T - T_{\mathrm{i}}\right)\right) \exp\left(\sum_k^{N_2} \delta_k^{\mathrm{neq}}\right), \tag{3.5}$$

where T_i is the initial temperature at time $t = 0$. The total departure from the instantaneous response is given by $\delta^{\text{neq}} = \sum_k^{N_2} \delta_k^{\text{neq}}$. We assume that δ^{neq} is related to the fictive temperature T_f of the nonequilibrium structure as, $T_\text{f} = \frac{1}{\Delta\alpha}\delta^{\text{neq}} + T_\text{i}$, where $\Delta\alpha = \alpha_r - \alpha_g$ is the difference between rubbery and glassy CTE. The fictive temperature was originally proposed by Tool[122] to represent the temperature at which the nonequilibrium structure would be in equilibrium. We assume the following first-order nonlinear kinetic relation originally proposed by Kovacs et al.[120] for the partial deformations,

$$\frac{d\delta_k^{\text{neq}}}{dt} = -\frac{1}{\tau_{R_k}}\left(\delta_k^{\text{neq}} - \Delta\alpha_k\left(T - T_\text{i}\right)\right), \tag{3.6}$$

where τ_{R_k} is the structural relaxation time dependent on the temperature, fictive temperature, and solvent concentration. The parameter $\Delta\alpha_k$ is the partial CTE with $\sum_k^{N_2} \Delta\alpha_k = \Delta\alpha$.

Polymers exhibit different time-dependent response to volumetric and isochoric (volume preserving) deformation.[27] Consequently, the mechanical deformation gradient and its elastic component are split into volumetric and isochoric components, $\overline{\mathbf{F}}_\text{M} = J_\text{M}^{-1/3}\mathbf{F}_\text{M}$ and $\overline{\mathbf{F}}_k^\text{e} = J_k^{\text{e}-1/3}\mathbf{F}_k^\text{e}$. This allows the stress response to be represented by an equilibrium distortional part $\mathbf{s}^{\text{eq}}$ represented by the Arruda-Boyce[126] model, N_1 nonequilibrium distortional parts $\mathbf{s}_k^{\text{neq}}$ represented by the Neo-Hookean model, and a time-independent volumetric part p,

$$\sigma = \underbrace{\frac{1}{J}\frac{\mu_\text{N}}{3}\frac{T_\text{f}}{T_0}\frac{\lambda_\text{L}}{\overline{\lambda}_\text{eff}}\mathcal{L}^{-1}\left(\frac{\overline{\lambda}_\text{eff}}{\lambda_\text{L}}\right)\left(\overline{\mathbf{b}}_\text{M} - \frac{1}{3}\overline{I}_{\text{M}_1}\mathbf{1}\right)}_{\mathbf{s}^{\text{eq}}} + \underbrace{\sum_k^{N_1}\frac{1}{J}\mu_k^{\text{neq}}\left(\overline{\mathbf{b}}_k^\text{e} - \frac{1}{3}\overline{I}_{1k}^\text{e}\mathbf{1}\right)}_{\mathbf{s}^{\text{neq}}} + \underbrace{\frac{1}{2J}\kappa\left(J_\text{M}^2 - 1\right)}_{p}\mathbf{1}, \tag{3.7}$$

where $\overline{\mathbf{b}}_{\mathrm{M}} = \overline{\mathbf{F}}_{\mathrm{M}}\overline{\mathbf{F}}_{\mathrm{M}}^{\mathrm{T}}$ and $\overline{\mathbf{b}}_{\mathrm{k}}^{e} = \overline{\mathbf{F}}_{\mathrm{k}}^{e}\overline{\mathbf{F}}_{\mathrm{k}}^{e\mathrm{T}}$ are the left Cauchy-Green deformation tensor of the mechanical deformation and its elastic component. The latter is an internal variable describing the departure from the equilibrium mechanical response. The variables $\overline{I}_{\mathrm{M_1}} = \mathbf{I} : \overline{\mathbf{b}}_{\mathrm{M}}$ and $\overline{I}_{1k}^{e} = \mathbf{I} : \overline{\mathbf{b}}_{\mathrm{k}}^{e}$ are the first invariant of the left Cauchy-Green deformation tensors, while $\overline{\lambda}_{\mathrm{eff}} = \sqrt{\frac{1}{3}\overline{I}_{\mathrm{M_1}}}$ denote the effective chain stretch of the Arruda-Boyce[126] network model. The following nonlinear evolution equation[127] is adopted for internal viscoelastic variable $\mathbf{b}_k^e$,

$$-\frac{1}{2}\mathcal{L}_v\mathbf{b}_k^e\mathbf{b}_k^{\mathrm{e\text{-}1}} = \frac{1}{2\upsilon_{\mathrm{S}_k}}\mathbf{s}_k^{\mathrm{neq}}, \tag{3.8}$$

where $\upsilon_{\mathrm{S}k}$ is the shear viscosity dependent of the temperature, fictive temperature, solvent concentration, and flow stress $s = \sqrt{\frac{1}{2}\mathbf{s}^{\mathrm{neq}} : \mathbf{s}^{\mathrm{neq}}}$. The shear relaxation time is defined from the shear viscosity as, $\tau_{\mathrm{S}k} = \upsilon_{\mathrm{S}k}/\mu_k^{\mathrm{neq}}$.

3.2.3.1 Relaxation Time of a Polymer-Solvent System:

Previously, we applied the Adam-Gibbs[39] model to describe the temperature dependence of the structural and stress relaxation times. The central hypothesis of the Adam-Gibbs model is that network rearrangements in response to decreasing temperatures require the cooperative motion of progressively larger number of molecular groups. By relating the number of cooperatively rearranging groups to the configurational entropy S_c, Adam and Gibbs[39] developed a formulation for the structural relaxation time that depends inversely on S_c,

$$\tau_R = A\exp\left(\frac{B}{TS_c}\right), \tag{3.9}$$

where A and B are a scaling parameters. For a system in thermodynamic equilibrium, we assume that the configurational entropy of the polymer-solvent system depends on the temperature and number of solvent molecules, $S_c(N,T)$. For a dilute system, we further assume that the presence of solvent molecules in low numbers contributes a small increment to the configurational entropy of the pure polymer system that depends only on the number of solvent molecules,

$$S_c(N,T) = S_c(0,T) + \Delta S_c(N). \tag{3.10}$$

This assumption was used by Chow[89] to develop a statistical mechanics model for the effect of dilute solvent concentration on the glass transition temperature. The model was applied successfully to predict the decrease in the glass transition temperature of polystyrene with absorption of a variety of organic solvent molecules. We adopt the approach of Chow[89] here to develop an extension of the Adam-Gibbs model for the effect of the dilute solvent concentration on the relaxation times.

The entropy of a system in equilibrium can be determined from the configurational partition function Q as,

$$S_c = k \ln Q + kT \left(\frac{\partial \ln Q}{\partial T} \right)_p, \tag{3.11}$$

where k is the Boltzmann constant. Substituting eq. (3.11) into eq. (3.10) gives,

$$\Delta S_c = k \ln \left(\frac{Q(N,T)}{Q(0,T)} \right) + kT \frac{\partial}{\partial T} \left(\ln \left[\frac{Q(N,T)}{Q(0,T)} \right] \right)_p. \tag{3.12}$$

The Brag-Williams theory[148] is used to evaluate the ratio of partition functions in eq.

(3.12), for the possible arrangements of small solvent molecules in the polymer lattice. The partition function $Q(N,T)$ represents N solvent molecules randomly distributed among $N+L$ lattice sites, where L is the number of empty lattice sites, while the partition function $Q(0,T)$ represents the state before mixing ($N=0$). The ratio of partition functions $Q(N,T)/Q(0,T)$ can be written as,[89]

$$\frac{Q(N,T)}{Q(0,T)} = \frac{(N+L)!}{N!L!}\exp -\frac{E}{kT}. \tag{3.13}$$

where E is the change in interaction energy caused by mixing. Defining the lattice coordination number as z and ϵ_{NN}, ϵ_{LL} and ϵ_{NL} as the energies of each NN, LL, and NL pair, E can be estimated as follows,

$$\begin{aligned} E =& \frac{z}{2}(N+L)\left(\frac{N^2}{(N+L)^2}\epsilon_{NN} + 2\frac{NL}{(N+L)^2}\epsilon_{NL} + \frac{L^2}{(N+L)^2}\epsilon_{LL}\right) - \frac{z}{2}N\epsilon_{NN} - \frac{z}{2}L\epsilon_{LL} \\ =& -\frac{zNL}{N+L}\left(\epsilon_{NN} + \epsilon_{LL} - 2\epsilon_{NL}\right). \end{aligned} \tag{3.14}$$

The first term in the above equation is the interaction energy after mixing and the last two terms are the interaction energy before mixing.

Substituting eq. (3.13) and (3.14) into eq. (3.12) and applying Stirling's approximation, $\ln(N!) = N\ln N - N$, gives the following

$$\Delta S_c = -\zeta[\theta\ln(\theta) + (1-\theta)\ln(1-\theta)], \tag{3.15}$$

where $\zeta = k(N+L)$ and $\theta = \frac{N}{N+L}$ is the solvent number fraction. Note that while we assumed that the entropy change ΔS is temperature independent in eq. (3.10), the result is achieved by using the Bragg-Williams theory. The number of solvent molecules N and

the number of the total lattice sites $N + L$ are defined for the polymer-solvent system as follows,

$$N = \frac{m_s N_A}{M_s}, \quad N + L = \frac{z m_p N_A}{M_p}, \tag{3.16}$$

where m_s, m_p are the mass and M_s , M_p are the molar mass of the solvent and polymer respectively, and N_A is Avogadro's number. This allows ζ and the number fraction θ to be expressed in terms of the following form as,

$$\zeta = \frac{z m_p R}{M_p}, \quad \theta = \frac{M_p}{z M_s}\phi, \tag{3.17}$$

where R is the gas constant.

For a nonequilibrium polymer-solvent system, we assume that the configurational entropy near equilibrium can be similarly decomposed as in eq. (3.10) into a contribution for the nonequilibrium pure polymer system dependent on the fictive temperature T_f and an increment dependent on the number of solvent molecules,

$$S_c\left(N, T_f\right) = S_c\left(0, T_f\right) + \Delta S_c\left(N\right). \tag{3.18}$$

Furthermore, we assume that ΔS_c has the same dependence on the solvent concentration as eq. (3.15). The nonlinear Adam-Gibbs model is applied for $S_c\left(0, T_f\right)$,[39,42,121]

$$S_c\left(0, T_f\right) = C\left(\frac{1}{T_2} - \frac{1}{T_f}\right), \tag{3.19}$$

where C is a scaling parameter and T_2 is the Kauzmann temperature for an ideal glass.

Combining eq. (3.9), (3.10), (3.15), and (3.19), gives the following explicit function for the dependence of the structural relaxation time for each relaxation process on the temperature, nonequilibrium structure, and solvent concentration,

$$\tau_{R_k}(T, T_f, \theta) = A_k \exp\left(\frac{B/\zeta}{T\left(C/\zeta[\frac{1}{T_2} - \frac{1}{T_f}] - [\theta\ln(\theta) + (1-\theta)\ln(1-\theta)]\right)}\right) = A_k a\left(T, T_f, \theta\right). \tag{3.20}$$

The function $a\left(T, T_f, \theta\right)$ is defined as the shift factor. For the purpose of parameter identification, we define the relaxation time for the dry polymer system ($\theta = 0$) at an equilibrium reference temperature as, $\tau^g_{R_k} = \tau_{Rk}(T^{\text{ref}}_{\text{g}}, T^{\text{ref}}_{\text{g}}, 0)$, where $T^{\text{ref}}_{\text{g}}$ is the glass transition temperature measured for a reference cooling rate. This allows the structural relaxation time of the polymer-solvent system to be expressed relative to the dry system at the reference temperature as follows,

$$\begin{aligned} \tau_{R_k}(T, T_f, \theta) &= \tau^g_{R_k}\frac{a(T, T_f, \theta)}{a(T^{\text{ref}}_{\text{g}}, T^{\text{ref}}_{\text{g}}, 0)}, \\ a(T^{\text{ref}}_{\text{g}}, T^{\text{ref}}_{\text{g}}, 0) &= \exp\left(\frac{B/\zeta}{T^{\text{ref}}_{\text{g}}C/\zeta\left(\frac{1}{T_2} - \frac{1}{T^{\text{ref}}_{\text{g}}}\right)}\right). \end{aligned} \tag{3.21}$$

For the dry polymer system, the expression for the relaxation time can be written as Nguyen et al.,[45]

$$\tau_{R_k}\left(T, T_{\text{f}}, 0\right) = \tau^{\text{g}}_{R_k}\exp\left[-\frac{C^{\text{g}}_1}{\log e}\left(\frac{C^{\text{g}}_2\left(T - T_{\text{f}}\right) + T\left(T_{\text{f}} - T^{\text{ref}}_{\text{g}}\right)}{T\left(C^{\text{g}}_2 + T_{\text{f}} - T^{\text{ref}}_{\text{g}}\right)}\right)\right], \tag{3.22}$$

where C^{g}_1 and C^{g}_2 are the WLF constants defined at the reference glass transition temperature.

We assume that the stress relaxation time has the same dependence on temperature, structure, and solvent concentration. To represent the stress-activated viscoplastic flow behavior, we further assume that the stress relaxation time also depends on the flow stress according to a modified Eyring model.[77] In the modified Eyring model, the Arrhenius temperature dependence is replaced by the Adam-Gibbs dependence on temperature, structure, and solvent concentration in equation (3.23),

$$\tau_{S_k}(T, T_f, \theta, s) = \tau^g_{S_k} \frac{a(T, T_\mathrm{f}, \theta)}{a(T^\mathrm{ref}_\mathrm{g}, T^\mathrm{ref}_\mathrm{g}, 0)} \frac{Q_S}{T} \frac{s}{s_y} \left[\sinh\left(\frac{Q_S}{T}\frac{s}{s_y}\right)\right]^{-1}, \tag{3.23}$$

where $\tau^g_{S_k}$ is the stress relaxation time at $T^\mathrm{ref}_\mathrm{g}$. The parameter Q_s is a scaling parameter, s_y is the yield strength and the flow stress s. Lastly, to incorporate the strain softening phenomena in the glassy state, the phenomenological evolution equation developed by Boyce et al.[149] is used for yield strength,

$$\dot{s}_\mathrm{y} = \frac{1}{\tau_y}\frac{T}{Q_S}\sinh\left(\frac{Q_S}{T}\frac{s}{s_y}\right)\frac{a(T^\mathrm{ref}_\mathrm{g}, T^\mathrm{ref}_\mathrm{g}, 0)}{a(T, T_\mathrm{f}, \theta)}\left(1 - \frac{s_\mathrm{y}}{s_{\mathrm{y}_{ss}}}\right)s_y, \quad s_\mathrm{y}\,(t=0) = s_{\mathrm{y}_0}, \tag{3.24}$$

where s_{y_0} and $s_{\mathrm{y}_{ss}}$ are the initial and steady-state yield strength.

3.2.4 Finite Element Model

The constitutive model was implemented in an open-source finite element program Tahoe© (Sandia National Laboratories) [2] and applied to simulate the isothermal recovery behavior of specimens in air and water to validate the model. We modeled both the rectangular and tube specimens described in Sec 3.2.2.4. Figure 3.3 shows the finite element

[2] http://sourceforge.net/projects/tahoe/

model of the rectangular tension specimen. Only one eighth of the specimen was simulated because of symmetry. The mesh was discretized using trilinear hexahedral elements, and a mesh convergence study was performed to determine the mesh density. The finite element model solved both the Fickian diffusion problem for the time-dependent spatial distribution of the solvent concentration,

$$c = \frac{\phi}{1+\phi} \tag{3.25}$$

and the mechanics problem for the deformation and stress response of the specimens. An iterative staggered scheme was applied to couple the two problems. The diffusion problem was solved to calculate the solvent concentration c_{n+1} at time $n+1$. This was used to solve the mechanics problem for the displacement field, and the process was repeated until the solution for both converged. The displacement boundary conditions for the mechanics problem during the programming stage at $T = 60°\text{C}$ were set as follows,

$$u_x(x=0,y,z)=0, u_y(x,y=0,z)=0, u_z(x,y,z=0)=0, u_z(x,y,z=10)=u(t), \tag{3.26}$$

where the applied displacement $u(t)$ resulted in an engineering strain of 25% after 100 seconds. The remaining boundaries were left traction free. The temperature was decreased to either 25°C or 30°C at a rate of 5°C/min and held constant for an additional 5 minutes. The strip was unloaded by applying a traction boundary condition at the top surface $z = 10$ mm that decreased to zero at a constant rate over a period of 20 seconds. To simulate shape recovery in water, the diffusion problem was solved with the initial condition $c(x, y, z, t \leq t_r) = 0$, where t_r is the time at the beginning of the recovery step. The boundary conditions

for the solvent concentration were,

$$c(x = 0.375, y, z, t \geq t_r) = c_\infty, c(x, y = 2.5, z, t \geq t_r) = c_\infty, c(x, y, z = 10, t \geq t_r) = c_\infty, \tag{3.27}$$

where c_∞ is the equilibrium concentration at the recovery temperature. Zero flux was specified for the remaining boundaries.

For the tube geometry, we modeled the 2D plane strain problem rather than the full 3D problem to reduce the computational time. Figure 3.4 shows the finite element model for the tube geometry. The mesh was discretized by bilinear quadrilateral elements. A significantly higher mesh density was chosen where there would be large bending stresses. A mesh convergence study was performed to determine the mesh density. The bottom point of the tube, $x = 0,\ y = 0$, was fixed in x and y to remove rigid body motions. A spherical indenter with radius $r = 0.5$mm with a modulus 1000 times greater the glassy modulus of the SMPs was used to deform the tube at $T = 60°$C at a velocity of 0.18mm/s for 100 seconds. The temperature was decreased from the initial 60°C to the recovery temperature at a rate of 5°C/minutes, under the constraint of the spherical indenter. The temperature was held constant for 5 minutes before removing the constraint. To simulate recovery in water, the diffusion problem was solved with solvent concentration at the inner and outer surfaces set at c_∞. The initial concentration was set to zero to represent the dry polymer.

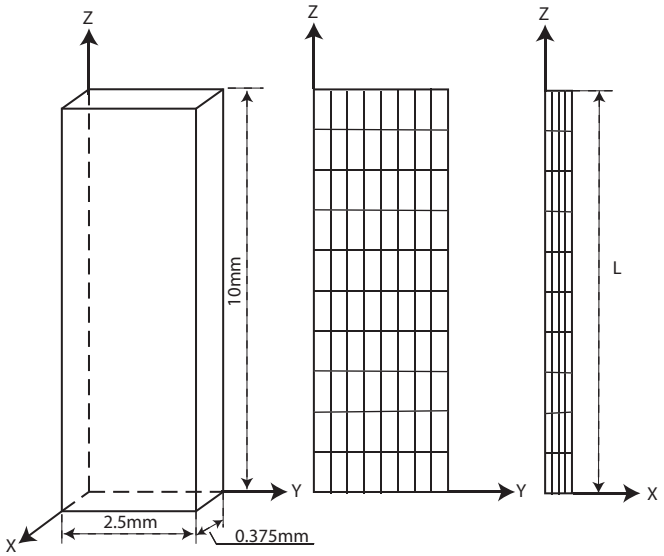

Figure 3.3: Finite element model of rectagular sample

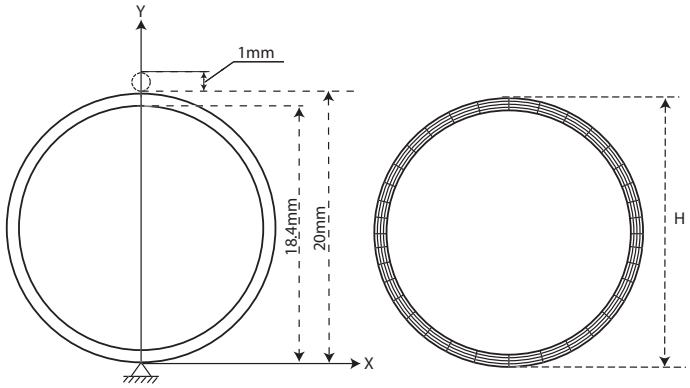

Figure 3.4: Finite element model of stent sample

3.3 Parameter determination

The parameters and relaxation spectra, obtained from thermomechanical tests previously described in,[45,78,79,145] are listed in Table 3.1. The discrete stress and structural relaxation spectrum are given in Tables 3.2 and 3.3. The following describes methods developed to measure the diffusion constant and parameters for the shift factor of the polymer-solvent system in eq. (3.21).

3.3.1 Relaxation Times

The density of the polymer and water for this study were $1.12g/cm^3$ and $1.0g/cm^3$. For the polymer-solvent system, the following additional parameters were determined for the relaxation time: the molar mass for the solvent and polymer M_s and M_p as well as the coordination number z in eq.(3.17), the Kauzmann temperature T_2, and the scaling parameters B/ζ and C/ζ in eq. (3.20). The MA-MMA-PEGDMA polymer system was composed of two monomers, methyl acrylate and methyl methacrylate, with molar mass $86g/mol$ and $100g/mol$ respectively. Since the ratio between the two monomers was 5:4, the molar mass of the copolymer was approximated as $M_p = 92g/mol$. We neglected the crosslinker contribution, considering the polymer was lightly cross-linked. We assumed $z = 1$ for the coordination number. The remaining three parameters, B/ζ, C/ζ and T_2, were obtained from dynamic frequency sweep tests described in Sec. 3.2.2.2. We first applied the frequency tests at multiple temperatures to construct the master curve of the storage modulus

Table 3.1: Parameters of the constitutive model for the polymer-solvent system.

Parameter	**Values**	**Physical significance**
$\alpha_{\mathrm{r}}(10^{-4}/^{\mathrm{o}}\,\mathrm{C})$	6.33	rubbery coefficient.
$\alpha_{\mathrm{g}}(10^{-4}/^{\mathrm{o}}\,\mathrm{C})$	1.8	glassy coefficient.
$\xi(10^{-6}s)$	7.0	stress relaxation time at T_{ref} $(75^{o}C)$.
α	0.66	stress relaxation spectrum breadth
$\chi(s)$	80	structural relaxation time at $T = T_{\mathrm{g}}^{\mathrm{ref}}$.
β	0.3	structural relaxation spectrum breadth
$T_2(^{\mathrm{o}}\mathrm{C})$	1.7	Kauzmann temperature.
B/ζ	5395	scaling parameter related with activation energy.
C/ζ	1377	scaling parameter related with configurational heat capacity.
μ_{N} (MPa)	0.96	shear modulus of equilibrium network.
λ_{L}	4	limiting chain stretch of equilibrium network.
μ_{neq} (MPa)	443.3	non-equilibrium shear modulus .
κ (MPa)	1666.7	bulk modulus.
$Q_{\mathrm{S}}/s_{\mathrm{y}_0}(^{\mathrm{o}}\mathrm{K/MPa})$	110	activation parameter for viscous flow.
$s_{\mathrm{y}_{\mathrm{ss}}}/s_{\mathrm{y}_0}$	0.43	ratio of steady-state to initial yield strength.
τ_y (MPa)	5000	characteristic yield time.
c_{∞}^{1} (%)	2.28	equilibrium water concentration at 25 ^{o}C.
c_{∞}^{2} (%)	2.36	equilibrium water concentration at 30 ^{o}C.
$D_1(mm^2/s)$	$3.94 * 10^{-6}$	water diffusion coefficient at 25 ^{o}C.
$D_2(mm^2/s)$	$5.41 * 10^{-6}$	water diffusion coefficient at 30 ^{o}C.

and determined the WLF constants C_1^g and C_2^g at $T_{\mathrm{g}}^{\mathrm{ref}}$ for the dry polymer as described in.[27,78,145] The Kauzmann temperature and the ratio of the two scaling parameters $\frac{B/\zeta}{C/\zeta}$ are related to the WLF constant C_1^g and C_2^g as,

$$\frac{B}{C}T_2 = \frac{C_1^g C_2^g}{\log e}, \quad T_2 = T_{\mathrm{g}}^{\mathrm{ref}} - C_2^g. \tag{3.28}$$

To calculate B/ζ and C/ζ, we performed a dynamic frequency sweep test at room temperature T_r to measure the storage modulus of the saturated polymer. We then shifted the storage modulus of the saturated material at T_r to the master curve of dry polymer at a reference temperature $T_{\mathrm{ref}} = 75°\mathrm{C}$ to obtain the frequency shift Δ as shown in Fig. 3.5. From eq. 3.20, Δ is related to the parameters as follows,

$$\begin{aligned}\Delta &= \frac{a(T_r, T_r, \theta_\infty)}{a(T_{ref}, T_{ref}, 0)} \\ &= \exp\left(\frac{B/\zeta}{T_r\left(C/\zeta[\frac{1}{T_2} - \frac{1}{T_r}] - [\theta_\infty \ln(\theta_\infty) + (1-\theta_\infty)\ln(1-\theta_\infty)]\right)} - \frac{B/\zeta}{T_{ref}\left(C/\zeta[\frac{1}{T_2} - \frac{1}{T_{ref}}]\right)}\right),\end{aligned} \tag{3.29}$$

where θ_∞ is the equilibrium solvent number ratio, which is related with equilibrium mass ratio through eq. 3.17. This method assumes that the saturated specimen is in structural equilibrium at T_r. This is reasonable because the storage modulus measured for the saturated system is within the glass transition region (Fig. 3.5). We also observed in experiments that the storage modulus did not evolve with aging time for the saturated sample. Combing eq. (3.28) and eq. (3.29) yields the parameters B/ζ and C/ζ.

Table 3.2: Discrete structural relaxation spectrum of dry MA-MMA-PEGDMA determined from the parameters χ and β in Table 3.1 as described in Xiao et al.[145]

k	τ_{Rk}^{g} (sec)	$\frac{\Delta\alpha_k}{\Delta\alpha}$
1	0.0008	0.0305
2	0.0052	0.0242
3	0.0335	0.0412
4	0.2171	0.0685
5	1.4060	0.1092
6	9.1036	0.1611
7	58.944	0.2049
8	381.65	0.1982
9	2471.1	0.1202
10	16000	0.0418

Table 3.3: Discrete stress relaxation spectrum of dry MA-MMA-PEGDMA determined from the parameters ξ and α in Table 3.1 as described in Xiao et al.[145]

k	τ_{Sk}^{g} (sec)	$\frac{\Delta\mu_k}{\Delta\mu}$
1	0.0111	0.0035
2	0.0668	0.0081
3	0.4009	0.0278
4	2.4055	0.1016
5	14.433	0.2912
6	86.598	0.3392
7	519.59	0.1629
8	3117.5	0.0447
9	18705	0.0128
10	112231	0.0055

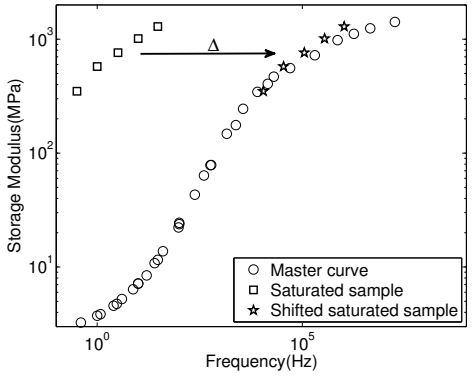

Figure 3.5: Dynamic frequency sweep tests

3.3.2 Solvent Diffusion

We applied Fick's second law to model the time-dependent diffusion process of the polymer-solvent system. While Fick's law is not valid for systems far below T_g, where solvent uptake occurs by case II diffusion,[137, 150–152] our system is sufficiently near T_g that Fick's law can be used to accurately describe the time-dependent results of the diffusion tests detailed in Sec. 3.2.2.1.We solved the diffusion equation for the solvent concentration, with the boundary condition $c = c_\infty$ at the surface and initial condition $c = 0$ at $t = 0$. The results for the solvent concentration can be written as,

$$c(x,y,z,t) = c_\infty - c_\infty \sum_{l,m,n=0}^{\infty} \frac{64\exp\left[-D(\alpha_l^2+\beta_m^2+\gamma_n^2)t\right]}{\alpha_l\beta_m\gamma_n L_1 L_2 L_3} cos(\alpha_l x)cos(\beta_m y)cos(\gamma_n z)$$
$$\alpha_l = (2l+1)\frac{\pi}{L_1}, \quad \beta_m = (2m+1)\frac{\pi}{L_2}, \quad \gamma_n = (2n+1)\frac{\pi}{L_3}, \tag{3.30}$$

where D is the diffusion coefficient and c_∞ is the equilibrium solvent concentration. To experimentally determine the diffusion constant and c_∞ for the MA-MMA-PEGDMA ma-

terial, we measured the solvent weight fraction of four samples immersed in de-ionized water at 25°C and 30°C. The solvent weight fraction at any given time t is defined as:

$$\overline{c}\,(t) = \frac{W(t) - W(0)}{W(\infty)}, \tag{3.31}$$

where $W(0)$, $W(t)$, and $W(\infty)$ refer to the initial weight of the dry specimen, wet specimen at time t, and the saturated specimen. The analytical solution for the weight fraction of the specimen at time t can be obtained as follows assuming small solvent concentration,

$$\overline{c}(t) = \frac{\int_{-L_1/2}^{L_1/2}\int_{-L_2/2}^{L_2/2}\int_{-L_3/2}^{L_3/2} c(x,y,z,t)dxdydz}{L_1L_2L_3} = c_\infty - c_\infty \sum_{l,m,n=0}^{\infty} \frac{8^3 \exp\left[-D(\alpha_l^2+\beta_m^2+\gamma_n^2)t\right]}{\alpha_l^2\beta_m^2\gamma_n^2 L_1^2L_2^2L_3^2} \tag{3.32}$$

We obtained the equilibrium concentration c_∞ and the diffusion coefficient D by fitting equation (3.32) to the experimental data as shown in Fig. 3.6. It was found that the equilibrium solvent concentration and diffusion coefficient at 30^oC are larger than at 25^oC, which was also observed in Chen et al.[153] The diffusion parameters are listed in Table 3.1.

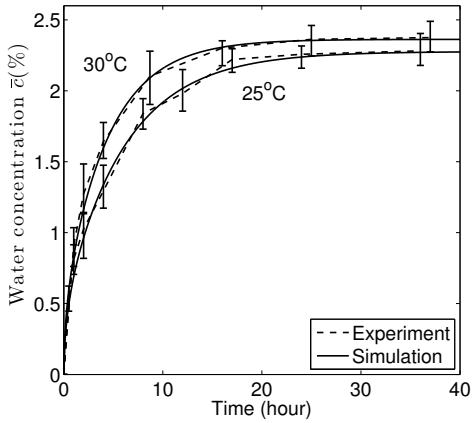

Figure 3.6: The experimental and simulation results for water diffusion tests

3.4 Results and Discussion

3.4.1 Isothermal Stress Response

Fig. 3.7 compares the experimental data and simulation results for the isothermal, uniaxial tension stress-strain response of dry and saturated specimens at room temperature. The results showed the dry specimen exhibited a typical hard glassy response with a yield point, post-yield softening, and viscoplastic flow. As expected, the saturated sample showed a compliant rubbery response without a definite yield point. The diffusion of solvent molecules into the polymer matrix reduced the glass transition temperature from above to below the room temperature resulting in the dramatic softening of the stress response. The simulation results agreed well with the experimental data; though the model slightly underestimated the stress response of the saturated specimen. This may be caused by the loss of hydration during the experiment.

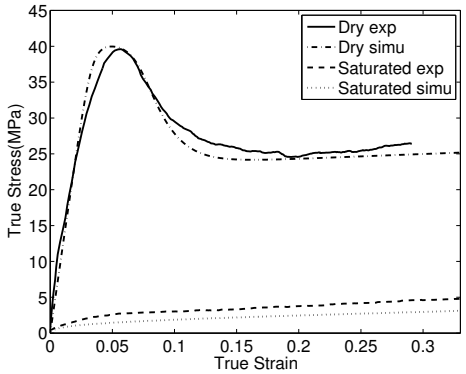

Figure 3.7: The stress-strain response for dry and saturated specimens at room temperature

3.4.2 Isothermal Recovery

Fig. 3.8 plots the experimental data and model prediction for the shape memory cycle, including the programming and isothermal recovery stage, of dry uniaxial tension specimens. Shape recovery was measured as a decrease in the shape fixity ratio, defined in eq. (3.1). The results showed the recovery rate increased with increased recovery temperatures. At 41^{o}C less than 30% deformation was recovered after one hour, while at 50^{o}C full recovery was achieved after 15 minutes. For the dry MA-MMA-PEGDMA material,

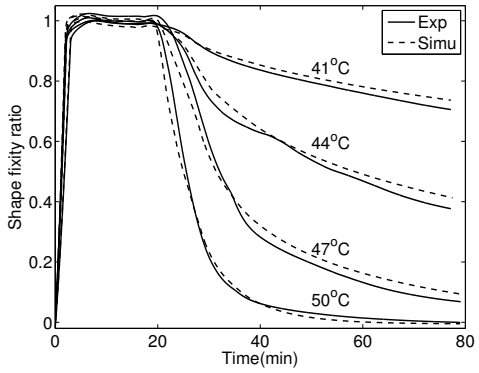

Figure 3.8: The experimental and simulation results for recovery of tension specimens in air

shape-memory programmed specimens showed negligible recovery after months storage at room temperature. However, the programmed specimens experienced a significant loss of shape fixity after it was immersed in water for several hours. Fig. 3.9 plots the shape fixity ratio for the isothermal recovery of specimens immersed in water at 25°C and 30°C. The specimens recovered to their original length after 8 hours at 25^{o}C and 4 hours at 30^{o}C. The model prediction showed good agreement with experimental results at 30°C but predicted

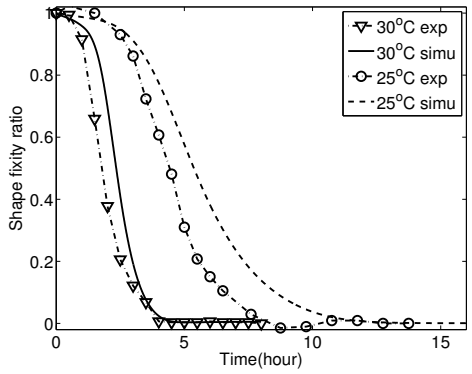

Figure 3.9: The experimental and simulation results for recovery of tension specimens in water

a longer recovery time, 11 hours rather than 8, for 25°C.

For tube specimens, Fig. 3.10 compares the experimentally measured and predicted specimen shape at different time points during recovery in water at 30^oC. Fig. 3.11 plots the shape fixity ratio defined in eq. (3.2) for both temperatures. The model prediction and experimental measurements showed excellent agreement.

3.5 Conclusions

Thermally activated shape-memory polymers have been extensively investigated both in experimental and modeling studies. However, the challenge of heating the SMP device to an activation temperature restricts the use of these smart materials in biomedical applications. The solvent-driven shape-memory effect is a possible solution to this limitation. The absorption of solvent in low concentration lowers the glass transition temperature allowing

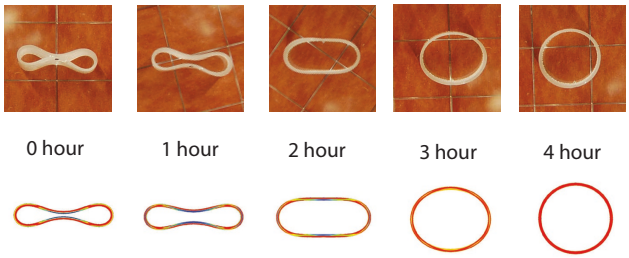

Figure 3.10: The momentary shape of stent samples in both experiments and simulation in 30°C water bath

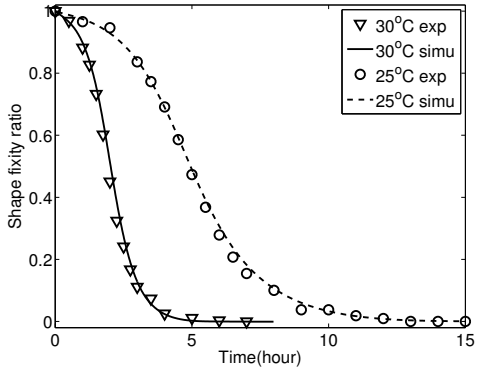

Figure 3.11: The experimental and simulation results for recovery of stent specimens in water

for athermal shape deployment. This process also changes the mechanical properties by dramatically reducing the stiffness and strength. For devices designed to be mechanical structures upon deployment, solvent absorption may significantly compromise the long-term load-bearing capability of the device. In this work, we developed a constitutive model to describe the effect of solvent on the thermomechanical properties of amorphous networks. The solvent increases the chain mobility by increasing the configurational entropy. The result is a decrease in the relaxation time and T_g. We extended the Adam-Gibbs model to describe this physical process. The model was implemented for finite element analy-

sis and computational models were developed to study the isothermal recovery behavior of specimens in air and water. The models also considered the diffusion process to accurately represent the real recovery process. The model was able to predict quantitatively the dramatic softening of the stress response of the saturated material and the time-dependent solvent-driven shape recovery. The results show that the constitutive model developed here is capable of describing the solvent-driven shape-memory effect. In biomedical applications, the SMP devices may be designed to assume a complex temporary shape and shape recovery path. The present work can assist this design process by predicting the effect of the shape-memory programming process and deployment conditions (e.g. temperature, solvent) on the shape recovery process. The polymer investigated in this work only absorbs low concentrations of solvent and the solvent-driven recovery time of the polymer is on the magnitude of hours. In the future, we will investigate polymer systems capable of large solvent absorption and rapid diffusion. This will require the development of a fully coupled thermodynamic theory for the mechanical and diffusion processes.

Chapter 4

An Effective Temperature Theory for the Nonequilibrium Behavior of Amorphous Polymers

This chapter will be submitted to Journal of the Mechanics and Physics of Solids, under the title “An Effective Temperature Theory for the Nonequilibrium Behavior of Amorphous Polymers", with T. D. Nguyen as co-authors.

In this chapter, we developed a thermomechanical theory that introduces the effective temperature as a thermodynamic state variable representing the nonequilibrium configurational structure to describe the influence of structural evolution on the inelastic behavior and physical properties of amorphous polymers. The theory couples the evolution of the effective temperature and internal state variables to describe the temperature-dependent

and rate-dependent inelastic response through the glass transition. We applied the theory to model the effect of temperature, strain rate, aging time, and plastic pre-deformation on the uniaxial compression response and enthalpy change with temperature of an acrylate network. The results showed excellent agreement with experiments and demonstrate the ability of the effective temperature theory to explain the complex thermomechanical behavior of amorphous polymers.

4.1 Introduction

Amorphous polymers exhibit a wide range of complex time-dependent and temperature-dependent behavior, from elastic and rubbery to viscoplastic and glassy. The physical properties of amorphous polymers are determined by the mobility of structural components spanning multiple length-scales, and these can be observed macroscopically as temperature-dependent relaxation processes occupying multiple time-scales. At high temperatures, the polymer structures are mobile and can rearrange quickly in response to a mechanical load or temperature change. The mobility decreases with the temperature, and cooling drives an initially rubbery material out of equilibrium and induces the glass transition. The glass transition is an inherently time-dependent process, and the glass transition temperature T_g changes with the cooling rate. Slower cooling rates produce lower glass transition temperatures, because more time is available for the polymer structure to rearrange towards an equilibrium configuration.[31] Whether the glass transition temperature has an equilibrium

limit is an open question. However, structural relaxation[121] can be observed readily near the glass transition as the time-dependent evolution of thermodynamic properties, such as volume and enthalpy, to equilibrium.[75,90–93] The effect of structural relaxation can also be observed in the mechanical behavior of glassy polymers as physical aging, where the flow-resistance and yield strength increase with time.[154] The structure of amorphous glasses can be rejuvenated to a more mobile state by plastic deformation,[93,155] and mechanical rejuvenation is responsible for the strain-softening behavior following yield in polymer glasses. Large plastic deformation also decreases the yield strength and erases the yield peak developed from structural relaxation.[93,95] In differential scanning calorimetry measurements (DSC), structural relaxation produces an endothermic overshoot at the T_g, that increases with annealing time corresponding to the yield strength. Large plastic deformation erases the endothermic overshoot at T_g and induces a pre-T_g exothermic undershoot that increases with plastic strain and corresponds to the post-yield strain-softening.[29]

Modeling the nonequilibrium behavior of amorphous polymers is important for fundamental studies of the glass transition and for practical applications, such as improving manufacturing processes (e.g., hot embossing) and controlling material performance (e.g., shape memory behavior) that operate through the glass transition. Though viscoelasticity and structural relaxation both arise from time-dependent structural rearrangements, they are described by different theoretical approaches. The internal state variable thermodynamics theory, introduced by Coleman and Gurtin[156] has been applied successfully to model the viscoelastic behavior of elastomers above the T_g[124,127,157] and the viscoplastic behavior of

glassy polymers below T_g.[63,64,68,71] The stress response is derived from a free energy density that depends on the total deformation and internal state variables describing the effects of inelastic deformation. The theory provides a definition for the internal dissipation, and temperature-dependent evolution equations are prescribed for the internal variables to guarantee positive dissipation. Additional structural variables, such as the yield strength, are introduced and evolved with the plastic strain rate to model strain-softening.[95,158] Recent efforts have applied the internal state variable theory to describe the glass transition,[65,71,72] where temperature-dependent moduli are prescribed to describe the dramatic change in the mechanical properties during the glass transition.

Tool[122] introduced the fictive temperature approach for modeling structural relaxation in glasses. In a cooling experiment, the fictive temperature T_f is defined as the equilibrium temperature from which the material is quenched to obtain a property at the current temperature. Tool[122] developed a nonlinear first order evolution equation for T_f towards the equilibrium temperature T, where the relaxation time depends on T and T_f to account for the changing structure of the glass. These features allowed the model to describe the dependence of T_g on the cooling rate, asymmetry in the structural relaxation response to cooling and heating, and hysteresis in the temperature dependence during a cooling-heating cycle. Subsequent developments for polymers have produced more physical models for the temperature- and structure-dependence of the relaxation time,[39,42,76] and introduced a distribution of relaxation times[96,120,159,160] to describe the memory effects observed after multiple temperature treatments. Recent glass-rubber models have applied a fictive temperature

dependence in the viscosities and plastic strain rate to describe physical aging and mechanical rejuvenation of the yield and post-yield behavior of glassy polymers.[45,78,79,99,106,161]

The ability of the fictive temperature concept to describe the nonequilibrium behavior of glasses has motivated the development of nonequilibrium theories that recasts the fictive temperature, renamed the effective temperature, as a thermodynamic state variable. The central idea of effective temperature theories is the degrees of freedom of a glass can be decomposed into a fast vibrational mode that equilibrates instantaneously and slow configurational modes that exist in a quasi-equilibrium state, characterized by an effective temperature (see for example[100–105]). The fast and slow modes have different entropies and internal energies, and can be thought as weakly interacting material subsystems.[129] The existence of an effective temperature as a thermodynamic state variable that is connected to the configurational entropy is supported by molecular dynamics simulations of an aging glass system,[162,163] simulations of athermal systems,[164,165] and granular systems.[166] The issue of whether the effective temperature is a true thermodynamic state variable is far from settled, and Leuzzi[104] provides an in-depth discussion of the distinction between the fictive and effective temperature concepts. Recent models of inelastic deformation in amorphous materials have integrated the effective temperature and internal state variable frameworks.[129,167,168] Bouchbinder and Langer extended the shear transformation zone theory to describe the linear rate-dependent behavior and the Kovacs memory effect[169,170] of polymer glasses. Karmin and Bouchbinder[171] developed a two-temperature thermomechanical theory, that explicitly considers the interaction of two thermodynamic subsystems,

and showed that the theoretical framework can produce a wide range of nonequilibrium deformation behavior of amorphous materials.

In this work, we develop an effective temperature theory for the coupled thermomechanical behavior of amorphous polymers. We adopt the basic idea that the behavior of the glass can be decomposed into fast kinetic processes at the equilibrium temperature and multiple slowly evolving configurational processes at different effective temperatures. The concept of multiple configurational processes are introduced to accurately represent the broad relaxation spectrum of polymers. The kinetic and configuration processes are characterized by different internal energies, entropies, heat flux, and entropy flux, the sum of which gives the properties of the system. We begin by decomposing the balance of energy into sub-balances for the kinetic and configurational subsystems, which requires introducing heat conduction between the subsystems. This approach was first applied by Kamrin and Bouchbinder,[171] and results in an energy balance for the configurational subsystems that describes mechanical rejuvenation and configurational temperature diffusion. The energy sub-balances are applied to develop a reduced entropy inequality that constrains the constitutive relations for heat conduction and internal state variables. We applied the theory to describe the thermomechanical behavior of an acrylate thermoset using parameters previously determined from standard dynamic mechanical analysis and isothermal uniaxial tensile experiments.[45,78,106] The results showed that the effective temperature theory was able to reproduce the temperature-dependent stress response through the glass transition and the effects of physical aging and mechanical rejuvenation on the yield strength of the

glass, without introducing additional structural variables. Calculations of the rate of enthalpy change shows the appearance of an endothermic overshoot at the T_g with physical aging as observed in experiments. Moreover, large inelastic work erased the endothermic overshoot and created an exothermic undershoot before T_g. The effective temperature thermodynamics theory provides a unifying framework to model the wide range of nonequilibrium behavior of amorphous polymers across the glass transition.

4.2 Methods

4.2.1 Nonequilibrium Thermodynamic Framework

We begin with the basic definition of a continuum deformation field, $\mathbf{x} = \varphi(\mathbf{X})$, which uniquely maps points $\mathbf{X}$ in the undeformed material configuration to points $\mathbf{x}$ in the deformed spatial configuration. The deformation gradient is defined as, $\mathbf{F} = \partial\varphi/\partial\mathbf{X}$. To describe the time-dependent inelastic deformation of polymers, we decompose the deformation gradient multiplicatively into N parallel elastic and inelastic components, $\mathbf{F} = \mathbf{F}^{\mathrm{e}}_j\mathbf{F}^{\mathrm{v}}_j$. For simplicity, we do not consider the effect of thermal deformation in the kinematic description, which was incorporated in previous constitutive developments.[45,78,106] The total and elastic right Cauchy-Green deformation tensors describing the stretch of material lines are defined as, $\mathbf{C} = \mathbf{F}^{\mathrm{T}}\mathbf{F}$ and $\mathbf{C}^{\mathrm{e}}_j = \mathbf{F}^{\mathrm{eT}}_j\mathbf{F}^{\mathrm{e}}_j$. We also define the spatial and inelastic velocity gradients as, $\mathbf{L} = \dot{\mathbf{F}}\mathbf{F}^{-1}$ and $\mathbf{L}^{\mathrm{v}}_j = \dot{\mathbf{F}}^{\mathrm{v}}_j\mathbf{F}^{\mathrm{v}-1}_j$.

The local first law of thermodynamics can be written for the reference configuration as,

$$\dot{e} = \mathbf{S} : \frac{1}{2}\dot{\mathbf{C}} - \nabla_{\mathbf{X}} \cdot \mathbf{Q}, \tag{4.1}$$

where $\mathbf{S}$ is the second Piola-Kirchhoff stress tensor, $\mathbf{Q}$ is the nominal heat flux, and e is the internal energy density of the reference configuration. Next, we apply the fundamental postulate that the behavior of the glass can be separated into fast kinetic and slow configurational processes. The configurational processes have different characteristic relaxation times, which cause them to fall out of equilibrium at different states and have different effective temperatures, T_{e_i}. Consequently, the entropy, internal energy and heat flux can be decomposed into kinetic and multiple configurational contributions as,

$$\eta = \eta^k + \sum_i^P \eta_i^c, \quad e = e^k + \sum_i^P e_i^c, \quad \mathbf{Q} = \mathbf{Q}^k + \sum_i^P \mathbf{Q}_i^c. \tag{4.2}$$

The Helmholtz free energy density of the system is defined as,

$$\Psi = \underbrace{e^k - T\eta^k}_{\Psi^k} + \sum_i^P \underbrace{e_i^c - T_{e_i}\eta_i^c}_{\Psi_i^c}. \tag{4.3}$$

The free energy density $\Psi\left(T, T_{e_1}...T_{e_P}, \mathbf{C}, \mathbf{C}_1^{\mathrm{e}}...\mathbf{C}_N^{\mathrm{e}}, \mathbf{A}_1...\mathbf{A}_M\right)$ generally depends on the deformation $\mathbf{C}$, N internal variables for the inelastic deformation gradient $\mathbf{F}_j^{\mathrm{v}}$, through $\mathbf{C}_j^{\mathrm{e}}$, and M additional internal variables $\mathbf{A}_j$ to describe various inelastic deformation mechanisms (e.g, orientation hardening). The first law can be expressed in terms of the free-energy density by combining eqs. (4.1)-(4.3) as,

$$T\dot{\eta}^k + \nabla_{\mathbf{X}} \cdot \mathbf{Q}^k + \sum_i^P T_{e_i}\dot{\eta}_i^c + \sum_i^P \nabla_{\mathbf{X}} \cdot \mathbf{Q}_i^c = \mathbf{S} : \frac{1}{2}\dot{\mathbf{C}} - \eta^k\dot{T} - \sum_i^P \eta_i^c \dot{T}_{e_i} - \dot{\Psi}. \tag{4.4}$$

The time-derivative of the free energy density describes the change in the thermodynamic state and can be evaluated as, $\dot{\Psi} = \mathbf{S} : \frac{1}{2}\dot{\mathbf{C}} - \eta^k \dot{T} - \sum_i^P \eta_i^c \dot{T}_{e_i} - \mathcal{W}^{\text{int}}$, where $\mathcal{W}^{\text{int}} = \sum_j^N \mathbf{C}_j^{\text{e}} \frac{\partial \Psi}{\partial \mathbf{C}_j^{\text{e}}} : \mathbf{L}_j^{\text{v}} - \sum_j^M \frac{\partial \Psi}{\partial \mathbf{A}_j} : \dot{\mathbf{A}}_j$ is the internal power from inelastic behavior. From the decomposition of Ψ in eq. (4.3), the internal power can be partitioned into kinetic and configurational contributions, $\mathcal{W}^{\text{int}} = \mathcal{W}^{\text{int},k} + \sum_i^P \mathcal{W}_i^{\text{int},c}$. At equilibrium, $T_{e_i} = T$ and $\mathcal{W}^{\text{int}} = 0$, and the stress and entropy can be defined from the free energy density as, $\mathbf{S} = 2\frac{\partial \Psi}{\partial \mathbf{C}}$, $\eta^k = -\frac{\partial \Psi}{\partial T}$, and $\eta_i^c = -\frac{\partial \Psi}{\partial T_{e_i}}$. Applying these results to eq. (4.4), we can eliminate the stress power from the first law:

$$T\dot{\eta}^k + \sum_i^P T_{e_i}\dot{\eta}_i^c = -\nabla_{\mathbf{X}} \cdot \mathbf{Q}^k - \sum_i^P \nabla_{\mathbf{X}} \cdot \mathbf{Q}_i^c + \mathcal{W}^{\text{int},k} + \sum_i^P \mathcal{W}_i^{\text{int},c}. \tag{4.5}$$

We now make the following assumptions. 1) Heat Q_i^{kc} flows between the kinetic and configurational subsystems and allows T_{e_i} to equilibrate with T.[171] 2) The configurational subsystems are weakly coupled; thus heat does not flow between the P configurational subsystems. Moreover, η_i^c only depends on T_i^e, deformation and internal variables, and η^k only depends on T, deformation, and internal variables. These assumptions allow the first law to be split into energy balances for each subsystem as,

$$\begin{aligned} T\dot{\eta}^k &= -\nabla_{\mathbf{X}} \cdot \mathbf{Q}^k - \sum_i^P Q_i^{kc} + \mathcal{W}^{\text{int},k} \\ T_{e_i}\dot{\eta}_i^c &= -\nabla_{\mathbf{X}} \cdot \mathbf{Q}_i^c + Q_i^{kc} + \mathcal{W}_i^{\text{int},c}, \quad i = 1...P. \end{aligned} \tag{4.6}$$

Expanding $\dot{\eta}$ and $\mathcal{W}^{\text{int}}$ gives the governing equations for T and T_{e_i},

$$\begin{aligned} c_g \dot{T} = &- \nabla_{\mathbf{X}} \cdot \mathbf{Q}^k - \sum_i^P Q_i^{kc} + \mathcal{W}^{\text{int},k} \underbrace{-T 2 \frac{\partial \eta^k}{\partial \mathbf{C}} : \frac{1}{2}\dot{\mathbf{C}}}_{\mathcal{H}^{\text{e,k}}} \\ &\underbrace{+ T \sum_j^N \mathbf{C}_j^{\text{e}} \frac{\partial \eta^k}{\partial \mathbf{C}_j^{\text{e}}} : \mathbf{L}_j^{\text{v}} - T \sum_j^M \frac{\partial \eta^k}{\partial \mathbf{A}_j} : \dot{\mathbf{A}}_j}_{\mathcal{H}^{\text{in,k}}} \end{aligned} \tag{4.7}$$

$$\begin{aligned} \Delta c_i \dot{T}_{e_i} = &- \nabla_{\mathbf{X}} \cdot \mathbf{Q}_i^c + Q_i^{kc} + \mathcal{W}_i^{\text{int},c} \underbrace{-T_{e_i} 2 \frac{\partial \eta_i^c}{\partial \mathbf{C}} : \frac{1}{2}\dot{\mathbf{C}}}_{\mathcal{H}_i^{\text{e,c}}} \\ &\underbrace{+ T_{e_i} \sum_j^N \mathbf{C}_j^{\text{e}} \frac{\partial \eta_i^c}{\partial \mathbf{C}_j^{\text{e}}} : \mathbf{L}_j^{\text{v}} - T_{e_i} \sum_j^M \frac{\partial \eta_i^c}{\partial \mathbf{A}_j} : \dot{\mathbf{A}}_j}_{\mathcal{H}_i^{\text{in,c}}}, \end{aligned} \tag{4.8}$$

where $c_g = -T \frac{\partial^2 \Psi}{\partial^2 T}$ is the heat capacity of the kinetic subsystem and $\Delta c_i = -T_{e_i} \frac{\partial^2 \Psi}{\partial^2 T_{e_i}}$ are the heat capacities of the configurational subsystems. The $\mathcal{H}^{\text{e}} = \mathcal{H}^{\text{e,k}} + \sum_i^P \mathcal{H}_i^{\text{e,c}}$ is the thermo-elasticity coupling term and $\mathcal{H}^{\text{in}} = \mathcal{H}^{\text{in,k}} + \sum_i^P \mathcal{H}_i^{\text{in,c}}$ is the thermo-inelastic coupling term. The sub-balances also can be combined as,

$$c_g \dot{T} + \sum_i^P \Delta c_i \dot{T}_{e_i} = -\nabla_{\mathbf{X}} \cdot \mathbf{Q} + \mathcal{W}^{\text{int}} + \mathcal{H}^{\text{e}} + \mathcal{H}^{\text{in}} \tag{4.9}$$

Equation (4.8) describes the effects of mechanical rejuvenation, where mechanical deformation drives the evolution of the nonequilibrium structure through the internal inelastic power and thermomechanical coupling. The theory also provides an explanation for the partial conversion of the plastic work under adiabatic conditions to heat as measured by the temperature rise $\dot{T}$. This phenomena is observed for all materials but is particularly pronounced in polymers, where the fraction of plastic work converted to heat can reach

0.4-0.9.[99,172] Equation (4.9) shows that the remainder is diverted to structural evolution through $\dot{T}_{e_i}$.

The second law can be written for the reference configuration as,

$$\dot{\eta} + \nabla_{\mathbf{X}} \cdot \mathbf{H} \geq 0. \tag{4.10}$$

where $\mathbf{H}$ is the entropy flux. Following Kamrin and Bouchbinder,[171] we postulate that:

$$\mathbf{H} = \frac{\mathbf{Q}^k}{T} + \sum_i^P \frac{\mathbf{Q}_i^c}{T_{e_i}}. \tag{4.11}$$

Substituting eq. (4.2) and (4.11) into eq. (4.10), and applying eq.(4.6) to eliminate the heat conduction terms gives,

$$\begin{aligned} &\sum_i^P \left(\frac{1}{T_{e_i}} - \frac{1}{T}\right) Q_i^{kc} - \frac{1}{T^2}\mathbf{Q}^k \cdot \nabla_{\mathbf{X}} T - \sum_i^P \frac{1}{T_{e_i}^2}\mathbf{Q}_i^c \cdot \nabla_{\mathbf{X}} T_{e_i} \\ &+ \frac{1}{T}\mathcal{W}^{\text{int},k} + \sum_i^P \frac{1}{T_{e_i}}\mathcal{W}_i^{\text{int},c} \geq 0. \end{aligned} \tag{4.12}$$

Motivated by the physical observation of heat flow, we require that each term in eq. (4.12) be non-negative to satisfy the second law:

$$\begin{aligned} &-\left(T_{e_i} - T\right) Q_i^{kc} \geq 0, \quad -\frac{1}{T^2}\mathbf{Q}^k \cdot \nabla_{\mathbf{X}} T \geq 0, \\ &-\frac{1}{T_{e_i}^2}\mathbf{Q}_i^c \cdot \nabla_{\mathbf{X}} T_{e_i} \geq 0, \quad \frac{1}{T}\mathcal{W}^{\text{int},k} + \sum_i^P \frac{1}{T_{e_i}}\mathcal{W}_i^{\text{int},c} \geq 0 \end{aligned} \tag{4.13}$$

These provide constraints for constitutive relations for the heat flux and evolution equations for the internal variables $\mathbf{F}_j^{\text{v}}$ and $\mathbf{A}_j$.

4.2.2 Constitutive Models for Amorphous Networks

In the following, we demonstrate using simple constitutive functions the ability of the effective temperature theory to describe the glass transition, physical aging, and mechanical rejuvenation of an amorphous crosslinked network. For moderate deformations, we apply decoupled Neo-Hookean functions for the internal energy and entropy densities,

$$\begin{aligned}\Psi^k &= \sum_j^N \frac{(1-a)\mu_j^{\text{neq}}}{2}\left(\text{tr}\left(\overline{\mathbf{C}}_j^{\text{e}}\right)-3\right)+\frac{\kappa}{4}\left(J^2-2\log J-1\right)+c_g\left(T-T_0\right)-c_gT\ln\frac{T}{T_0},\\ \Psi_i^c &= \frac{\Delta c_i T_{e_i}}{\Delta c T_0}\frac{\mu^{\text{eq}}}{2}\left(\text{tr}\left(\overline{\mathbf{C}}\right)-3\right)+\sum_j^N \frac{a_i\mu_j^{\text{neq}}}{2}\left(\text{tr}\left(\overline{\mathbf{C}}_j^{\text{e}}\right)-3\right)+\Delta c_i\left(T_{e_i}-T_0\right)-\Delta c_i T_{e_i}\ln\frac{T_{e_i}}{T_2},\end{aligned} \tag{4.14}$$

where $J = \det\mathbf{F}$ is the volumetric deformation and $\overline{\mathbf{C}} = J^{-2/3}\mathbf{C}$ and $\overline{\mathbf{C}}_j^{\text{e}} = J_i^{\text{e}-2/3}\mathbf{C}_j^{\text{e}}$ with $J_i^{\text{e}} = \det\mathbf{F}_i^{\text{e}}$ are the isochoric parts of the total and elastic deformation tensors. The parameters κ is the bulk modulus, μ_j^{neq} are the shear moduli of the N inelastic processes, and T_2 is Kauzmann temperature. We have assumed a partitioning of the inelastic internal energy, where $0 \leq 1-a \leq 1$ describes the fraction of the total inelastic internal energy attributed to the kinetic subsystem. To reduce the number of parameters, we also assume that the excess heat capacity Δc and a have the same distribution over the P configurational processes, such that $\Delta c_i = \phi_i \Delta c$ and $a_i = \phi_i a$, where $\sum_i^P \phi_i = 1$. The total free energy density Ψ can be represented as,

$$\begin{aligned}\Psi = &\sum_i^P \frac{\Delta c_i T_{e_i}}{\Delta c T_0}\frac{\mu^{\text{eq}}}{2}\left(\text{tr}\left(\overline{\mathbf{C}}\right)-3\right)+\sum_j^N \frac{\mu_j^{\text{neq}}}{2}\left(\text{tr}\left(\overline{\mathbf{C}}_j^{\text{e}}\right)-3\right)+\frac{\kappa}{4}\left(J^2-2\log J-1\right)\\ &+c_g\left(T-T_0\right)-c_gT\ln\frac{T}{T_0}+\sum_i^P\left(\Delta c_i\left(T_{e_i}-T_0\right)-\Delta c_i T_{e_i}\ln\frac{T_{e_i}}{T_2}\right).\end{aligned} \tag{4.15}$$

When polymer structure is at equilibrium, $T_{e_i} = T$, the above function reduces to the simplest form of Helmholtz free energy density, which is widely adopted in classic thermodynamic theories.[?,174]

The nominal stress response is evaluated from $\mathbf{S} = 2\frac{\partial \Psi}{\partial \mathbf{C}}$ as,

$$\mathbf{S} = \sum_i^P \phi_i \frac{T_{e_i}}{T_0} \mu^{\mathrm{eq}} J^{-2/3} \left(\mathbf{I} - \frac{1}{3} \mathrm{tr}\left(\mathbf{C}\right) \mathbf{C}^{-1} \right) + \sum_j^N \mu_j^{\mathrm{neq}} J_j^{\mathrm{e}-2/3} \mathbf{F}_j^{\mathrm{v}-1} \left(\mathbf{I} - \frac{1}{3} \mathrm{tr}\left(\mathbf{C}_j^{\mathrm{e}}\right) \mathbf{C}_j^{\mathrm{e}-1} \right) \mathbf{F}_j^{\mathrm{v}-T} + \frac{\kappa}{2}(J^2 - 1)\mathbf{C}^{-1}, \tag{4.16}$$

and the Cauchy stress $\sigma = \frac{1}{J}\mathbf{F}\mathbf{S}\mathbf{F}^{\mathrm{T}}$ is the push-forward of $\mathbf{S}$,

$$\sigma = \frac{1}{J} \sum_i^P \phi_i \frac{T_{e_i}}{T_0} \mu^{\mathrm{eq}} \left(\overline{\mathbf{C}} - \frac{1}{3} \mathrm{tr}\left(\overline{\mathbf{C}}\right) \right) + \frac{1}{J} \sum_j^N \mu_j^{\mathrm{neq}} \left(\overline{\mathbf{C}}_j^e - \frac{1}{3} \mathrm{tr}\left(\overline{\mathbf{C}}_j^e\right) \right) + \frac{1}{J} \kappa \left(J^2 - 1 \right). \tag{4.17}$$

The inelastic flow stress is evaluated from $\mathbf{M}_j = \mathbf{C}_j^{\mathrm{e}} 2 \frac{\partial \Psi}{\partial \mathbf{C}_j^{\mathrm{e}}}$, as,

$$\mathbf{M}_j = \mu_j^{\mathrm{neq}} \left(\overline{\mathbf{C}}_j^{\mathrm{e}} - \frac{1}{3} \mathrm{tr}\left(\overline{\mathbf{C}}_j^{\mathrm{e}}\right) \mathbf{I} \right), \tag{4.18}$$

which is symmetric for an isotropic free energy density. Thus the internal power can be written as $\mathcal{W}^{\mathrm{int}} = \sum_j^N \mathbf{M}_j : \mathbf{D}_j^{\mathrm{v}}$, where $\mathbf{D}_j^{\mathrm{v}} = \frac{1}{2}\left[\mathbf{L}_j^{\mathrm{v}} + \mathbf{L}_j^{\mathrm{vT}}\right]$ is the inelastic rate of deformation tensor. We previously developed a flow rule for the inelastic deformation that combines the[39] and[77] theory to describe the dramatic change in the relaxation time through the glass transition and stress-activation of inelastic deformation,[106]

$$\mathbf{D}_j^{\mathrm{v}} = \frac{1}{2\upsilon_j} \mathbf{M}_j, \quad \upsilon_j = \upsilon_j^{ref} \exp\left(\frac{B}{T \sum_i^P \eta_i^c} \right) \frac{V_S S}{RT} \left[\sinh\left(\frac{V_S S}{RT} \right) \right]^{-1}. \tag{4.19}$$

The intrinsic viscosities are required to be positive, $\upsilon_j^{ref} > 0$, to satisfy the dissipation criteria in eq. (4.13). The parameter B is a thermal activation energy and V_S is a mechanical

activation volume. We've assumed that the viscosities depend on the total flow stress, $S = (\sum_j^N \frac{2}{3}\mathbf{M}_j : \mathbf{M}_j)^{1/2}$, rather than the flow stress of each inelastic process. The latter requires introducing a spectrum of activation volumes, which would dramatically increase the number of parameters.

To satisfy the entropy inequality caused by heat flux in eq. (4.13), we adopt a linear relation for the heat flux between the inter-subsystem and Fourier's law for heat flux within the subsystem,[174]

$$Q_i^{kc} = -A_i \left(T_{e_i} - T\right), \quad \mathbf{Q}^k = -k_g \mathbf{C}^{-1} \nabla_{\mathbf{X}} T, \quad \mathbf{Q}_i^c = -\Delta k_i \mathbf{C}^{-1} \nabla_{\mathbf{X}} T_{e_i}, \tag{4.20}$$

where $A_i \geq 0$ is the conductivity between the kinetic and each configurational subsystem, k_g and Δk_i are the corresponding coefficients of thermal conductivity in kinetic subsystem and configurational subsystems.

Combining eq. (4.7), (4.8), (4.14) and (4.20) gives the governing equation for T and T_{e_i},

$$c_g \dot{T} = \nabla_{\mathbf{X}} \cdot \left(k_g \mathbf{C}^{-1} \nabla_{\mathbf{X}} T\right) - \sum_i^P A_i \left(T - T_{e_i}\right) + (1-a) \sum_j^N \mathbf{M}_j : \mathbf{D}_j^{\mathrm{v}} \tag{4.21}$$

$$\Delta c_i \dot{T}_{e_i} = \nabla_{\mathbf{X}} \cdot \left(\Delta k_i \mathbf{C}^{-1} \nabla_{\mathbf{X}} T_{e_i}\right) + A_i \left(T - T_{e_i}\right) + a_i \sum_j^N \mathbf{M}_j : \mathbf{D}_j^{\mathrm{v}} + J^{-2/3} \frac{\phi_i T_{e_i} \mu^{\mathrm{eq}}}{2T_0} \left(\mathbf{I} - \frac{1}{3}\mathrm{tr}\left(\mathbf{C}\right)\mathbf{C}^{-1}\right) : \dot{\mathbf{C}}. \tag{4.22}$$

In the following simulations, we assume isothermal condition, where $\dot{T} = 0$, and neglect

$\nabla_{\mathbf{X}} T_{e_i}$. Eq. (4.22) can be simplified as,

$$\dot{T}_{e_i} = \frac{T - T_{e_i}}{\tau_i} + \underbrace{\frac{a}{\Delta c} \sum_{j}^{N} \mathbf{M}_j : \mathbf{D}_j^{\mathrm{v}}}_{\mathcal{W}_i^{\mathrm{int},c}} + \underbrace{\frac{J^{-2/3} T_{e_i} \mu^{\mathrm{eq}}}{2 \Delta c T_0} \left(\mathbf{I} - \frac{1}{3} \mathrm{tr}\,(\mathbf{C})\, \mathbf{C}^{-1} \right) : \dot{\mathbf{C}}}_{\mathcal{H}_i^{\mathrm{e,c}}}, \quad \tau_i = \tau_i^{ref} \exp\left(\frac{B}{T \sum_i^P \eta_i^c} \right), \tag{4.23}$$

where $\tau_i = \Delta c_i / A_i$ is the structural relaxation time, which we describe using the Adam-Gibbs model.[39]We have assumed that the viscosities υ_j in (4.19) and τ_i share the same dependence on T and structure through the total configurational entropy $\eta^c = \sum_i^P \eta_i^c$. We confirmed this assumption experimentally in a previous work for the acrylate networks used in this study.[106] More generally, τ_i can depend on the entropy of each configurational subsystem, which would permit introduction of a spectrum of activation energies B_i, but this would dramatically increase the number of parameters.

In summary, the inelastic behavior of the polymer network is described by two sets of state variables, a distribution of effective temperatures, T_{e_i}, describing the nonequilibrium configurational structure and characterized by the structural relaxation spectrum (τ_i, ϕ_i), and a distribution of inelastic deformations, $\mathbf{F}_k^{\mathrm{v}}$, characterized by the viscoelastic relaxation spectrum $\left(\upsilon_k, \mu_k^{\mathrm{neq}}\right)$. No additional internal variables are used to describe inelastic behavior.

4.2.3 Experimental Methods

The materials adopted for this study was a tert-butyl acrylate (tBA), poly(ethylene glycol) dimethacrylate (PEGDMA) and di(ethylene glycol) dimethacrylate (DEGDMA) random copolymer crosslinked network, with 10 wt% PEGDMA-DEGDMA (XLS) crosslink

density. In previous work, we performed two sets of experiments to obtain the viscoelastic relaxation and structural relaxation spectra. Specifically, the dynamic frequency sweep tests at different temperatures were adopted to measure the viscoelastic relaxation behaviors. The isothermal volumetric relaxation tests were employed to obtain the structural relaxation spectrum. The synthesis procedures and experimental methods to obtain the parameters were described in detail in Nguyen et al.[78] and Xiao et al.[106] In this work, we performed a DSC experiment to obtain the heat capacity and a series of uniaxial compression experiments to validate the constitutive model.

4.2.3.1 DSC

Differential scanning calorimetry is adopted here to obtain the excess heat capacity. Film specimen of 6 mg is heated from -10°C to 80°C at 10°C/min with a TA Q20 differential scanning calorimeter. The specimen was then cooled to -10°C within 20 minutes. The specimen was heated again from -10°C to 80°C at 10°C/min.

4.2.3.2 Uniaxial compression

To validate the model, we performed uniaxial compression tests on cylindrical specimens with both diameter and length 6 mm. The specimens were first heated to 70°C and held for 30 min to remove the effects of physical aging. The specimens were then either quenched in 20°C water for 5 min or cooled to 20°C at 3°C/min, and annealed for 30 min, 1 day or 14 days in an incubator. The specimens were transferred to an MTS Insight 5

electromechanical testing system, equipped with a temperature chamber set at 20°C, and subjected to two load-unload cycles with different annealing times between each cycle. In the first cycle, the specimen was compressed to 30% engineering strain at 0.001/s or 0.01/s strain rate and unloaded. The compressed specimen was annealed at 20°C for 1 min, 10 min, 1 day or 14 days before being compressed again by an addition 15% engineering strain at 0.001/s or 0.01/s. In addition to 20°C, the specimens were also cooled to 60°C and 40°C at 3°C/min, and annealed for 30 min. The specimens were then compressed to 30% engineering strain at 0.001/s or 0.01/s.

4.3 Parameter Determination

The material parameters for the tBA-co-XLS networks with 10wt% crosslinking agents are listed in Table 4.1. This material has a glass transition temperature around 36°C. For convenience, we first rewrite the Adam-Gibbs model at T_g.

The explicit form of the configurational entropy can be calculated by substituting the Helmholtz free energy density in eq. (4.14) into $\eta_i^c = -\frac{\partial \Psi}{\partial T_{e_i}}$,

$$\eta^c\left(T_{e_i}, \mathbf{C}\right) = \sum_i^P \eta_i^c = \sum_i^P \left(\Delta c_i \ln \frac{T_{e_i}}{T_2} - \frac{\Delta c_i}{\Delta c T_0} \frac{\mu^{eq}}{2}\left(\mathrm{tr}\left(\overline{\mathbf{C}}\right) - 3\right)\right) \tag{4.24}$$

The characteristic viscosity and structural relaxation time at T_g are defined as,

$$\begin{aligned} \upsilon_j^g &= \upsilon_j^{ref} \exp\left(\frac{B}{T\eta^c\left(T_g, \mathbf{I}\right)}\right), j = 1:N, \\ \tau_i^g &= \tau_i^{ref} \exp\left(\frac{B}{T\eta^c\left(T_g, \mathbf{I}\right)}\right), i = 1:P. \end{aligned} \tag{4.25}$$

Table 4.1: Parameters of the constitutive model for the polymer-solvent system.

Parameter	**Values**	**Physical significance**
μ^{eq} (MPa)	0.53	equilibrium shear modulus
κ (MPa)	1333.3	bulk modulus
$V_S(cm^3/mol)$	897.5	activation volumen for viscous flow
$B(J/g)$	258.1	thermal activation energy
$T_2(K)$	276.5	Kauzmann temperature
$T_g(K)$	309	glass transition temperature
$T_0(K)$	348	reference temperature
c_g (J/(gK))	1.2	heat capacity of kinetic subsystem
Δc (J/(gK))	0.25	excess heat capacity of configurational subsystems

Combing the above equation with eq. (4.19) and (4.23) yields the viscosity and structural relaxation time at any arbitrary temperature T, effective temperature T_{e_i} and deformation as,

$$\begin{aligned} \upsilon_j &= \upsilon_j^g \exp\left(\frac{B}{T\eta^c\left(T_{e_i}, \mathbf{C}\right)} - \frac{B}{T\eta^c\left(T_g, \mathbf{I}\right)}\right) \frac{V_S S}{RT}\left[\sinh\left(\frac{V_S S}{RT}\right)\right]^{-1}, \\ \tau_i &= \tau_i^g \exp\left(\frac{B}{T\eta^c\left(T_{e_i}, \mathbf{C}\right)} - \frac{B}{T\eta^c\left(T_g, \mathbf{I}\right)}\right). \end{aligned} \tag{4.26}$$

In addition to viscoelastic spectrum $\left(\upsilon_j^g, \mu_j^{\text{neq}}\right)$ and structural relaxation spectrum $\left(\tau_i^g, \phi_i\right)$, the following parameters also need to be determined: T_2, B, μ^{eq}, κ, V_S, Δc and a.

The discrete viscoelasticity spectrum $\left(\upsilon_j^g, \mu_j^{\text{neq}}\right)$, equilibrium modulus μ^{eq} and bulk modulus κ were determined from the master curve of the storage modulus, measured for small strains near the T_g using a substitute continuous relaxation spectrum model.[106,131] The parameter B and Kauzmann temperature T_2 were determined from the temperature dependence of the shift factor used to generate the mater curve of the storage modulus. The structural relaxation spectrum $\left(\tau_i^g, \phi_i\right)$ was determined from the master curve of the unconstrained (stress-free) volume recovery response to a sudden temperature change.[79,106] We've assumed that same distribution of structural relaxation times can be used to describe enthalpy and volume recovery. The activation volume V_S was fit to the difference in the yield strength measured at two strain rate 0.01/s and 0.001/s at $T = 20°\text{C}$. DSC experiments were used to determine the excess heat capacity Δc of configurational subsystems and heat capacity of the kinetic subsystem c_g (Fig. 4.1). The heat capacity has a slight temperature dependence. For simplicity, we assumed a constant value for heat capacity. The

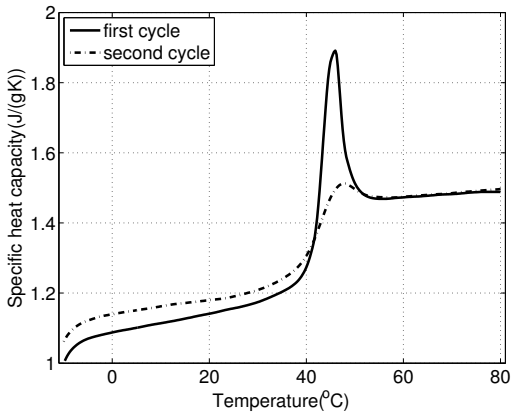

Figure 4.1: DSC scan of the undeformed specimens

remaining parameter a controls the rate of strain softening. We assumed $a = 0.5$ for simplicity. The viscoelastic and structural relaxation spectrums at glass transition temperature T_g are plotted in Fig. 4.2.

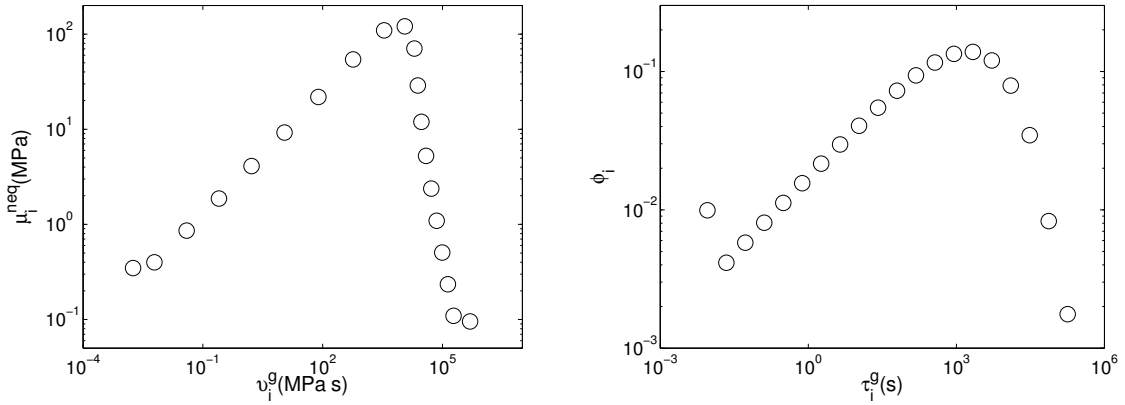

(a) (b)

Figure 4.2: Relaxation spectrum of of tBA-co-XLS networks with 10 wt% crosslinker (a)viscoelastic spectrum, (b) structural relaxation spectrum

We choose $N = 20$ and $P = 20$ to accurately represent both stress and structural re-

laxation spectrums. The choice of the number of effective temperatures P and internal inelastic deformation N is a trade-off between accuracy and computational cost. We performed a parameter study that evaluated the error associated with the choice of N and P. Results showed that decreasing the number of discrete processes to $N = 12$ and $P = 12$ did not significantly increase the error. A further reduction would result a non-smooth fit to the whole region of master curve. The number of relaxation processes for viscoelastic relaxation and structural relaxation do not need to be set as equal. Currently we are implementing the model into finite element code to simulate the inhomogeneous thermal and mechanical conditions involving large number of elements which may require developing an efficient algorithm to reduce the number of internal variables.

4.4 Results and Discussions

To validate the model, we performed uniaxial compression tests on cylindrical specimens of the tBA-co-PEGDMA material with 10 wt% cross-linker density and $T_g = 36°C$.[106] The specimens were first heated to 70 ^{o}C and held for 30 minutes to remove the effects of the physical aging. The specimens were then either quenched in 20 ^{o}C water for 5 minutes or cooled to 20 ^{o}C at 3 ^{o}C/min, and annealed for 30 minutes, 1 day or 14 days in an incubator. The specimens were transferred to an MTS electromechanical testing system, equipped with a temperature chamber set at 20 ^{o}C, and subjected to two load-unload cycles with different annealing times between each cycle. In the first cycle, the specimen was

compressed to 30% engineering strain at 0.001/s strain rate and unloaded. The compressed specimen was annealed at 20 ^{o}C for 1 minute, 10 minutes, 1 day or 14 days before being compressed again by an addition 15% engineering strain at 0.001/strain. In addition to 20 ^{o}C, the specimens were also cooled to 60 ^{o}C and 40 ^{o}C at 3 ^{o}C/min, and annealed for 30 minutes. The specimens were then compressed to 30 % engineering strain at 0.001/s or 0.01/s.

Figure 4.3 plots the uniaxial compression response at different temperatures spanning the glass transition for strain rates 0.01/s and 0.001/s. The model was able to capture the transition from a rubbery viscoelastic response to a glassy viscoplastic response, characterized by a yield peak and dynamic softening, with decreasing temperature. Moreover, it accurately described the effect of strain rate on the temperature-dependent stress response through the glass transition.

Figure 4.4 compares experimental and simulation results for the uniaxial compression response for two consecutive load-unload cycles for different annealing times before the first loading and 1 minute annealing time before the second loading. The yield strength of the first compression response increased with the prior annealing time, while the steady state flow stress was independent of the annealing time. The stress response of the second compression all collapsed onto a single curve, which indicated that the large inelastic deformation of the prior loading erased the thermal history. Figure 4.5 plots the experimental and simulation results of specimens annealed at different time before the second compression. The yield strength increased with annealing time, indicating renewed physical aging

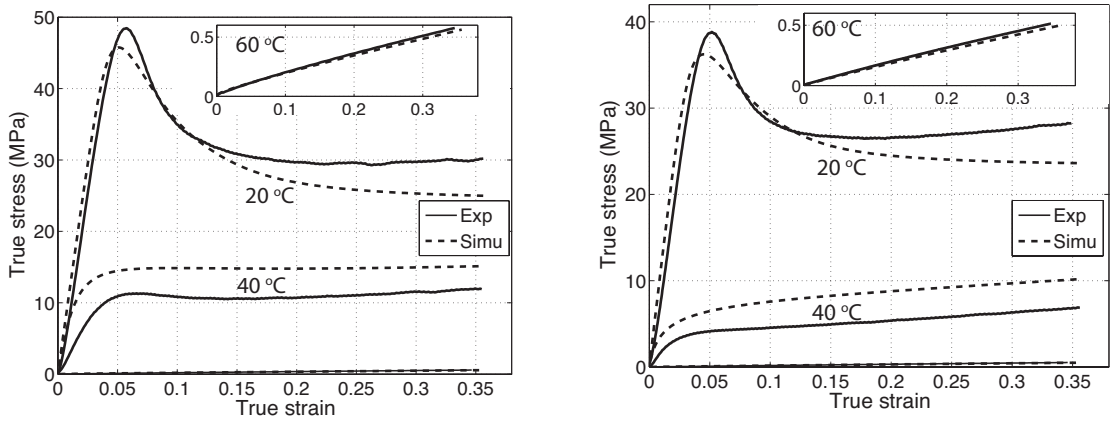

Figure 4.3: Uniaxial compression response of tBA-co-PEGDMA with 10 wt% crosslinker at different temperatures spanning the glass transition region for applied engineering strain rates (a) 0.01/s and (b) 0.001/s.

after cessation of deformation. The experimental and modeling predictions of the yield strength of the first and second uniaxial compression response agreed well for different prior annealing times. The model also accurately predicted the strain recovery during the second annealing period. Figure 4.6 compares the yield strength of the first and second uniaxial compression response for different prior annealing times. The results demonstrated good agreement between experiments and simulation.The largest discrepancy occurred for second compression cycle with a prior 1 minute annealing time, where the yield strength predicted by the model was 6 MPa smaller than measured by experiments. We believed that the discrepancy occurred because the model did not take into account the effect of orientation hardening, which was evident in the experiments after 20% strain.

Finally, we simulated the DSC response of quenched and annealed (30 minutes) speci-

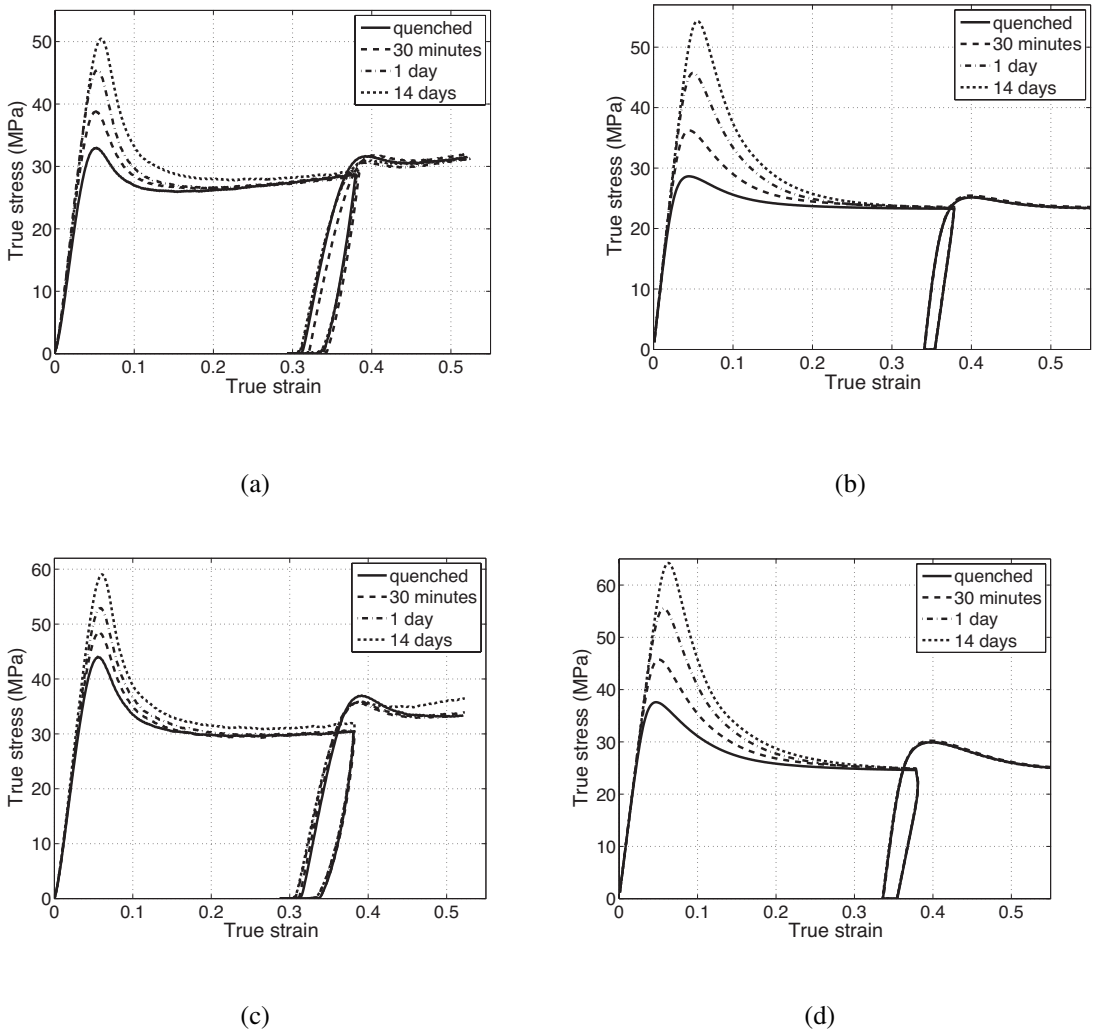

Figure 4.4: Uniaxial compression response of tBA-co-XLS networks with 10 wt% crosslinker for two load-unload cycles and different annealing times prior to the first cycle and 1 min annealing time prior to the second cycle, comparing (a) 0.001/s experiments, (b) 0.001/s simulations, (c) 0.01/s experiments and (d) 0.01/s simulations.

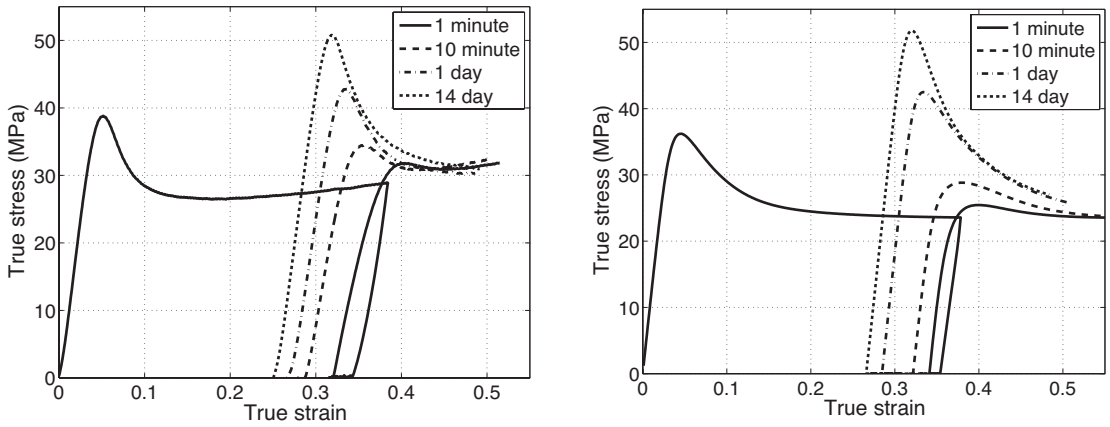

(a) (b)

Figure 4.5: Uniaxial compression response of tBA-co-PEGDMA with 10 wt% crosslinker for two load-unload cycles at 0.001/s strain rate and 30 minutes annealing times prior to the first cycle and different annealing time prior to the second cycle, comparing (a) experiments and (b) simulations.

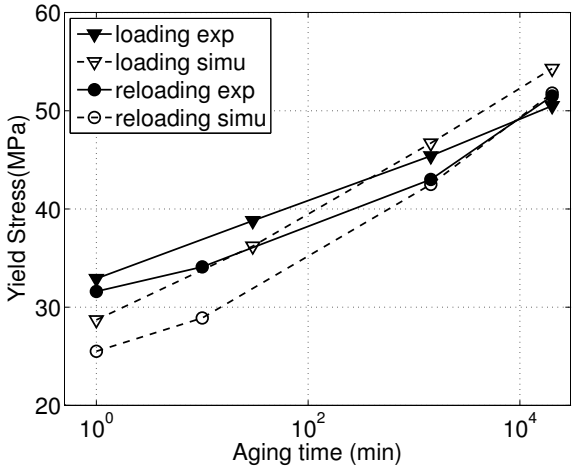

Figure 4.6: Yield strength of the uniaxial compression response for different prior annealing time

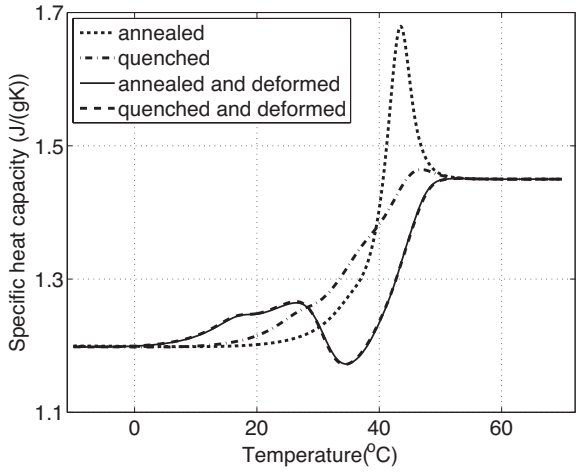

Figure 4.7: Simulation results of DSC for annealed and quenched specimens before and after deformation

mens before and after 30% compression. Results for the enthalpy change with temperature for all cases shown in Fig. 4.7 captured the features of physical aging and mechanical rejuvenation reported by experiments for amorphous polymers.[29] Prior to plastic deformation, annealing caused the appearance of an endothermic overshoot T_g. This feature was absent from the quenched condition. Plastic deformation by 30% compression erased the effects created by the prior thermal history, resulting in identical DSC curves for the quenched and annealed conditions. Moreover plastic deformation removed the endothermic overshoot after T_g and created an exothermic undershoot before T_g.

We have developed a coupled thermomechanical model for the nonequilibrium behavior of amorphous materials, that strongly couples structural evolution and inelastic deformation. The material structure is described conceptually as configurational degrees of freedom, characterized by a distribution of effective temperatures, trapped in a nonequi-

librium state by slow molecular motions. The evolution of the configurational subsystems towards a less mobile state brings about the tremendous increase in the stiffness of the glass transition and the appearance of yielding and plastic deformation. The yield strength for a particular temperature and strain rate is determined by the nonequilibrium structure; thus longer annealing times result in more resistance to plastic flow and higher yield strengths. The internal plastic work in turn drives the configurational subsystems towards a more mobile state, and produces the post-yield strain-softening behavior typical of glassy polymers. The theory predicts the appearance of a steady-state flow stress from the balance of internal plastic work and heat conduction between the kinetic and configurational subsystems. In previous constitutive developments, this phenomena was described as an evolution of the yield strength s_y with the plastic strain rate to a steady-state value.[106,149] This resulted in a steady-state flow stress that depends on the thermal history, which is contrary to experimental observations.

We have made a number of strong assumptions in applying the thermomechanical theory to the tBA-co-PEGDMA random copolymer network. The relaxation time and the viscosity of each structural and stress relaxation process were assumed to have the same dependence on the temperature and the total configurational entropy. Moreover, we assumed that the distribution of configurational properties, such as the heat capacity Δc and fraction of stored plastic work a, were identical. These assumptions minimized the number of model parameters and facilitated parameter determination from experiments. Comparing the simulation and experimental results for the uniaxial compression tests showed that

the assumptions were appropriate for tBA-co-PEGDMA. However, more work is needed to validate the modeling assumptions for other amorphous materials and for applications far below the glass transition temperature. We are currently investigating the ability of the model and model parameters determined from thermomechanical experiments to predict the effect of deformation and temperature history on the enthalpy (e.g, Fig. 4) and other physical properties. The results will provide further insight on the thermodynamic nature of the effective temperatures and limitations of the current modeling framework. We also plan to investigate the ability of the model to capture the effect of structural evolution on the heat generation at different strain rates and the effect of effective temperature diffusion on the development of heterogeneous strain fields and strain localization.

In conclusion, we have developed a thermodynamically consistent theory for coupling structural evolution and inelastic deformation for amorphous polymers. We have shown that with the appropriate constitutive relations for the temperature-dependence and structure-dependence of the viscosities governing inelastic flow and structural relaxation times, the effective temperature theory can capture a wide variety of nonequilibrium behaviors. The theory has the practical benefit of dramatically reducing the number of model parameters. We were able to use the same stress and structural relaxation spectrum and activation energies to reproduce the rate-dependence and time-dependence of the high temperature viscoelastic behavior, low temperature viscoplastic behavior, physical aging, and mechanical rejuvenation for an acrylate network. This provides an efficient predictive modeling tool for applications spanning a large temperature range, such as for material processing

and shape memory behavior, long times, and dynamic events.

Chapter 5

Conclusions and Future Work

This work has developed constitutive models to describe the thermomechanics and shape memory performance of amorphous polymers spanning the glass transition. The models incorporate stress relaxation, structural relaxation, mechanical rejuvenation, and plasticization effect. The models capture all the main characteristics of amorphous polymers over a wide temperature region, including the entropy-driven hyperelasticity above the glass transition region, the time and temperature dependent viscoelastic behaviors in the glass transition region, and the viscoplastic performance with yielding and strain softening below the glass transition region. These models have shown the ability to describe the thermally-activated and solvent-driven shape memory behaviors. To characterize the polymers, both thermomechanical experiments and shape memory recovery experiments were performed. Experiments were also developed to obtain the model parameters.

5.1 Summary of this Work

Chapter 2 developed a constitutive model for the thermally-activated shape memory effect. The model employed multiple discrete relaxation processes for stress relaxation, structural relaxation and stress-activated viscous flow. The model parameters were obtained through the dynamic frequency sweep tests, isothermal volumetric recovery tests and uniaxial compression tests. The model was applied to study the influence of deformation temperature on the partial constraint recovery and fixed-strain recovery tests. The simulation results accurately predicted the recovery region and recovery ratio of the partially constraint recovery tests as shown in experiments. The model also captures the strain overshoot of specimens programmed below T_g, which is caused by the distribution of relaxation times. For fixed-strain recovery experiments, the simulations show the specimens programmed below T_G exhibit significantly larger stress overshoot than specimens programmed above T_g, which is consistent with experimental observations. The stress overshoot is caused by the mechanical strain recovery for cold-programmed samples. In contrast, the stress overshoot for hot-programmed specimens is caused by the constrained thermal expansion, which is significantly smaller than the viscoelastic strain recovery.

In Chapter 3, a constitutive model was developed to investigate the influence of low solvent concentration on the mechanical properties and shape memory performance. The Adam-Gibbs model was extended to describe the decrease in the relaxation time due to the increase in configurational entropy through mixing. The diffusion process was also incorporated into the model. The constitutive model was implemented for finite element

analysis. A staggered iterative scheme was applied to solve the mechanical and diffusion problems. To verify the model, an acrylate-based copolymer was synthesized. The diffusion tests and frequency tests of dry and saturated specimens were employed to obtain the model parameters. The model with the obtained parameter is able to predict the transition from the viscoplastic stress response of dry specimens to the viscoelastic response of saturated specimens in the uniaxial tension tests. The simulation results on the shape recovery of film specimens and tube specimens in water also show good agreement with the experimental observations. From this it was concluded that the solvent-driven shape memory recovery is caused by the plasticization effect of solvents.

In order to describe the strain softening behaviors, the models in Chapter 2 and 3, adopted a phenomenological evolution equation of the yield strength to a steady-state value with plastic strain rate. This results in a steady-state flow stress that depends on the thermal history, which contradicts experimental observations. These models can not be directly employed to explain the mechanical rejuvenation phenomena. In Chapter 4, a thermomechanical model that couples structural evolution and inelastic deformation was developed to describe both physical aging and mechanical rejuvenation. The polymers are assumed to be composed of the fast relaxation kinetic subsystem which is always in equilibrium and slow relaxation configurational subsystems which fall out to the equilibrium at low temperatures. Physical aging is caused by the structural evolution of configurational subsystems towards a less mobile state, while the mechanical rejuvenation is caused by the internal plastic work that drives the configurational subsystems towards a more mobile state. The

model is verified by the measured stress-strain response of samples at different temperatures, strain rate, aging time and pre-deformation. The model can also describe the enthalpy change of specimens with different thermal history and mechanical deformation. The simulation shows that the physical aging can result in an endothermic overshoot and that large elastic work can erase the appearance of the endothermic overshoot and create another exothermic undershoot, which are all observed in experiments. This model shows the possibility of providing a unified theory with a minimum set of parameters for a wide range of nonequilibrium behaviors, that are typically treated as separate phenomena in current modeling approaches.

The model developed in the Chapter 4 studies the general physical properties and mechanical response of amorphous polymers. It can also be applied to model the thermal and solvent-driven shape memory effect. For the partially constraint recovery tests of specimens programmed blow T_g, the model in Chapter 2 predicted a 5-10^{o}C higher activation temperature and a larger strain overshoot. By introducing the coupling between structural evolution and inelastic deformation, the model in Chapter 4 can improve the prediction of the shape memory recovery performance of cold deformation specimens. The coupled thermal-mechanical model can also be implemented into finite element code to incorporate the heat conduction in the specimen and heat flux between the specimen and environment.

5.2 Key Contributions to Polymer Physics

The work includes the following contributes to the fundamental understanding of the polymer physics,

1. **A detailed experimental method was developed for obtaining the structural relaxation spectrum.** The broad distribution nature of the structural relaxation processes makes it difficult to obtain the spectrum in one single test. Thus the consecutively isothermal volumetric recovery tests were designed to obtain the structural relaxation spectrum. The relaxation tests at high temperatures provide the information for relaxation processes with large relaxation time, while the relaxation tests at low temperatures provide the information for relaxation processes with small relaxation time. This method can also be applied to obtain the structural relaxation spectrum corresponding to changes in pressure.

2. **The stress and structural relaxation time can be described by the same temperature and structure dependence shift factor for the acrylate random copolymer system.** It was demonstrated the individual volumetric relaxation test can be shifted to form a master curve through adopting the same shift factor from the viscoelastic relaxation tests. The shift factor for the stress relaxation can be obtained through the standard time-temperature superposition of small strain viscolelastic tests. In contrast, the shift factor of structural relaxation is difficult to obtain from standard tests. This finding shows that the shift factor for both relaxation processes can be obtained

through one single test.

3. **Solvent-driven shape memory effect originates from the plasticization effect.** In this work, the configurational entropy theory was adopted to describe the depression of the glass transition temperature by solvent introduced plasticization effect. The model parameters were obtained through superposition of the storage modulus of saturated specimens to the master curve of the storage modulus of the dry specimens. This approach can be extended for other theories (free volume, for example) to simulate the shape memory recovery in solvents.

4. **Physical aging and mechanical rejuvenation can be described by one single set of parameters for the acrylate random copolymer system.** This work provides a unified framework to model the influence of thermal history and mechanical deformation on the stress-strain and enthalpy response, which is important for the applications of amorphous polymers as structural materials. The work also shows that the origin of strain softening is structural rejuvenation.

5.3 Limitations of this Work

Though these models have achieved considerable success in describing the shape memory performance of amorphous polymers and the general thermomechanical behaviors of amorphous polymers, some limitations of these models should be acknowledged. First, the current models are limited to moderate strains (less than 30%). In the rubbery state,

the Arruda-Boyce eight chain model is able to describe the stress strain response over a wide strain region. However, the Arruda-Boyce model is inadequate to capture the temperature and strain rate dependent strain hardening behaviors below T_g, which shows strain hardening modulus increases with decreasing temperature and increasing strain rate. The model developed in the Chapter 3 adopted the modified Adam-Gibbs model to incorporate the solvent effect into the model by assuming the solvent does not influence the configurational entropy of the dry polymer systems. This assumption may only be valid for the polymer-solvent systems with limited swelling ability. Thus the model can not be applied to investigate the shape memory recovery of polymers in organic solvent, which involves large solvent concentration. The diffusion of the solvent in the polymer systems is modeled by the Fick's law, which may also fail to explain the diffusion behaviors of organic solvent in amorphous polymers. For the model developed in Chapter 4, it is assumed that a constant fraction of viscous dissipation flows into the configurational subsystems. This assumption needs to be verified over a wide range of strain rate and temperature.

5.4 Future Directions

Future directions include further improvement on the current models and the applications of the models to describe new experimental observations. The main future directions are listed as following,

1. The current work can be extended for thermoplastic amorphous polymers. The work

mainly focuses on the amorphous thermoset with chemically cross-linked networks. Compared with the structures of thermosets which are formed through strong chemical bonds, the polymer chains of thermoplastic associate through the intermolecular forces. Thus at high temperatures the thermoplastic can be reshaped. When thermoplastic is adopted as shape memory polymers, the recovery performance is accompanied by some unrecoverable strain. The model developed in Chapter 2 can be modified to model the shape memory behaviors of the thermoplastic amorphous polymers, including the influence of deformation temperature, holding time, and cyclic tests on the shape memory performance.

2. The plasticization model developed in Chapter 2 can be improved to describe high solvent concentration. The dependence of the relaxation time on large solvent concentration needs to be defined through general polymer solution theories and verified through the experimentally measured dynamic response of polymers with various degrees of solvent concentration. A fully coupled chemo-mechanical model can also be developed. The energy change from mixing polymer and solvent needs to be incorporated into the total free energy, and the diffusion equation for the solvent species needs to be derived from thermodynamics. The model can be further extended to describe the mechanical behaviors of the gels. Most of current gel models assume the dry gels are in their rubbery state. But various gels are in the stiff glassy state at room temperature. As gels swell, the solvent decreases their viscosity. Thus the viscoelastic and viscoplastic effect needs to be included to fully describe the complex

swelling and deformation behaviors of gels.

3. The structural relaxation spectrum in this study is obtained through isothermal volumetric relaxation tests. In Chapter 4, the enthalpy structural relaxation spectrum is assumed to have the same shape as the volumetric relaxation spectrum. New experimental procedures need to be designed to obtain the enthalpy structural relaxation spectrum from DSC data. The constitutive model developed in Chapter 4 together with new obtained structural relaxation spectrum can be applied to study the enthalpy measurements of amorphous polymers with different thermal history (cooling rate, aging time) and mechanical deformation (strain).

4. The model developed in Chapter 4 can be applied to simulate the thermomechanical coupling of glassy amorphous polymers. The model needs to be implemented into finite element program by writing a user-defined element subroutine. In Appendix B, the detailed procedure of implementation is provided. The model can then be applied to study the influence of strain rate and thermal history on heat generation. The in situ surface temperature measurement tests need to be performed by an infrared camera to verify the model. The model can also be employed to study the strain localization behaviors of amorphous polymers due to inhomogeneous in geometry and thermal history .

5. Strain hardening can be incorporated into the thermomechanical models. The nonequilibrium thermodynamic framework developed in Chapter 4 can be extended to incor-

porate the strain hardening effect. Internal parameters will be defined to describe the chain orientation. The evolution equations will be derived based on thermodynamics. The model can be applied to study the influence of temperature, strain rate and pre-deformation on the strain hardening behaviors. The model can also be employed to investigate the shape memory behaviors of samples programmed with large strain below T_g.

Appendix A

Modeling Multiple Shape Memory and Temperature Memory Effects in Amorphous Polymers

This appendix has been reprinted from R. Xiao, J. Guo and T. Nguyen, "Modeling the multiple shape memory effect and temperature memory effect in amorphous polymers ", RSC Advances, 2015, 5, Pages 416-423, with permission from The Royal Society of Chemistry.[173]

In the previous chapter, we investigated the shape memory behaviors of acrylate-based polymers. These polymers exhibit a glass transition region spanning 15^{o}C-30^{o}C. The fractional damping model was adopted to obtain the relaxation spectrum with reasonable accuracy. For polymers with extreme broad glass transition region, the fractional damping

model was not able to accurately fit the master curve. Thus an alternative method needs to be developed to obtain the relaxation spectrum. In this appendix, we presented a method for measuring the broad relaxation spectrum of Nafion, which has a glass transition spanning from 50^{o}C to140^{o}C. We applied a finite deformation, nonlinear viscoelastic model with the obtained spectrum to study the multiple shape memory effect and temperature memory effect of Nafion.

A.1 Methods

Nafion® PFSA membrane with equivalent molecular weight 1100 was purchased (Dupont, Wilmington, DE, USA) and cut into strips of dimensions 15 mm×5 mm×0.25 mm for dynamic mechanical analysis (DMA) measurements described below. Prior to the DMA measurements, the specimens were annealed for 30 minutes at 160°C to remove the water in the specimens.

A.1.1 Material Characterization

A.1.1.1 Stress Relaxation:

Stress relaxation experiments were performed using the DMA Q800 (TA Instruments, New Castle, DE, USA). The Nafion strips were equilibrated at 190^{o}C for 15 minutes and then cooled to 40^{o}C in 6°C increments. The specimens were equilibrated at each test tem-

perature for 15 minutes, then subjected to a 0.4% strain and held for 20 minutes for stress relaxation. The relaxation modulus as a function of time was measured at each temperature and then shifted to the reference temperature, $T_0 = 160^oC$, using the method described in Ferry.[27] This procedure provided a master curve of relaxation modulus, which was used to determine the parameters of the viscoelastic relaxation spectrum and the temperature-dependence shift factor $a(T)$.

A.1.1.2 Dynamic Temperature Sweep:

The dynamic temperature sweep test was used to measure the temperature dependent storage modulus, loss modulus and tanδ of the Nafion strips. The specimen was equilibrated at 20^{o}C for 20 minutes and then heated to 180^{o}C at 1^{o}C/min. A 0.4% dynamic strain applied at 1 Hz at each temperature to measure the dynamic mechanical properties.

A.1.2 Shape Recovery Experiments

A.1.2.1 Temperature Memory:

The DMA Q800 was also used to measure free recovery response of Nafion strips programmed at different deformation temperatures, 155^{o}C, 120^{o}C and 85^{o}C. The specimens were equilibrated at the deformation temperature for 15 minutes, then stretched to 50% engineering strain in two minutes. The specimens were cooled to 40^{o}C at 3^{o}C/min at constant strain and held isothermally for 5 minutes to fix the temporary shape before unloading. To

recover the permanent shape, the strips were heated to 180°C at 1°C /min. The displacement of the strips were measured using the zero force mode of the Q800. We chose a relative low cooling and heating rate to reduce the influence of heat conduction on the shape memory performance.

A.1.2.2 Multi-staged Shape Recovery:

To investigate the influence of the recovery temperature, the specimens were stretched to 80% engineering strain at 155°C and cooled to 40°C. To recover the permanent shape, the specimens were heated in discrete steps at 3°C /min. The temperature steps were 40°C, 100°C, 120°C, 140°C and 160°C. The specimens were held for 20 minutes at each step and the displacement was measured under zero force mode.

A.1.2.3 Dual Programming Shape Recovery:

We performed a two-step shape memory programming test. The specimen was equilibrated at 155°C (the first programming temperature) for 15 minutes and stretched to 40% engineering strain. The specimen was cooled to 120°C (the second programming temperature) at $3^oC/min$ and held for 5 minutes at isostrain condition. The specimen was then stretched another 40% engineering strain before cooling to 40°C at $3^oC/min$ to fix the temporary shape. To recover the permanent shape, the specimens were heated to 170°C at 1°C/min under zero force mode. The experiment investigated two additional sets of programming temperatures: (155°C, 85°C) and (120°C, 85°C).

A.2 Numerical Modeling

A.2.1 Constitutive Modeling

A finite deformation, nonlinear viscoelastic model with multiple parallel relaxation mechanisms was used to describe the shape memory behavior of Nafion. The deformation gradient $\mathbf{F}$ is defined to map a point in the reference undeformed configuration to a point in the current deformed configuration. To describe viscoelasticity, the deformation gradient is multiplicatively decomposed into elastic and viscous parts as: $\mathbf{F} = \mathbf{F}_i^{\mathrm{e}}\mathbf{F}_i^{\mathrm{v}}, i = 1 : N$. The total and elastic left Cauchy-Green deformation tensors are defined as $\mathbf{b} = \mathbf{F}\mathbf{F}^{\mathrm{T}}$ and $\mathbf{b}_i^{\mathrm{e}} = \mathbf{F}_i^{\mathrm{e}}\mathbf{F}_i^{\mathrm{eT}}$. To represent the inherent difference in the time-dependent behavior of the volumetric and deviatoric response, we also split the deformation into the distortional and volumetric parts as: $\overline{\mathbf{b}} = J^{-2/3}\mathbf{b}$ and $\overline{\mathbf{b}}_i^{\mathrm{e}} = J^{\mathrm{e}-2/3}\mathbf{b}_i^{\mathrm{e}}$, where $J = \det(\mathbf{F})$ and $J_i^{\mathrm{e}} = \det\left(\mathbf{F}_i^{\mathrm{e}}\right)$ are the total and elastic part of the volumetric deformation ratio.

The Cauchy stress response σ is described as the sum of a time-independent equilibrium distortional component, N time-dependent nonequilibrium distortional components, and a time-independent volumetric component:

$$\sigma = \underbrace{\frac{1}{J}G^{\mathrm{eq}}\left(\overline{\mathbf{b}} - \frac{1}{3}\mathrm{tr}\left(\overline{\mathbf{b}}\right)\right)}_{\mathbf{s}^{\mathrm{eq}}} + \underbrace{\sum_i^N \frac{1}{J}G_i^{\mathrm{neq}}\left(\overline{\mathbf{b}}_i^{\mathrm{e}} - \frac{1}{3}\mathrm{tr}\left(\overline{\mathbf{b}}_i^{\mathrm{e}}\right)\right)}_{\mathbf{s}^{\mathrm{neq}}} + \underbrace{\frac{1}{2J}\kappa\left(J^2-1\right)}_{p}\mathbf{1}, \tag{A.1}$$

where G^{eq} is the equilibrium shear modulus, G_i^{neq} are the nonequilibrium shear moduli and κ is the bulk modulus.

The following nonlinear evolution equation is adopted for the internal strains $\mathbf{b}_i^{\mathrm{e}}$,[127]

$$-\frac{1}{2}\mathcal{L}_v\mathbf{b}_i^e\mathbf{b}_i^{\mathrm{e}\text{-}1} = \frac{\mathbf{s}_i^{\mathrm{neq}}}{2\upsilon_i^{\mathrm{ref}}\mathrm{a}(T)} \tag{A.2}$$

where $\check{\mathrm{c}}_{\mathrm{v}}\mathbf{b}_i^{\mathrm{e}} = \mathbf{F}\overline{\left(\mathbf{F}_i^{\mathrm{v}\mathrm{T}}\mathbf{F}_i^{\mathrm{v}}\right)^{-1}}\mathbf{F}^{\mathrm{T}}$ and $\mathcal{L}_v$ is the Lie time derivative.[174] The parameter $\upsilon_i^{\mathrm{ref}}$ is the shear viscosity at the reference temperature and a (T) is the temperature-dependent shift factor. The stress relaxation time is related with the shear viscosity as $\tau_i^{\mathrm{ref}} = \upsilon_i^{\mathrm{ref}}/G_i^{\mathrm{neq}}$.

A.2.2 Parameter Determination

As described in Sec. A.1.1.1, the master curve of the relaxation modulus was obtained as shown in Fig. A.1(a). Linearizing the viscoelastic model to small strain, the uniaxial tension stress relaxation modulus at the reference temperature can be expressed as,

$$E(t) = E^{\mathrm{eq}} + \sum_i^N E_i^{\mathrm{neq}} \exp\left(-\frac{t}{\tau_i^{\mathrm{ref}}}\right) \tag{A.3}$$

where E^{eq} is the equilibrium Young's modulus and E_i^{neq} are the nonequilibrium Young's moduli. Because the master curve is extremely broad, it is difficult to fit eq. (A.3) directly to the master curve of the relaxation modulus to obtain the relaxation spectrum $\left(\tau_i^{\mathrm{ref}}, E_i^{\mathrm{neq}}\right)$. Instead, we first evaluated a continuous relaxation spectrum $h(\tau)$ from the master curve,[27]

$$E(t) = \int_{-\infty}^{\infty} h(\tau)\exp\left(-\frac{t}{\tau}\right) d\ln\tau. \tag{A.4}$$

According to Schwarzl and Staverman,[?] the continuous relaxation spectrum can be calculated using the following second order accurate approximation method,

APPENDIX A. MODELING MULTIPLE SHAPE MEMORY AND TEMPERATURE MEMORY EFFECTS IN AMORPHOUS POLYMERS

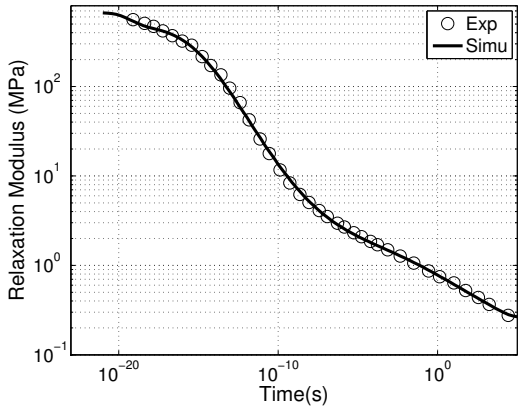

(a)

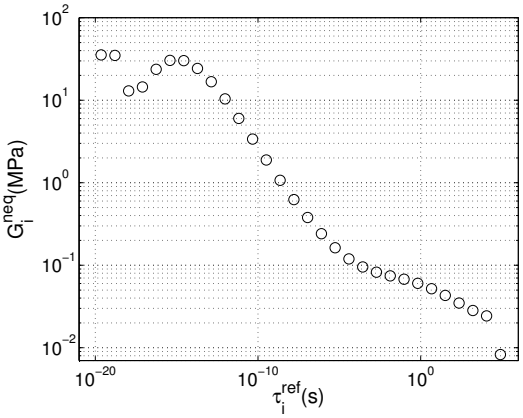

(b)

Figure A.1: Characterizing the stress relaxation behavior of Nafion: (a) master curve of the relaxation moduli, and (b) the discrete stress relaxation spectrum

$$h(\tau) = -E(t)\left[\frac{d\left(\log E\right)}{d\left(\log t\right)} - \left(\frac{d\left(\log E\right)}{d\left(\log t\right)}\right)^2 - \frac{1}{\ln\left(10\right)}\frac{d^2\left(\log E\right)}{d\left(\log t\right)^2}\right]_{t=2\tau}. \tag{A.5}$$

To evaluate eq. (A.5) for $h(\tau)$, we expressed $\log E$ as a function of $\log t$ by fitting a 7th order polynomial to the master master curve of the relaxation modulus plotted on a log-log scale. We next evaluated the continuous cumulative relaxation spectrum as,

$$H(\tau) = \int_{\ln\tau}^{\infty} h\left(z\right) d\left(\ln\left(z\right)\right) \tag{A.6}$$

The discreet cumulative relaxation spectrum was evaluated by combining eq. (A.3), (A.4) and (A.6) as,

$$H_{\text{disc}}(\tau) = E^{\text{eq}} + \sum_{i}^{N} E_i^{\text{neq}} \left\langle \tau - \tau_i^{ref} \right\rangle \tag{A.7}$$

where $\left\langle \tau - \tau_i^{ref} \right\rangle = 1$ for $\tau < \tau_i^{ref}$.

We next assumed a power law distribution of the relaxation times at the reference temperature as,[78]

$$\tau_i^{\text{ref}} = \tau_{\max}\left(\frac{\tau_{\max}}{\tau_{\min}}\right)^{\frac{i-1}{N-1}}, \tag{A.8}$$

where $\tau_{\max}$ and $\tau_{\min}$ are the maximum and minimum relaxation time chosen based on the relaxation region and N is the number of relaxation processes. The choice of N is a trade off between accuracy and computational cost. Haupt et al.[131] presented a detailed discussion of the effect of N on the error of the discrete approximation of the relaxation spectrum. The nonequilibrium moduli E_i^{neq} were calculated such that $H_{\text{disc}}(\tau)$ in eq. (A.7) formed a

staircase approximation for $H(\tau)$ in eq. (A.6):[131]

$$\begin{aligned} E_1^{\text{neq}} &= \frac{1}{2}\left(H(\tau_1^{\text{ref}}) + H(\tau_2^{\text{ref}})\right) - E^{\text{eq}}, \\ E_i^{\text{neq}} &= \frac{1}{2}(H(\tau_{i+1}^{\text{ref}}) - H(\tau_{i-1}^{\text{ref}}), 1 < i < N-1, \\ E_N^{\text{neq}} &= E^{\text{neq}} - \sum_i^{N-1} E_i^{\text{neq}}. \end{aligned} \tag{A.9}$$

As shown in Fig. A.1a, the relaxation modulus continuously decreased with increasing time, though at a very slow rate and did not exhibit a clear rubbery plateau. We chose E^{eq} to be the smallest measured stress relaxation modulus. The results for $\left(\tau_i^{\text{ref}}, E_i^{\text{neq}}\right)$ was applied to eq. (A.3) to calculate the master curve for the discrete viscoelastic model. The results, plotted in Fig. A.1(a), showed good agreement with experimental data. The shear moduli were calculate from the Young's moduli as $G^{\text{eq}} = E^{\text{eq}}/2(1+\upsilon_r)$ and $G_i^{\text{neq}} = E_i^{\text{neq}}/2(1+\upsilon_g)$, where the rubbery Poisson's ratio was $\upsilon_r = 0.5$ and glassy Poisson's ratio was $\upsilon_g = 0.35$. The bulk modulus was calculated as, $k = E^{\text{neq}}/3(1-2\upsilon_g)$. The results gave $G^{\text{eq}} = 0.087$ MPa and the bulk modulus $\kappa = 744.4$ MPa. Figure A.1b plots the relaxation spectrum $\left(\tau_i^{\text{ref}}, G_i^{\text{neq}}\right)$. The relaxation moduli $G^{\text{neq}}(\tau)$ decays very slowly, decreasing only 3 order of magnitude over 10^{24} s range of relaxation times.

The temperature-dependent shift factor shift factor was described by a third order polynomial function,

$$a(T) = 2.76 * 10^{-6}T^3 - 4.78 * 10^{-4}T^2 - 0.171T + 28.2, \tag{A.10}$$

which provided a good fit to the experimental data as shown in Fig. A.2. Finally, the temperature-dependent storage modulus, loss modulus, and tanδ can be evaluated for the

linearized viscoelastic model as,

$$
\begin{aligned}
E'(\omega,T) &= E^{\mathrm{eq}} + \sum_{i}^{N} \frac{E_i^{\mathrm{neq}} \omega^2 \left(\tau_i^{\mathrm{ref}} a(T)\right)^2}{1+\omega^2 \left(\tau_i^{\mathrm{ref}} a(T)\right)^2}, \\
E''(\omega,T) &= \sum_{i}^{N} \frac{E_i^{\mathrm{neq}} \omega \tau_i^{\mathrm{ref}} a(T)}{1+\omega^2 \left(\tau_i^{\mathrm{ref}} a(T)\right)^2}, \\
\tan\delta(\omega,T) &= \frac{E''(\omega,T)}{E'(\omega,T)},
\end{aligned}
\tag{A.11}
$$

where $a(T)$ is the shift factor in eq. (A.10).

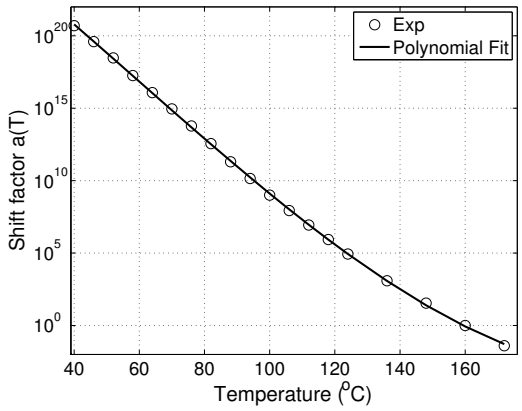

Figure A.2: The temperature-dependent shift factor $a(T)$.

A.3 Results

The constitutive model was applied first to simulate the dynamic temperature sweep experiments described in Sec. A.1.1.2 using the relaxation spectrum obtained from the stress relaxation tests in Fig. A.1. The temperature dependent storage modulus and tanδ were calculated using (A.11) for $\omega = 2\pi$ and $T = 40^{\mathrm{o}}\mathrm{C} - 172^{\mathrm{o}}\mathrm{C}$. The results are compared

to experimental measurements in Fig. A.3. Good quantitatively agreement across the glass transition region. We observed from the tanδ that the glass transition region spanned T = 50^{o}C – 140^{o}C.

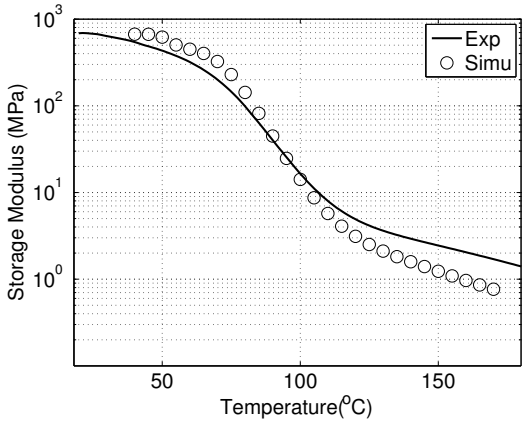

(a)

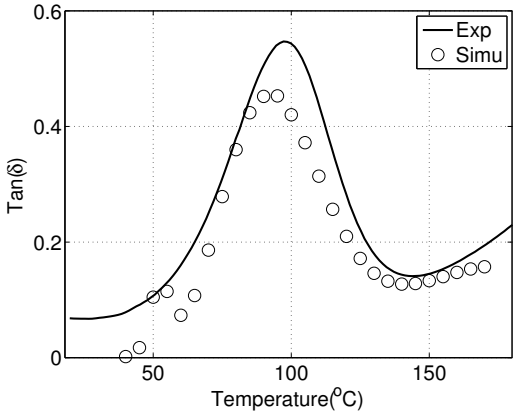

(b)

Figure A.3: Comparing experimental measurements and model predictions of dynamic temperature sweep measurements of: (a) the storage modulus, and (b) tanδ

We applied the model to study the shape recovery of specimens deformed at different programming temperatures describe in Sec. A.1.2.1. Fig A.4.a shows the experimental

and simulation results of the free recovery response of the specimens programmed at 155, 120 and 85°C. The activation temperature for strain recovery increased with the programming temperature. The simulations showed good agreement with the experimental data especially for specimens programmed at 155°C and 120°C. For specimens programmed at 85^oC, the simulation predicted a lower temperature recovery region. The discrepancy was likely caused by structural relaxation, which is a pronounced effect at the onset of the glass transition[106] and was not included in the model. To illustrate the physical mechanism behind the effect of the programming temperature, the normalized distribution of nonequilibrium stresses at end of the cooling period was plotted as a function of the characteristic relaxation time in Fig. A.4b for each relaxation time τ_i^{ref} in the discrete relaxation spectrum. The distribution of nonequilibrium stresses was narrow compared to the distribution of relaxation moduli in Fig. A.1b because faster processes were able to relax to equilibrium for the programing temperature and applied strain rate. The breadth of the distribution of nonequilibrium stresses decreased with increasing programming temperature, and the peak of the distribution shifted towards smaller relaxation times for lower programming temperatures. This allowed for faster shape recovery.

Fig. A.5 shows the experimental and simulation results for the multi-staged shape recover experiments described in Sec. A.1.2.2. The simulations showed good agreement with the experimental results. At each recovery temperature, the specimens achieved a partial shape recovery, though the results showed that recovery continued to persist at a significantly reduced rate. This demonstrated that multi-staged shape-recovery at discrete

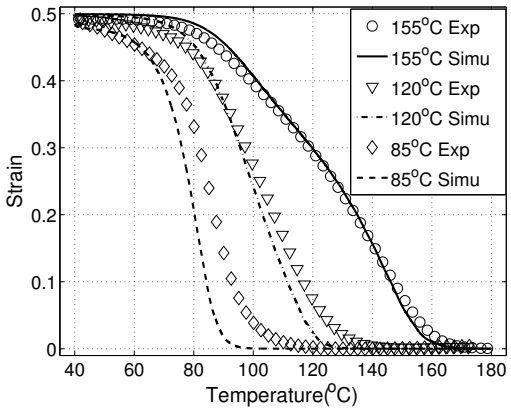

(a)

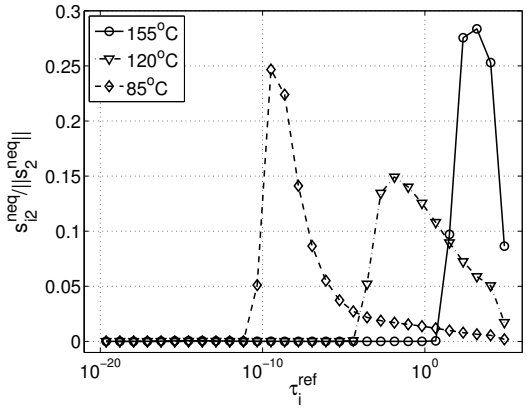

(b)

Figure A.4: Influence of the deformation temperature on shape recovery. (a) Comparison of experimental and simulation results for the unconstrained recovery behavior at different deformation programming temperature, (b) The distribution of nonequilibrium stresses at the end of the programming process before unloading.

temperatures is a manifestation of the very broad relaxation spectrum with relaxation times. The distribution of relaxation times for Nafion was significantly larger than laboratory time scale, which allowed the material to obtain the quasi-stable nonequilibrium shape at each recovery temperature.

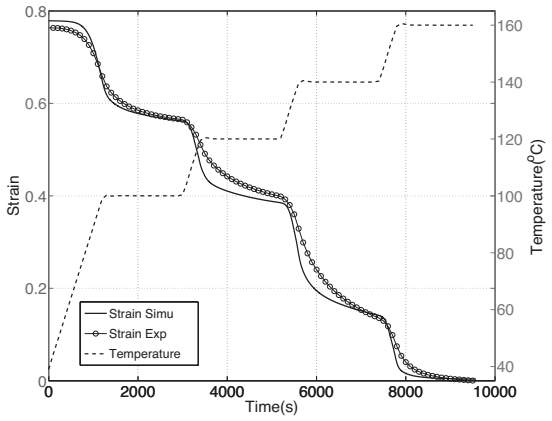

Figure A.5: Comparing the experimental results and model predictions for the free shape recovery response at multiple temperature steps.

Fig. A.6 plots the recovery behavior of specimens programmed at two different temperatures (Sec. A.1.2.3), showing good agreement between experiments and simulations. The initial recovery of the specimens programmed at 155°C and 85°C coincided with the recovery curve of the specimen programmed at 120°C and 85°C. The two curves separated at 80°C, which corresponded to the activation temperature for shape recovery of specimens programmed at 120°C in the single-step programming experiment (Fig. A.4). In contrast, the recovery curves of the specimens programmed at 155°C and 120°C and at 155°C and 85°C were initially different, but merged at 130°C. The 130°C coincided with the temperature at which specimens programmed at a single 120°C temperature achieved fully

recovery (Fig. A.4).

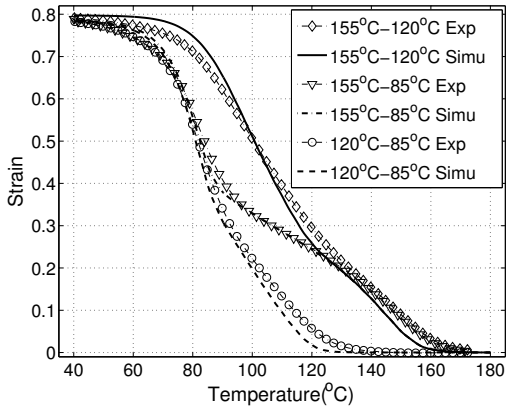

Figure A.6: Shape recovery of specimens programmed at two different temperatures, comparing experiments and model predictions.

The nonlinear viscoelastic model was implemented for finite element analysis (Tahoe©, Sandia National Laboratories) [2] and applied to describe the multiple shape memory effect of a membrane with a period array of holes (Fig A.7a). A series of pattern transformations was programmed in the membrane at different temperatures by applying deformations to trigger a mechanical instability.[175–178] The numerical examples combined the multiple shape memory effect and mechanical instability to achieve multiple temperature activated pattern transformation. The repeating unit cell shown in Fig. A.7 was used to describe a membrane with a periodic array of circular holes. The unit cell was discretized using hexahedral elements and only one layer element was used in the thickness direction as shown in Fig A.7.b.

In order to simulate the deformation through the mechanical instability and bias the buckled configuration, the shape of the bottom-left circle was perturbed into an ellipse

[2] http://sourceforge.net/projects/tahoe/

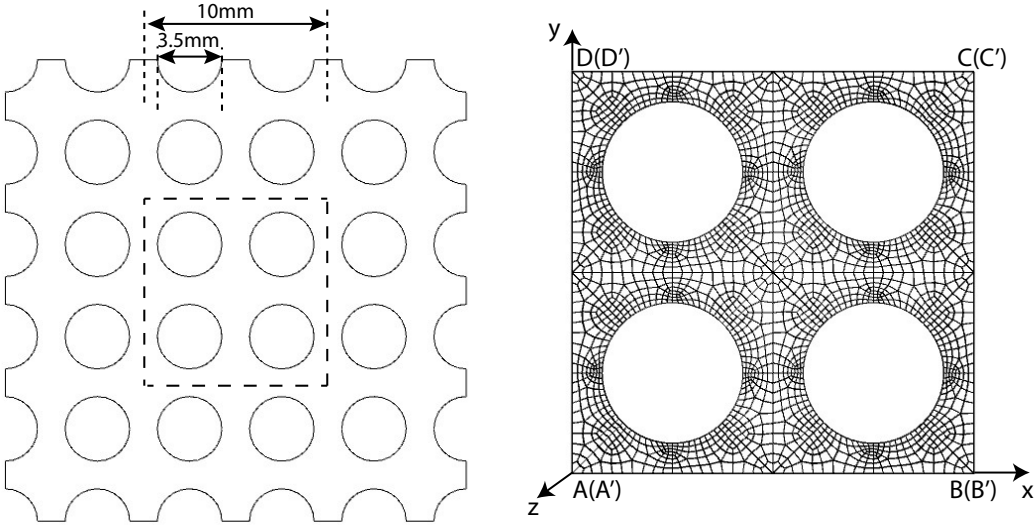

Figure A.7: (a) Schematic of Nafion membrane with a periodic array of circular holes, (b) finite element model of a representative unit cell of the Nafion membrane.

with a major axis that was 0.14% larger than the minor axis. The displacements were fixed as follows: $u_z(x, y, 0) = 0, u_x(0, 0, 0) = 0, u_y(0, 0, 0) = 0$. In addition, periodic boundary conditions were applied to the x surfaces ($AA'B'B$, $DD'C'C$) and y surfaces ($AA'D'D$, $BB'C'C$). The membrane was deformed in the z direction to -25% engineering strain over 100 seconds at 160°C. The boundary conditions were chosen to simulate the experiments of,[178] which used hot-pressing to trigger the pattern transformation of an SMP periodic membrane. The applied programmed shape at different strain level is shown in Fig A.8. The mechanical instability transformed the circular holes into alternating horizontal and vertical ellipses. The programmed membrane was cooled to 120°C at 6°C/min and stretched from -25% to 25% engineering strain in the z direction. The tension in the z direction opened the ellipses returning the shape to the original periodic array of circular holes. The third temporary programmed shape was achieved by cooling the membrane to

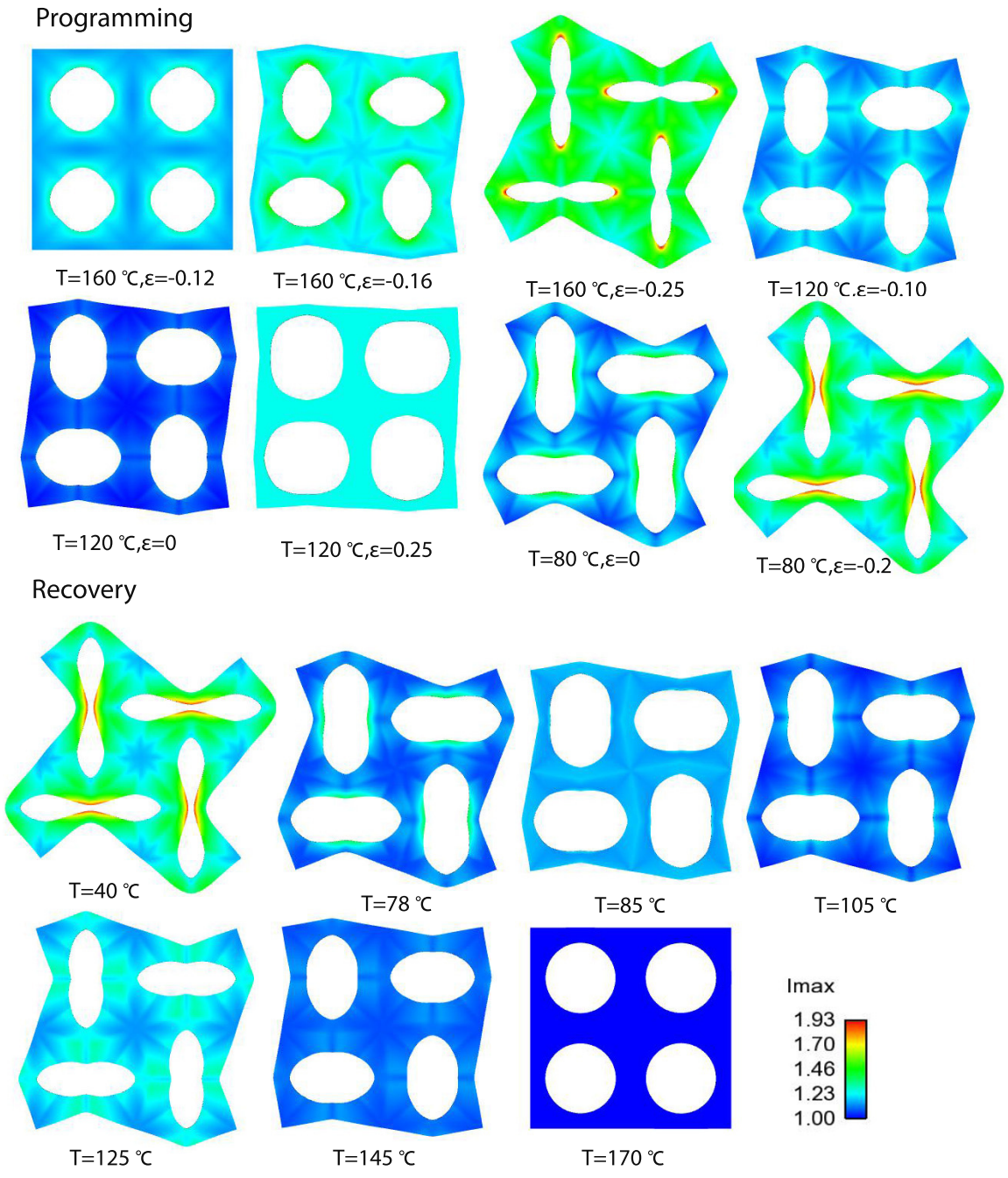

Figure A.8: The shape memory programming and recovery of the Nafion membrane with a periodic array of circular holes shown multiple switchable pattern transformation.

80°C at 6°C/min and then compressing again in z to -20% strain at 80°C. The final shape, an array of alternating horizontal and vertical ellipses, was fixed by cooling the membrane to 40°C at 6°C/min under fixed compression strain and unloaded.

The membrane was heated to 170°C at 1°C/min to achieve shape recovery under traction-free conditions in z, the thickness direction. The recovered shape is shown in Fig A.8 at different temperatures. As shown at $T = 40°C$, unloading in z had negligible effect on the programmed shape. No pronounced recovery occurred until 70°C. The elliptical holes continuously opened with increasing temperature until 85°C and then closed to reach the ellipses with larger aspect ratio with increasing temperature to 125°C. The elliptical holes then opened again, transforming to the permanent circular shape. The membrane achieved fully recovery at 170°C. As shown, the multiple pattern transformation can be achieved by combining mechanical instability and the multiple shape memory effect. Stretching the thin film in the thickness direction to program the second temporary shape may be difficult to achieve in experiments. Alternatively, pattern transformation can be achieved by deforming the film through uniaxial or biaxial compression in the plane.[176,177] Stretching the film in the plane would open the collapsed holes to achieve the second temporary shape for this loading configuration.

Appendix B

Finite Element Implementation of a Coupled Thermal-mechanical Model

In this appendix, the thermal-mechanical coupled model developed in Chapter 4 is implemented as a user-defined element subroutine into finite element code. The constitutive equations are first summarized and the procedures of the numerical implementation are described.

B.1 Constitutive Equations

The deformation gradient tensor, strain and stress tensor are defined in Chapter 2-4. The explicit form of the Second Piola-Kirchhoff stress tensor is given as,

$$\mathbf{S} = \sum_{i}^{P} \phi_i T_{e_i} \mu^{\mathrm{eq}} J^{-2/3} \left(\mathbf{I} - \frac{1}{3} \mathrm{tr}\left(\mathbf{C}\right) \mathbf{C}^{-1} \right) + \sum_{j}^{N} \mu_j^{\mathrm{neq}} J_j^{\mathrm{e}-2/3} \mathbf{F}_j^{\mathrm{v}-1} \left(\mathbf{I} - \frac{1}{3} \mathrm{tr}\left(\mathbf{C}_j^{\mathrm{e}}\right) \mathbf{C}_j^{\mathrm{e}-1} \right) \mathbf{F}_j^{\mathrm{v}-T}. \tag{B.1}$$

The inelastic flow stress is given as,

$$\mathbf{M}_j = \mu_j^{\mathrm{neq}} \left(\overline{\mathbf{C}}_j^{\mathrm{e}} - \frac{1}{3} \mathrm{tr}\left(\overline{\mathbf{C}}_j^{\mathrm{e}}\right) \mathbf{I} \right), \tag{B.2}$$

The evolution equations of the internal variable $\mathbf{F}_j^v$ are,

$$\mathbf{D}_j^{\mathrm{v}} = \frac{1}{2\upsilon_j} \mathbf{M}_j, j = 1 : N, \tag{B.3}$$

In developing the nonequilibrium thermodynamics theory, the effective temperatures are treated as state variables. Due to the large number of effective temperatures, the effective temperature in the finite element simulations are treated as internal variables and only evaluated at the integration points. The evolution equations for the effective temperatures are,

$$\dot{T}_{e_i} = \frac{T - T_{e_i}}{\tau_i} + \underbrace{\frac{a}{\Delta c} \sum_{j}^{N} \mathbf{M}_j : \mathbf{D}_j^{\mathrm{v}}}_{\mathcal{W}_i^{\mathrm{int},c}} + \underbrace{\frac{J^{-2/3} T_{e_i} \mu^{\mathrm{eq}}}{2\Delta c T_0} \left(\mathbf{I} - \frac{1}{3} \mathrm{tr}\left(\mathbf{C}\right) \mathbf{C}^{-1} \right) : \dot{\mathbf{C}}}_{\mathcal{H}_i^{\mathrm{e,c}}}. \tag{B.4}$$

To be simple, the diffusion of the effective temperatures is ignored in the current implementation.

B.2 Numerical Solution Procedure

The following implementation procedure is developed on the reference configuration. The similar procedure can be also developed on the current configuration. The strong forms of the coupled thermal-mechanical model are summarized as,

$$\text{Balance of Momentum} \begin{cases} \text{Div}\,(\mathbf{FS}) + \mathbf{B} = 0 \quad in \quad \Omega \\ \mathbf{U} = \widehat{\mathbf{U}} \quad on \quad \Omega_u, \\ \mathbf{T} = \mathbf{FS}\cdot\mathbf{N} = \widehat{\mathbf{T}} \quad on \quad \Omega_t \end{cases} \tag{B.5}$$

$$\text{Balance of Energy} \begin{cases} c_g\dot{T} + \sum_i^P \Delta c_i \dot{T}_{e_i} = -\nabla_{\mathbf{X}}\cdot\mathbf{Q} + W_{\text{dis}} \quad in \quad \Omega \\ T = \widehat{\mathbf{T}} \quad on \quad T_n, \\ Q = \widehat{Q_n} \quad on \quad Q_n \end{cases} \tag{B.6}$$

where W_{dis} is the total heat generation from the dissipation. With the weighting functions are defined as $\mathbf{W}$ and Θ, the corresponding weak form of the above equations are,

$$\text{Weak form} \begin{cases} \int \boldsymbol{\nabla}\mathbf{W} : (\mathbf{FS})\, dV = \int \mathbf{W}\cdot\mathbf{B}dV + \int \mathbf{W}\cdot\mathbf{T}_n dS, \\ \int \Theta c_g \dot{T} dV + \sum_l^P \int \Theta \Delta c_i \dot{T}_{e_i} dV - \int \boldsymbol{\nabla}\Theta\cdot\mathbf{Q}dV = \int \Theta\widehat{Q}_n dS + \int \Theta W_{\text{dis}} dV. \end{cases} \tag{B.7}$$

The following shape functions and trial functions are defined

$$\begin{cases} \mathbf{W} = \sum N_A \mathbf{W}_A, \quad \Theta = \sum N_A \Theta_A, \\ \mathbf{U} = \sum N_A \mathbf{U}_A, \quad T = \sum N_A T_A \qquad \dot{T} = \sum N_A \dot{T}_A. \end{cases} \tag{B.8}$$

Using the above equations, the weak forms can be discretized as,

$$\begin{cases} \int (\mathbf{FS}) \frac{\partial N_A}{\partial \mathbf{X}} dV = \int N_A \mathbf{B} dV + \int N_A \mathbf{T}_n dS \\ \int N_A N_B c_g \dot{T}_B dV + \sum_l^P \int N_A \Delta c_i \dot{T}_{e_i} dV - \int \frac{\partial N_A}{\partial \mathbf{X}}\cdot\mathbf{Q}dV = \int N_A \widehat{Q}_n dS + \int N_A W_{\text{dis}} dV. \end{cases} \tag{B.9}$$

APPENDIX B. FINITE ELEMENT IMPLEMENTATION OF A COUPLED THERMAL-MECHANICAL MODEL

The coupled equations are solved using Newton raphson procedure. The residuals are defined as,

$$\begin{cases} R_A^{\mathbf{U}} = \int (\mathbf{FS}) \frac{\partial N_A}{\partial \mathbf{X}} dV - \int N_A \mathbf{B} dV - \int N_A \mathbf{T}_n dS \\ R_A^{\dot{T}} = \int N_A N_B c_g \dot{T}_B dV + \sum_l^P \int N_A \Delta c_i \dot{T}_{e_i} dV - \int \frac{\partial N_A}{\partial \mathbf{X}} \cdot \mathbf{Q} dV - \int N_A \widehat{Q}_n dS - \int N_A W_{\text{dis}} dV. \end{cases} \tag{B.10}$$

The tangents can be obtained through,

$$\begin{cases} K_{AB}^{\mathbf{UU}} = \frac{\partial R_A^{\mathbf{U}}}{\partial \mathbf{U}_B}, \\ K_{AB}^{\mathbf{U}\dot{T}} = \frac{\partial R_A^{\mathbf{U}}}{\partial \dot{T}_B}, \\ K_{AB}^{\dot{T}\mathbf{U}} = \frac{\partial R_A^{\dot{T}}}{\partial \mathbf{U}_B}, \\ K_{AB}^{\dot{T}\dot{T}} = \frac{\partial R_A^{\dot{T}}}{\partial \dot{T}_B}, \end{cases} \tag{B.11}$$

To obtain the tangent, the residuals in Eq. (B.10) is written in the index form,

$$\begin{cases} R_A^{U_i} = \int F_{ij} S_{jk} \frac{\partial N_A}{\partial X_k} dV - \int N_A B_i dV - \int N_A T_{ni} dS \\ R_A^{\dot{T}} = \int N_A N_B c_g \dot{T}_B dV + \sum_l^P \int N_A \Delta c_i \dot{T}_{e_i} dV - \int \frac{\partial N_A}{\partial X_k} Q_k dV - \int N_A \widehat{Q}_n dS - \int N_A W_{\text{dis}} dV. \end{cases} \tag{B.12}$$

The $K_{AB}^{U_i U_l}$ is given by,

$$K_{AB}^{U_i U_l} = \int \frac{\partial N_A}{\partial X_k} \frac{\partial N_B}{\partial X_j} S_{jk} \delta_{il} dV + \int \frac{\partial N_A}{\partial X_k} \frac{\partial N_B}{\partial X_m} F_{ij} F_{ln} \mathbb{C}_{jkmn} dV \tag{B.13}$$

where the $\mathbb{C}_{jkmn} = \frac{\partial \mathbf{S}_{jk}}{\partial \mathbf{C}_{mn}}$. The second term of the right side of eq. (B.13) is similar to the stiffness matrix of linear theory while the first terms is caused by an initial stress contribution. To obtain the material tangent moduli $\mathbb{C}_{jkmn}$, some numerical methods (for example, Holzapfel,[174] and Reese and Govindjee[127]) have been developed based on the spectrum deposition. In our implementation, the Reese-Govindjee method (RG split method) is adopted.

APPENDIX B. FINITE ELEMENT IMPLEMENTATION OF A COUPLED THERMAL-MECHANICAL MODEL

To obtain the $K_{AB}^{\dot{T}\dot{T}}$, the relationship between T and $\dot{T}$ needs to be provided. In order to obtain the temperature T from the temperature rate $\dot{T}$, the Crank-Nicolson method is adopted. The predictor of temperature is defined as,

$$\widetilde{T}_n = T_n + (1-\alpha)\Delta t\dot{T}_n. \tag{B.14}$$

The temperature can be calculated through the predictor,

$$T_{n+1} = \widetilde{T}_n + \alpha\Delta t\dot{T}_{n+1}. \tag{B.15}$$

Thus, $\Delta T = \alpha\Delta t\Delta\dot{T}$ can be obtained. The Fourier law is adopted for heat condition, $\mathbf{Q} = -k_0\mathbf{C}^{-1}\nabla T$, where k_0 is thermal conductivity coefficient. The heat convection between the specimen and air is described by $\widehat{Q}_n = h_0(T - T_{\text{env}})$, where h_0 is the heat transfer coefficient and T_{env} is the temperature of the environment. With all the above relationships, $R_A^{\dot{T}}$ can be written as,

$$R_A^{\dot{T}} = \int N_A N_B c_g \dot{T}_B dV + \int \frac{\partial N_A}{\partial X_k} k_0 C_{kj}^{-1} \frac{\partial T}{\partial X_j} dV - \int N_A h_0 (T - T_{\text{env}}) dS - \int N_A W_{\text{pdis}} dV. \tag{B.16}$$

where $W_{\text{psis}} = W_{\text{dis}} - \sum_l^P \Delta c_i \dot{T}_{e_i}$ represents the fraction of viscous dissipation flow into the kinetic subsystem. $K_{AB}^{\dot{T}\dot{T}}$ is calculated as,

$$K_{AB}^{\dot{T}\dot{T}} = \int N_A N_B c_g dV + \alpha\Delta t \left(\int \frac{\partial N_A}{\partial X_k} k_0 C_{kj}^{-1} \frac{\partial N_B}{\partial X_j} dV - \int N_A h_0 N_B dS - \int N_A \frac{\partial W_{\text{pdis}}}{\partial T} N_B dV \right). \tag{B.17}$$

$K_{AB}^{\mathbf{U}\dot{T}}$ and $K_{AB}^{\dot{T}\mathbf{U}}$ can be estimated as,

$$\begin{cases} K_{AB}^{U_i\dot{T}} = \alpha\Delta t \int F_{ij} \frac{\partial S_{jk}}{\partial T} \frac{\partial N_A}{\partial X_k} dV \\ K_{AB}^{\dot{T}U_l} = -\int \frac{\partial N_A}{\partial X_k} \frac{\partial N_A}{\partial X_m} k_0 C_{km}^{-1} C_{nj}^{-1} F_{ln} \frac{\partial T}{\partial X_j} dV - \int N_A \frac{\partial N_B}{\partial X_j} \frac{\partial W_{\text{pdis}}}{\partial C_{ij}} F_{li} dV. \end{cases} \tag{B.18}$$

APPENDIX B. FINITE ELEMENT IMPLEMENTATION OF A COUPLED THERMAL-MECHANICAL MODEL

The explicit function of $\mathbf{S}$ is not directly expressed by T and W_{pdis} is also not directly related with $\mathbf{C}$. Thus the explicit form of these two terms is obtained through chain rule as,

$$\begin{aligned}\frac{\partial \mathbf{S}}{\partial T} &= \sum_{i}^{P} \frac{\partial \mathbf{S}}{\partial T_{e_i}} \frac{\partial T_{e_i}}{\partial T} + \sum_{j}^{N} \frac{\partial \mathbf{S}}{\partial \mathbf{F}_j^v} : \frac{\partial \mathbf{F}_j^v}{\partial T}, \\ \frac{\partial W_{\text{pdis}}}{\partial \mathbf{C}} &= \sum_{i}^{P} \frac{\partial W_{\text{pdis}}}{\partial T_{e_i}} \frac{\partial T_{e_i}}{\partial \mathbf{C}} + \sum_{j}^{N} \frac{\partial W_{\text{pdis}}}{\partial \mathbf{F}_j^v} : \frac{\partial \mathbf{F}_j^v}{\partial \mathbf{C}}.\end{aligned} \tag{B.19}$$

The $\frac{\partial T_{e_i}}{\partial T}, \frac{\partial \mathbf{F}_j^v}{\partial T}, \frac{\partial T_{e_i}}{\partial \mathbf{C}}$ and $\frac{\partial \mathbf{F}_j^v}{\partial \mathbf{C}}$ are obtained through satisfying the evolution equation of viscous flow (eq. (B.3)) and the evolution equation of effective temperatures (eq. (B.4)) at the intergraion point. The detailed information can be found in Reese and Govindjee[127] and is not provided in this thesis.

Bibliography

[1] B. K. Kim, S. Y. Lee, and M. Xu, "Polyurethanes having shape memory effects," *Polymer*, vol. 37, no. 26, pp. 5781 – 5793, 1996.

[2] A. Lendlein and S. Kelch, "Shape-memory polymers," *Angewandte Chemie International Edition*, vol. 41, pp. 2034–2057, 2002.

[3] C. Liu, H. Qin, and P. T. Mather, "Review of progress in shape-memory polymers," *Journal of Materials Chemistry*, vol. 17, pp. 1543–1558, 2007.

[4] C. M. Yakacki, R. Shandas, D. Safranski, A. M. Ortega, K. Sassaman, and K. Gall, "Strong, tailored, biocompatible shape-memory polymer networks," *Advanced Functional Materials*, vol. 18, pp. 2428–2435, 2008.

[5] M. Behl, M. Razzaq, and A. Lendlein, "Multifunctional shape-memory polymers," *Adv. Mater.*, vol. 22, pp. 3388—-3410, 2010.

[6] A. Lendlein, H. Jiang, O. Junger, and R. Langer, "Light-induced shape-memory polymers," *Nature*, vol. 434, pp. 879–882, 2005.

[7] K. N. Long, T. F. Scott, H. J. Qi, C. N. Bowman, and M. L. Dunn, "Photomechanics of light-activated polymers," *J. Mech. Phys. Solids*, vol. 57, no. 7, pp. 1103–1121, 2009.

[8] L. Wu, C. Jin, and X. Sun, "Synthesis, properties, and light-induced shape memory effect of multiblock polyesterurethanes containing biodegradable segments and pendant cinnamamide groups," *Biomacromolecules*, vol. 12, no. 1, pp. 235–241, 2010.

[9] S.-Q. Wang, D. Kaneko, M. Okajima, K. Yasaki, S. Tateyama, and T. Kaneko, "Hyperbranched polycoumarates with photofunctional multiple shape memory," *Angewandte Chemie International Edition*, vol. 52, no. 42, pp. 11 143–11 148, 2013.

[10] J. W. Cho, J. W. Kim, Y. C. Jung, and N. S. Goo, "Electroactive shape-memory polyurethane composites incorporating carbon nanotubes," *Macromolecular Rapid Communications*, vol. 26, no. 5, pp. 412–416, 2005.

[11] J. Leng, H. Lv, Y. Liu, and S. Du, "Electroactivate shape-memory polymer filled with nanocarbon particles and short carbon fibers," *Applied Physics Letters*, vol. 91, no. 14, p. 144105, 2007.

[12] J. Leng, W. Huang, X. Lan, Y. Liu, and S. Du, "Significantly reducing electrical resistivity by forming conductive ni chains in a polyurethane shape-memory polymer/carbon-black composite," *Applied Physics Letters*, vol. 92, no. 20, p. 204101, 2008.

[13] X.-J. Han, Z.-Q. Dong, M.-M. Fan, Y. Liu, Y.-F. Wang, Q.-J. Yuan, B.-J. Li, S. Zhang *et al.*, "ph-induced shape-memory polymers," *Macromolecular rapid communications*, vol. 33, no. 12, pp. 1055–1060, 2012.

[14] B. Yang, W. Huang, C. Li, C. Lee, and L. Li, "On the effects of moisture in a polyurethane shape memory polymer," *Smart materials and structures*, vol. 13, no. 1, p. 191, 2003.

[15] S. Chen, J. Hu, C. Yuen, and L. Chan, "Novel moisture-sensitive shape memory polyurethanes containing pyridine moieties," *Polymer*, vol. 50, no. 19, pp. 4424–4428, 2009.

[16] H. Du and J. Zhang, "Solvent induced shape recovery of shape memory polymer based on chemically cross-linked poly (vinyl alcohol)," *Soft Matter*, vol. 6, no. 14, pp. 3370–3376, 2010.

[17] X. Gu and P. T. Mather, "Water-triggered shape memory of multiblock thermoplastic polyurethanes (tpus)," *Rsc Advances*, vol. 3, no. 36, pp. 15 783–15 791, 2013.

[18] C. Liu, S. B. Chun, P. T. Mather, L. Zheng, E. H. Haley, and E. B. Coughlin, "Chemically cross-linked polycyclooctene: synthesis, characterization, and shape memory behavior," *Macromolecules*, vol. 35, no. 27, pp. 9868–9874, 2002.

[19] W. Wagermaier, K. Kratz, M. Heuchel, and A. Lendlein, "Characterization methods

for shape-memory polymers," in *Shape-Memory Polymers*. Springer, 2010, pp. 97–145.

[20] A. Lendlein and R. Langer, "Biodegradable, elastic shape-memory polymers for potential biomedical applications," *Science*, vol. 296, no. 5573, pp. 1673–1676, 2002.

[21] C. M. Yakacki, R. Shandas, C. Lanning, B. Rech, A. Eckstein, and K. Gall, "Unconstrained recovery characterization of shape-memory polymer networks for cardiovascular applications," *Biomaterials*, vol. 28, pp. 2255–2263, 2007.

[22] Y. Liu, J. Leng, J. Leng, and S. Du, *Applications of Shape Memory Polymers in Aerospace*. CRC Press: Boca Raton, FL, 2010.

[23] J. Hu, *Shape memory polymers and textiles*. Elsevier, 2007.

[24] G. Zhu, G. Liang, Q. Xu, and Q. Yu, "Shape-memory effects of radiation crosslinked poly (?-caprolactone)," *Journal of Applied Polymer Science*, vol. 90, no. 6, pp. 1589–1595, 2003.

[25] I. A. Rousseau and P. T. Mather, "Shape memory effect exhibited by smectic-c liquid crystalline elastomers," *Journal of the American Chemical Society*, vol. 125, no. 50, pp. 15 300–15 301, 2003.

[26] L. E. Nielsen, *Mechanical properties of polymers*. Van Nostrand Reinhold, 1962.

[27] J. D. Ferry, *Viscoelastic Properties of Polymers*. New York, NY: John Wiley and Sons, 1980.

[28] G. Höhne, W. Hemminger, and H.-J. Flammersheim, *Differential scanning calorimetry*. Springer, 2003.

[29] O. Hasan and M. C. Boyce, "Energy storage during inelastic deformation of glassy polymers," *Polymer*, vol. 34, no. 24, pp. 5085–5092, 1993.

[30] L. H. Sperling, *Introduction to physical polymer science*. John Wiley & Sons, 2005.

[31] A. J. Kovacs, "La contraction isotherme du volume des polymeres amorphes," *Journal of polymer science*, vol. 30, no. 121, pp. 131–147, 1958.

[32] J. Lennard-Jones and A. Devonshire, "Critical phenomena in gases. i," *Proceedings of the Royal Society of London. Series A, Mathematical and Physical Sciences*, pp. 53–70, 1937.

[33] D. Turnbull and M. H. Cohen, "Free-volume model of the amorphous phase: glass transition," *The Journal of Chemical Physics*, vol. 34, no. 1, pp. 120–125, 1961.

[34] J. H. Gibbs and E. A. DiMarzio, "Nature of the glass transition and the glassy state," *J. Chem. Phys.*, vol. 28, p. 373, 1958.

[35] G. H. Fredrickson and H. C. Andersen, "Facilitated kinetic ising models and the glass transition," *The Journal of chemical physics*, vol. 83, no. 11, pp. 5822–5831, 1985.

[36] J. M. Brader, T. Voigtmann, M. Fuchs, R. G. Larson, and M. E. Cates, "Glass rhe-

ology: From mode-coupling theory to a dynamical yield criterion," *Proceedings of the National Academy of Sciences*, vol. 106, no. 36, pp. 15 186–15 191, 2009.

[37] S. F. Edwards and P. W. Anderson, "Theory of spin glasses," *Journal of Physics F: Metal Physics*, vol. 5, no. 5, p. 965, 1975.

[38] V. Lubchenko and P. G. Wolynes, "Theory of structural glasses and supercooled liquids," *arXiv preprint cond-mat/0607349*, 2006.

[39] G. Adam and J. H. Gibbs, "On the temperature dependence of cooperative relaxation properties in the glass-forming liquids," *J. Chem. Phys.*, vol. 43, pp. 139–146, 1965.

[40] A. K. Doolittle, "Studies in newtonian flow. ii. the dependence of the viscosity of liquids on free-space," *Journal of Applied Physics*, vol. 22, no. 12, pp. 1471–1475, 1951.

[41] M. L. Williams, R. F. Landel, and J. D. Ferry, "The temperature dependence of relaxation mechanisms in amorphous polymers and other glass-forming liquids," *Journal of the American Chemical Society*, vol. 77, pp. 3701–3707, 1955.

[42] I. Hodge, "Effects of annealing and prior history on enthalpy relaxation in glassy polymers: Adam-gibbs formulation of nonlinearity," *Macromolecules*, vol. 20, pp. 2897–2908, 1987.

[43] G. L. Danton, *Engineering viscoelasticity*. US: Springer, 2014.

[44] W. Voit, T. Ware, R. R. Dasari, P. Smith, L. Danz, D. Simon, S. Barlow, S. R. Marder, and K. Gall, "High-strain shape-memory polymers," *Advanced functional materials*, vol. 20, no. 1, pp. 162–171, 2010.

[45] T. Nguyen, H. J. Qi, F. Castro, and K. N. Long, "A thermoviscoelastic model for amorphous shape memory polymers: Incorporating structural and stress relaxation," *J. Mech. Phys. Solids*, vol. 56, pp. 2792–2814, 2008.

[46] N. Lakhera, C. M. Yakacki, T. Nguyen, and C. P. Frick, "Partially-constrained recovery of (meth)acrylate shape-memory polymer networks," *J. App. Poly. Phys..*, vol. 126, no. 1, pp. 72–82, 2012.

[47] C. M. Yakacki, A. M. Ortega, C. P. Frick, N. Lakhera, R. Xiao, and T. D. Nguyen, "Unique recovery behavior in amorphous shape-memory polymer networks," *Macromolecular Materials and Engineering*, vol. 297, no. 12, pp. 1160–1166, 2012.

[48] P. Ping, W. Wang, X. Chen, and X. Jing, "Ploy(ϵ-caprolactone polyurethane and its shape-memory property," *Biomacromolecules*, vol. 6, pp. 587–592, 2005.

[49] K. Gall, C. M. Yakacki, Y. Liu, R. S. adn N. Willet, and K. S. Anseth, "Thermomechanics of the shape memory effect in polymers for biomedical applications," *Journal of Biomedical Materials Research: Part A*, vol. 73, pp. 339–348, 2005.

[50] G. Rabani, H. Luftmann, and A. Kraft, "Synthesis and characterization of two shape-

memory polymers containing short aramid hard segments and poly(ϵ-caprolactone) soft segments," *Polymers*, vol. 47, pp. 4251–4260, 2006.

[51] Z. Wang, Z. Li, L. Wang., Z. Xiong, Z. Wang, Z. Li, L. Wang, and Z. Xiong, "Viscoelastic characteristics of shape memory polymers," *J. App. Poly. Phys.*., vol. 118, pp. 1406–1413, 2010.

[52] G. Li and W. Xu, "Thermomechanical behavior of thermoset shape memory polymer programmed by cold-compression: Testing and constitutive modeling," *J. Mech. Phys. Solids*, vol. 59, pp. 1231–1250, 2011.

[53] Y. Liu, K. Gall, M. Dunn, and P. McCluskey, "Thermomechanical recovery coupling of shape memory polymers in flexure," *Smart Mater. Struct.*, vol. 12, pp. 947–954, 2003.

[54] P. Miaudet, A. Derre, M. Maugey, C. Zakri, P. Piccione, R. Inoubli, and P. Poulin, "Shape and temperature memory of nanocomposites with broadened glass transition," *Science*, vol. 318, pp. 1294–1296, 2007.

[55] F. Grillard, C. Zakri, P. Gaillard, A. Korzhenko, W. Néri, and P. Poulin, "How polymers lose memory with age," *Soft matter*, vol. 10, no. 44, pp. 8985–8991, 2014.

[56] L. Sun, W. M. HUANG, C. C. WANG, Y. ZHAO, Z. DING, and H. PURNAWALI, "Optimization of the shape memory effect in shape memory polymers," *J. App. Poly. Phys. Part A: Poly. Chem.*, vol. 49, pp. 3574–3581, 2011.

[57] H. Tobushi, H. Hashimoto, S. Hayashi, and E. Yamada, "Thermomechanical constitutive model of shape memory polymer of polyurethane series," *J. Intell. mater. Syst. Struct.*, vol. 8, pp. 711–718, 1997.

[58] J. Morshedian, H. A. Khonakdar, and S. Rasouli, "Modeling of shape memory induction and recovery in heat-shrinkable polymers," *Macromolecular Theory and Simulations*, vol. 14, pp. 428–434, 2005.

[59] C. P. Buckley, C. Prisacariu, and A. Caraculacu, "Novel triol-crosslinked polyurethanes and their thermorheological characterization as shape-memory materials," *Polymers*, vol. 48, pp. 1338–1396, 2007.

[60] K. Yu, Q. Ge, and H. J. Qi, "Reduced time as a unified parameter determining fixity and free recovery of shape memory polymers," *Nature communications*, vol. 5, 2014.

[61] Q. Ge, K. Yu, Y. Ding, and H. J. Qi, "Prediction of temperature-dependent free recovery behaviors of amorphous shape memory polymers," *Soft Matter*, vol. 8, no. 43, pp. 11 098–11 105, 2012.

[62] H. Tobushi, K. Okamura, S. Hayashi, and N. Ito, "Thermomechanical constitutive model of shape memory polymer," *Mechanics of Materials*, vol. 33, pp. 545–554, 2001.

[63] M. C. Boyce, D. M. Parks, and A. S. Argon, "Large inelastic deformation of glassy

polymers. part i: rate dependent constitutive model," *Mechanics of Materials*, vol. 7, pp. 15 – 33, 1988.

[64] E. M. Arruda and M. C. Boyce, "Evolution of plastic anisotropy in amorphous polymers during finite straining," *International Journal of Plasticity*, vol. 9, pp. 697 – 720, 1993.

[65] R. B. Dupaix and M. C. Boyce, "Constitutive modeling of the finite strain behavior of amorphous polymers in and above the glass transition," *Mechanics of Materials*, vol. 39, pp. 39–52, 2007.

[66] C. P. Buckley and D. C. Jones, "Glass-rubber constitutive model for amorphous polymers near the glass transition," *Polymer*, vol. 36, pp. 3301–3312, 1995.

[67] J. J. Wu and C. Buckley, "Plastic deformation of glassy polystyrene: A unified model of yield and the role of chain length," *J. Poly. Sci. Part B: Poly. Phys.*, vol. 42, pp. 2027–2040, 2004.

[68] T. Tervoort, E. Klompen, and L. Govaert, "A multi-mode approach to finite, three-dimensional, nonlinear viscoelastic behavior of polymer glasses," *Journal of Rheology (1978-present)*, vol. 40, no. 5, pp. 779–797, 1996.

[69] L. E. Govaert, T. A. P. Engels, W. M., T. A. Tervoort, and W. S. Ulrich, "Does the strain hardening modulus of glassy polymers scale with the flow stress," *Journal of Polymer Science Part B: Polymer Physics*, vol. 46, p. 2475Ð2481, 2008.

[70] L. Anand and C. Su, "A theory for amorphous viscoplastic materials undergoing finite deformations, with application to metallic glasses," *Journal of the Mechanics and Physics of Solids*, vol. 53, no. 6, pp. 1362–1396, 2005.

[71] L. Anand and N. M. Ames, "On modeling the micro-indentation response of amorphous polymer," *Int. J. Plas.*, vol. 22, pp. 1123–1170, 2006.

[72] V. Srivastava, S. Chester, and L. Anand, "Thermally actuated shape-memory polymers: Experiments, theory, and numerical simulations," *J. Mech. Phys. Solids*, vol. 58, pp. 1100–1124, 2010.

[73] J. Diani, Y. Liu, and K. Gall, "Finite strain 3d thermoviscoelastic constitutive model for shape memory polymers," *Polymer Engineering and Science*, vol. 46, pp. 486–492, 2006.

[74] J. Diani, P. Gilormini, C. Frédy, and I. Rousseau, "Predicting thermal shape memory of crosslinked polymer networks from linear viscoelasticity," *International Journal of Solids and Structures*, vol. 49, no. 5, pp. 793–799, 2012.

[75] A. Q. Tool, "Relaxation of stresses in annealing glass," *Journal of Research of the National Bureau of Standards*, vol. 34, pp. 199–212, 1945.

[76] G. W. Scherer, *Relaxation in Glass and Composites*. New York, NY: John Wiley and Sons, 1986.

[77] H. Eyring, "Viscosity, Plasticity, and Diffusion as Examples of Absolute Reaction Rates," *J. Chem. Phys.*, vol. 4, pp. 283–291, 1936.

[78] T. D. Nguyen, C. M. Yakacki, P. D. Brahmbhatt, and M. L. Chambers, "Modeling the Relaxation Mechanisms of Amorphous Shape Memory Polymers," *Advanced Materials*, vol. 22, no. 31, Sp. Iss. SI, pp. 3411–3423, 2010.

[79] J. Choi, A. M. Ortega, R. Xiao, C. M. Yakacki, and T. D. Nguyen, "Effect of physical aging on the shape-memory behavior of amorphous networks," *Polymer*, vol. 53, no. 12, pp. 2453–2464, 2012.

[80] W. Huang, C. Song, Y. Fu, C. Wang, Y. Zhao, H. Purnawali, H. Lu, C. Tang, Z. Ding, and J. Zhang, "Shaping tissue with shape memory materials," *Advanced drug delivery reviews*, vol. 65, no. 4, pp. 515–535, 2013.

[81] W. Huang, B. Yang, L. An, C. Li, and Y. Chan, "Water-driven programmable polyurethane shape memory polymer: demonstration and mechanism," *Applied Physics Letters*, vol. 86, no. 11, p. 114105, 2005.

[82] B. Yang, W. Huang, C. Li, C. Lee, and L. Li, "On the effects of moisture in a polyurethane shape memory polymer," *Smart materials and structures*, vol. 13, no. 1, p. 191, 2004.

[83] B. Yang, W. Huang, C. Li, and L. Li, "Effects of moisture on the thermomechanical

properties of a polyurethane shape memory polymer," *Polymer*, vol. 47, no. 4, pp. 1348–1356, 2006.

[84] H. Lu, Y. Liu, J. Leng, and S. Du, "Qualitative separation of the physical swelling effect on the recovery behavior of shape memory polymer," *European Polymer Journal*, vol. 46, no. 9, pp. 1908–1914, 2010.

[85] A. Kirkpatrick, "Some relations between molecular structure and plasticizing effect," *Journal of Applied Physics*, vol. 11, no. 4, pp. 255–261, 1940.

[86] F. Kelley and F. Bueche, "Viscosity and glass temperature relations for polymer-diluent systems," *Journal of Polymer Science*, vol. 50, no. 154, pp. 549–556, 1961.

[87] G. U. Losi and W. G. Knauss, "Free volume theory and nonlinear thermoviscoelasticity," *Polymer Engineering & Science*, vol. 32, no. 8, pp. 542–557, 1992.

[88] E. Dimarzio and J. Gibbs, "Molecular interpretation of glass temperature depression by plasticizers," *Journal of Polymer Science Part A: General Papers*, vol. 1, no. 4, pp. 1417–1428, 1963.

[89] T. Chow, "Molecular interpretation of the glass transition temperature of polymer-diluent systems," *Macromolecules*, vol. 13, no. 2, pp. 362–364, 1980.

[90] L. Struik, "Physical aging in amorphous glassy polymers," *Annals of the New York Academy of Sciences*, vol. 279, no. 1, pp. 78–85, 1976.

[91] J. M. Hutchinson, "Physical aging of polymers," *Progress in Polymer Science*, vol. 20, no. 20, pp. 703–760, 1993.

[92] I. M. Hodge, "Physical aging in polymer glasses," *SCIENCE-NEW YORK THEN WASHINGTON-*, pp. 1945–1945, 1995.

[93] H. E. Meijer and L. E. Govaert, "Mechanical performance of polymer systems: the relation between structure and properties," *Progress in polymer science*, vol. 30, no. 8, pp. 915–938, 2005.

[94] H. G. H. van Melick, L. E. Govaert, B. Raas, W. J. Nauta, and H. E. H. Meijer, "Kinetics of ageing and re-embrittlement of mechanically rejuvenated polystyrene," *Polymer*, vol. 44, pp. 1171 – 1179, 2003.

[95] O. Hasan and M. Boyce, "A constitutive model for the nonlinear viscoelastic viscoplastic behavior of glassy polymers," *Polymer Engineering & Science*, vol. 35, no. 4, pp. 331–344, 1995.

[96] O. S. Narayanaswamy, "A model of structural relaxation in glass," *Journal of the American Ceramics Society*, vol. 54, p. 491, 1971.

[97] C. T. Moynihan, A. J. Easteal, M. A. DeBolt, and J. Tucker, "Dependence of the fictive temperature on the glass cooling rate," *Journal of the American Ceramics Society*, vol. 59, pp. 12–16, 1976.

[98] I. Hodge, "Adam-gibbs formulation of enthalpy relaxation near the glass transition,"

Journal of Research of the National Institute of Standards and Technology, vol. 102, pp. 195–205, 1997.

[99] C. Buckley, P. Dooling, J. Harding, and C. Ruiz, "Deformation of thermosetting resins at impact rates of strain. part 2: constitutive model with rejuvenation," *Journal of the Mechanics and Physics of Solids*, vol. 52, no. 10, pp. 2355–2377, 2004.

[100] T. M. Nieuwenhuizen, "Thermodynamics of the glassy state: Effective temperatureas an additional system parameter," *Phys. Rev. Lett.*, vol. 80, pp. 5580–5583, 1998.

[101] ——, "Thermodynamic description of a dynamical glassy transition," *Journal of Physics A: Mathematical and General*, vol. 31, no. 10, p. L201, 1998.

[102] ——, "Formulation of thermodynamics for the glassy state: Configurational energy as a modest source of energy," *The Journal of Chemical Physics*, vol. 115, no. 17, pp. 8083–8088, 2001.

[103] H. C. Ottinger, "Nonequilibrium thermodynamics of glasses," *Phys. Rev. E.*, vol. 74, pp. 011 113–1–011 113–25, 1975.

[104] L. Leuzzi, "A stroll among effective temperatures in aging systems: Limits and perspectives," *Journal of Non-Crystalline Solids*, vol. 355, no. 10, pp. 686–693, 2009.

[105] L. F. Cugliandolo, "The effective temperature," *arXiv preprint arXiv:1104.4901*, 2011.

[106] R. Xiao, J. Choi, N. Lakhera, C. Yakacki, C. Frick, and T. Nguyen, "Modeling the glass transition of amorphous networks for shape-memory behavior," *Journal of the Mechanics and Physics of Solids*, vol. 61, no. 7, pp. 1612–1635, 2013.

[107] A. Lendlein, S. Kelch, K. Kratz, and J. Schulte, "Shape-memory Polymers," in *Encyclopedia of Materials: Science and Technology*. Elsevier, 2005, pp. 1–9.

[108] P. T. Mather, X. Luo, and I. Rousseau, "Shape memory polymer research," *Annual Review of Materials Research*, vol. 39, pp. 445–471, 2009.

[109] C. Yakacki and K. Gall, "Shape-memory polymers for biomedical applications," in *Shape-Memory Polymers*, ser. Advances in Polymer Science, A. Lendlein, Ed. Springer Berlin / Heidelberg, 2010, vol. 226, pp. 147–175.

[110] D. A. Perkins, J. L. Reed, Jr., and E. Havens, "Morphing wing structures for loitering air vehicles," vol. AIAA 2004-1888, 2004, presented a the 45th AIAA/ASME/ASCE/AHS/ASC Structures, Structural Dynamics and Materials Conference.

[111] T. Takahashi, N. Hayashi, and S. Hayashi, "Structure and properties of shape-memory polyurethane block copolymers," *Journal of Applied Polymer Science*, vol. 60, pp. 1061–1069, 1996.

[112] Y. Liu, K. Gall, M. L. Dunn, A. R. Greenberg, and J. Diani, "Thermomechanics of

shape memory polymers: uniaxial experiments and constitutive modeling," *Int. J. Plas.*, vol. 22, pp. 279–313, 2006.

[113] H. J. Qi, T. D. Nguyen, F. Castro, C. Yakacki, and R. Shandas, "Finite deformation thermo-mechanical behavior of thermally-induced shape memory polymers," *J. Mech. Phys. Solids*, vol. 56, pp. 1730–1751, 2008.

[114] Y. Chen and D. C. Lagoudas, "A constitutive theory for shape memory polymers. Part I large deformations," *J. Mech. Phys. Solids*, vol. 56, pp. 1752–1765, 2008.

[115] S. Reese, M. Bol, and D. Christ, "Finite element-based multi-phase modelling of shape memory polymer stents," *Comp. Meth. App. Mech. Engr.*, vol. 199, pp. 1276–1286, 2010.

[116] A. Lion, C. Liebl, S. Kolmeder, and J. Peters, "Representation of the glass-transition in mechanical and thermal properties of glass-forming materials:a three-dimensional theory based on thermodynamics with internal state variables," *J. Mech. Phys. Solids*, vol. 58, pp. 1338–1360, 2010.

[117] X. Chen and T. D. Nguyen, "Influence of Thermoviscoelastic Properties and Loading Conditions on the Recovery Performance of Shape Memory Polymers," *Mechanics of Materials*, vol. 43, pp. 127–138, 2011.

[118] T. A. Tervoort, E. T. J. Klompen, and L. E. Govaert, "A multi-mode approach to

finite, three-dimensional, nonlinear viscoelastic behavior of polymer glasses," *J. Rheol.*, vol. 40, pp. 779–797, 1996.

[119] P. J. Dooling and C. P. Buckley, "The onset of nonlinear viscoelasticity in multi-axial creep of glassy polymers: a constitutive model and its application to pmma," *Polymer Engineering and Science*, vol. 38, pp. 892–904, 1998.

[120] A. J. Kovacs, J. J. Aklonis, J. M. Hutchinson, and A. R. Ramos, "Isobaric volume and enthalpy recovery of glasses: II a transparent multiparameter theory," *J. Polymer Science*, vol. 17, pp. 1097–1162, 1979.

[121] G. W. Scherer, "Use of the adam-gibbs equation in the analysis of structural relaxation," *J. Am. Cerm. Soc.*, vol. 67, pp. 504–511, 1984.

[122] A. Q. Tool, "Viscosity and extraordinary heat effects in glass." *J. Am. Ceram. Soc.*, vol. 29, pp. 240–253, 1946.

[123] S. Lu and K. Pister, "Decomposition of deformation and representation of the free energy function for isotropic for isotropic thermoelastic solids," *Int. J. Solids Struct.*, vol. 11, pp. 927–934, 1975.

[124] A. Lion, "On the large deformation behavior of reinforced rubber at different temperatures," *J. Mech. Phys. Solids*, vol. 45, pp. 1805–1834, 1997.

[125] S. M. Rekhson, "Memory effects in glass transition," *Journal of Non-Crystalline Solids*, vol. 84, pp. 68–85, 1986.

[126] E. M. Arruda and M. C. Boyce, "A three-dimensional constitutive model for the large stretch behavior of rubber elastic materials," *J. Mech. Phys. Solids*, vol. 41, pp. 389–412, 1993.

[127] S. Reese and S. Govindjee, "A theory of finite viscoelasticity and numerical aspects," *Int. J. Solids Struct.*, vol. 35, pp. 3455–82, 1998.

[128] G. A. Holzapfel and T. C. Gasser, "A new constitutive framework for arterial wall mechanics and a comparative study of material models," *Journal of Elasticity*, vol. 61, pp. 1–48, 2000.

[129] E. Bouchbinder and J. S. Langer, "Nonequilibrium thermodynamics of driven amorphous materials. ii. effective-temperature theory," *Phys. Rev. E.*, vol. 80, pp. 031 132–1–094 505–7, 2009.

[130] J. Moller, I. Gutzow, and J. W. Schmelzer, "Freezing-in and production of entropy in vitrification," *J. Comp. Phys.*, vol. 125, pp. 094 505–1–094 505–13, 2006.

[131] P. Haupt, A. Lion, and E. Backhaus, "On the dynamic behaviour of polymers under finite strains: constitutive modelling and identification of parameters," *Int. J. Solids Struct.*, vol. 37, no. 26, pp. 3633–3646, 2000.

[132] R. Kohlrausch, "Theorie des elektrischen r§ckstandes in der leidner flasche," *Annalen der Physik und Chemie*, vol. 91, pp. 56–82, 1854.

[133] G. Williams and D. C. Watts, "Non-symmetrical dielectric relaxation behavior arising from a simple empirical decay function," *Tran. Faraday Soc.*, vol. 66, pp. 80–85, 1970.

[134] G. P. Lindsey and G. D. Patterson, "Detailed comparison of the williams-watts and cole-davidson functions," *J. Chem. Phys.*, vol. 73, pp. 3348–3357, 1980.

[135] A. Espinoza and J. J. Aklonis, "Modeling viscoelastic behavior of glasses during physical aging," *Poly. Eng. Sci.*, vol. 33, pp. 486–496, 1993.

[136] R. Xiao and T. D. Nguyen, "Modeling the solvent-induced shape-memory behavior of glassy polymers," *Soft Matter*, vol. 9, no. 39, pp. 9455–9464, 2013.

[137] W. Huang, Y. Zhao, C. Wang, Z. Ding, H. Purnawali, C. Tang, and J. Zhang, "Thermo/chemo-responsive shape memory effect in polymers: a sketch of working mechanisms, fundamentals and optimization," *Journal of Polymer Research*, vol. 19, no. 9, pp. 1–34, 2012.

[138] C. Wang, W. Huang, Z. Ding, Y. Zhao, and H. Purnawali, "Cooling-/water-responsive shape memory hybrids," *Composites Science and Technology*, vol. 72, no. 10, pp. 1178–1182, 2012.

[139] Y. Zhao, C. Chun Wang, W. Min Huang, and H. Purnawali, "Buckling of poly (methyl methacrylate) in stimulus-responsive shape recovery," *Applied Physics Letters*, vol. 99, no. 13, pp. 131 911–131 911, 2011.

[140] C. C. Wang, Y. Zhao, H. Purnawali, W. M. Huang, and L. Sun, "Chemically induced morphing in polyurethane shape memory polymer micro fibers/springs," *Reactive and Functional Polymers*, 2012.

[141] W. Huang, "Thermo-moisture responsive polyurethane shape memory polymer for biomedical devices," *Open Medical Devices Journal*, vol. 2, no. 1, pp. 11–19, 2010.

[142] K. Smith, S. Parks, M. Hyjek, S. Downey, and K. Gall, "The effect of the glass transition temperature on the toughness of photopolymerizable (meth) acrylate networks under physiological conditions," *Polymer*, vol. 50, no. 21, pp. 5112–5123, 2009.

[143] K. Smith, P. Trusty, B. Wan, and K. Gall, "Long-term toughness of photopolymerizable (meth) acrylate networks in aqueous environments," *Acta Biomaterialia*, vol. 7, no. 2, pp. 558–567, 2011.

[144] R. Simha and R. Boyer, "On a general relation involving the glass temperature and coefficients of expansion of polymers," *The Journal of Chemical Physics*, vol. 37, no. 5, pp. 1003–1007, 1962.

[145] R. Xiao, J. Choi, N. Lakhera, C. Yakacki, C. Frick, and T. Nguyen, "Modeling the glass transition of amorphous networks for shape-memory behavior," *Journal of the Mechanics and Physics of Solids*, vol. 61, no. 7, pp. 1612–1635, 2013.

[146] X. Chen and T. D. Nguyen, "Influence of thermoviscoelastic properties and loading

conditions on the recovery performance of shape memory polymers," *Mechanics of Materials*, vol. 43, no. 3, pp. 127–138, 2011.

[147] S. Joshi, C. Eberl, B. Cao, K. Ramesh, and K. Hemker, "On the occurrence of portevin–le châtelier instabilities in ultrafine-grained 5083 aluminum alloys," *Experimental mechanics*, vol. 49, no. 2, pp. 207–218, 2009.

[148] W. Bragg and E. J. Williams, "The effect of thermal agitation on atomic arrangement in alloys," *Proceedings of the Royal Society of London. Series A*, vol. 145, no. 855, pp. 699–730, 1934.

[149] M. C. Boyce, G. G. Weber, and D. M. Parks, "On the kinematics of finite strain plasticity," *J. Mech. Phys. Solids*, vol. 37, pp. 647–665, 1989.

[150] K. Chou, S. Lee, and C. Han, "Water transport in crosslinked 2-hydroxyethyl methacrylate," *Polymer Engineering & Science*, vol. 40, no. 4, pp. 1004–1014, 2004.

[151] N. Thomas and A. Windle, "A theory of case ii diffusion," *Polymer*, vol. 23, no. 4, pp. 529–542, 1982.

[152] P. Vijalapura and S. Govindjee, "Numerical simulation of coupled-stress case ii diffusion in one dimension," *Journal of Polymer Science Part B: Polymer Physics*, vol. 41, no. 18, pp. 2091–2108, 2003.

[153] S. Chen, J. Hu, and H. Zhuo, "Study on the moisture absorption of pyridine contain-

ing polyurethane for moisture-responsive shape memory effects," *Journal of materials science*, vol. 46, no. 20, pp. 6581–6588, 2011.

[154] C. GŚell and G. B. McKenna , "Influence of physical ageing on the yield response of model dgeba/poly(propylene oxide) epoxy glasses," *Polymer*, vol. 33, pp. 2103 – 2113, 1992.

[155] L. C. E. Struik, "On the rejuvenation of physically aged polymers by mechanical deformation," *Polymer*, vol. 38, pp. 4053 – 4057, 1997.

[156] B. D. Coleman and M. E. Gurtin, "Thermodynamics with internal state variables," *Journal of Chemical Physics*, vol. 47, pp. 597–613, 1967.

[157] J. S. Bergstrom and M. Boyce, "Constitutive modeling of the large strain time-dependent behavior of elastomers," *J. Mech. Phys. Solids*, vol. 46, pp. 931–954, 1998.

[158] E. Klompen, T. Engels, L. Govaert, and H. Meijer, "Modeling of the postyield response of glassy polymers: influence of thermomechanical history," *Macromolecules*, vol. 38, no. 16, pp. 6997–7008, 2005.

[159] P. Macedo and A. Napolitano, "Effects of a distribution of volume relaxation times in the annealing of bsc glass," *J Res Natl Bur Stand*, vol. 71, pp. 231–238, 1967.

[160] J. J. Aklonis, "Kinetic treatments of glass transition phenomena and viscoelastic

properties of glasses," *Polymer Engineering and Science*, vol. 23, pp. 896–902, 1981.

[161] H. X. Li and C. P. Buckley, "Necking in glassy polymers: Effects of intrinsic anisotropy and structural evolution kinetics in their viscoplastic flow," *International Journal of Plasticity*, vol. 26, pp. 1726 – 1745, 2010.

[162] L. F. Cugliandolo, J. Kurchan, and L. Peliti, "Energy flow, partial equilibration, and effective temperatures in systems with slow dynamics," *Physical Review E*, vol. 55, no. 4, p. 3898, 1997.

[163] L. Berthier and J.-L. Barrat, "Nonequilibrium dynamics and fluctuation-dissipation relation in a sheared fluid," *The Journal of Chemical Physics*, vol. 116, no. 14, pp. 6228–6242, 2002.

[164] D. Durian, "Foam mechanics at the bubble scale," *Physical review letters*, vol. 75, no. 26, p. 4780, 1995.

[165] I. K. Ono, C. S. OÕHern, D. Durian, S. A. Langer, A. J. Liu, and S. R. Nagel, "Effective temperatures of a driven system near jamming," *Physical review letters*, vol. 89, no. 9, p. 095703, 2002.

[166] H. A. Makse and J. Kurchan, "Testing the thermodynamic approach to granular matter with a numerical model of a decisive experiment," *Nature*, vol. 415, no. 6872, pp. 614–617, Feb. 2002. [Online]. Available: http://dx.doi.org/10.1038/415614a

[167] J. Langer, "Dynamics of shear-transformation zones in amorphous plasticity: Formulation in terms of an effective disorder temperature," *Physical Review E*, vol. 70, no. 4, p. 041502, 2004.

[168] M. L. Falk and J. Langer, "Deformation and failure of amorphous, solidlike materials," *Annual Review of Condensed Matter Physics*, vol. 2, pp. 353–373, 2011.

[169] E. Bouchbinder and J. S. Langer, "Nonequilibrium thermodynamics of the kovacs effect," *Soft Matter*, vol. 6, pp. 3065–3073, 2010.

[170] E. Bouchbinder and J. Langer, "Shear-transformation-zone theory of linear glassy dynamics," *Physical Review E*, vol. 83, no. 6, p. 061503, 2011.

[171] K. Kamrin and E. Bouchbinder, "Two-temperature continuum thermomechanics of deforming amorphous solids," *J. Mech. Phys. Solids*, vol. 73, pp. 269–288, 2014.

[172] D. Rittel, "On the conversion of plastic work to heat during high strain rate deformation of glassy polymers," *Mechanics of Materials*, vol. 31, no. 2, pp. 131–139, 1999.

[173] R. Xiao, J. Guo, and T. D. Nguyen, "Modeling the multiple shape memory effect and temperature memory effect in amorphous polymers," *RSC Advances*, vol. 5, pp. 416–423, 2015.

[174] G. A. Holzapfel, *Nonlinear solid mechanis: a continuum approach for engineers*. Chichester: John Wiley and Sons, LTD, 2000.

[175] W. Hong, Z. Liu, and Z. Suo, "Inhomogeneous swelling of a gel in equilibrium with a solvent and mechanical load," *International Journal of Solids and Structures*, vol. 46, no. 17, pp. 3282–3289, 2009.

[176] T. Mullin, S. Deschanel, K. Bertoldi, and M. Boyce, "Pattern transformation triggered by deformation," *Physical review letters*, vol. 99, no. 8, p. 084301, 2007.

[177] K. Bertoldi, M. Boyce, S. Deschanel, S. Prange, and T. Mullin, "Mechanics of deformation-triggered pattern transformations and superelastic behavior in periodic elastomeric structures," *Journal of the Mechanics and Physics of Solids*, vol. 56, no. 8, pp. 2642–2668, 2008.

[178] J. Li, J. Shim, J. Deng, J. T. Overvelde, X. Zhu, K. Bertoldi, and S. Yang, "Switching periodic membranes via pattern transformation and shape memory effect," *Soft Matter*, vol. 8, no. 40, pp. 10 322–10 328, 2012.

Vita

Rui Xiao was born in Lu'an, Anhui Province, China in 1987. He received a B.S. in Theoretical and Applied Mechanics from University of Science and Technology of China in June, 2009. He joined Professor Nguyen's lab at Johns Hopkins University in September 2009 and obtained a M.S.E. in Mechanical Engineering in May 2011. His research in Hopkins focused on amorphous shape-memory polymers and hydrogels, which has been published in Journal of the Mechanics and Physics of Solids, Soft Matter, RSC Advances, Smart Materials and Structures, Polymers, et al. His general interest lies in soft active materials and solid mechanics.